Alma Mater Studiorum · Università di Bologna

Scuola di Scienze
Dipartimento di Fisica e Astronomia
Corso di Laurea Magistrale in Fisica

Loop-induced annihilation of dark matter

Relatore: **Presentata da:**

Prof. Fabio Maltoni   **Daniele Massaro**

Correlatore:

Dott. Jan Heisig

Anno Accademico 2018/2019

The story so far:
In the beginning the Universe was created.
This has made a lot of people very angry
and been widely regarded as a bad move.

Douglas Adams
The Restaurant at the End of the Universe

Alla mia famiglia, a Federica.

Abstract

Plenty of evidences suggest the existence of a new type of non-luminous matter in the Universe, that has been called dark matter. Its nature is still unresolved, however, there is a widespread belief that is a new particle. Today we have three important search strategies for dark matter: indirect detection, direct detection and collider searches. In this thesis we focus on indirect detection, which investigates the products of annihilation of dark matter in overdense regions of the Universe. In particular we focus on γ-ray observations, considering the γ-ray line signal, arising from dark matter annihilation into a pair of monochromatic photons. For electrically neutral dark matter, this process can proceed only via loop diagrams. Its computation can be done using numerical techniques. Numerical tools are a huge step forward in the dark matter research, and help scientists to make predictions and improve their models. However, at the current status there is no tool allowing for the calculation of loop-induced γ-ray signals for arbitrary models. In this thesis we make an important step towards filling this gap. We focus on the numerical tool MADDM, and we validate the feature of automatised loop-induced computation using two dark matter models: the singlet scalar Higgs portal model and a simplified top-philic model. We then constrain the parameter space of these models using the current experimental results. In particular we consider the upper limits on γ-ray line searches obtained by FERMI-LAT and HESS collaborations, finding that they provide important constraints on the parameters of both models.

Sommario

Un gran numero di evidenze osservative suggerisce l'esistenza di un nuovo tipo di materia che non emette luce e che è stata chiamata materia oscura. La sua natura è ancora misteriosa, ciò nonostante, un'ipotesi largamente affermata è che si tratti di una nuova particella. Oggi abbiamo tre importanti strategie di ricerca per la materia oscura: detezione indiretta, detezione diretta e ricerca con acceleratori. In questa tesi ci siamo concentrati sulla detezione indiretta. Essa studia i prodotti dell'annichilazione di materia oscura in regioni particolarmente dense dell'Universo. In particolare ci siamo concentrati sull'osservazione di uno spettro monocromatico di raggi γ, prodotto dall'annichilazione di materia oscura in una coppia di fotoni monoenergetici. Attualmente si ipotizza che la materia oscura sia elettricamente neutra, quindi questo processo può procedere solo attraverso diagrammi a loop. Il calcolo di tali diagrammi può essere svolto utilizzando tecniche numeriche. I software numerici costituiscono un grande passo in avanti nella ricerca della materia oscura, aiutando gli scienziati a realizzare predizioni e migliorare i loro modelli. Tuttavia, attualmente non ci sono software in grado di eseguire il calcolo di processi loop-indotti per spettri γ monoenergetici in modelli arbitrari di materia oscura. L'obiettivo di questa tesi è quello di colmare questa lacuna. Ci concentreremo sul software numerico MadDM testando il calcolo di processi loop-indotti su due modelli di materia oscura: il modello "singlet Scalar Higgs portal" e un modello semplificato "top-philic". Successivamente studieremo lo spazio dei parametri dei modelli, implementando i vincoli sperimentali attuali. In particolare, considereremo i limiti di esclusione sulle linee γ ottenuti dalle collaborazioni Fermi-LAT e HESS, riuscendo a imporre vincoli importanti sui parametri di entrambi i modelli.

Contents

Chapter 1

Introduction

Since the early 1930s, plenty of issues related to our astrophysics and cosmology appeared and are still unresolved. The observation of Coma Cluster by astronomer Fritz Zwicky [1] shows an unexpectedly higher mass compared to expectations. The measurement of galaxy rotation curves by Vera Rubin [2] suggests that galaxies are more massive than what we can actually observe through photons. The Cosmic Microwave Background (CMB) shows that our structure formation models were not able to describe the measured density contrast. All these issues lead to the hypothesis of a new kind of matter, that is invisible and undetectable with electromagnetic radiation and that is called dark matter. The dark matter hypothesis allowed to solve the mentioned issues, however, its elusive nature makes it very hard to detect. Indeed, we only know few facts about dark matter. We know it interacts at least gravitationally and that it should make up nearly the 26% of the energy budget of the Universe [3]. The rest is made of the ordinary matter described by the Standard Model of particle physics, that accounts only for the 5%, while the remaining 69% is known as dark energy.

A huge step forward in the comprehension of dark matter has been done in the last decades and new observations has been carried out. There is a widespread belief that dark matter is a new particle which has probably interacted with Standard Model particles in its history. Following this idea, today we have three important search strategies for dark matter: indirect detection, which studies the products of dark matter annihilation in overdense regions; direct detection, that investigates the nucleon-dark matter scattering; colliders searches, aimed at producing dark matter particles through collisions of Standard Model ones or through fixed target experiments to study the high-intensity frontier. Nonetheless, experiments alone are not enough for a complete understanding of the dark matter nature. The other key ingredient is a theoretical viable dark matter model. The assumption of dark matter being a new particle has lead scientists to build a huge variety of dark matter models, with different mass scale, number of particles and free parameters. Dark matter models can be constrained using the results of experiments and observations, which can deeply constrain the model parameter space. The comparison between theory and experiments can be accomplished only if we are able to compute the relevant dark matter
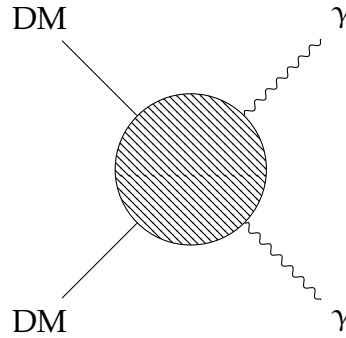
Figure 1.1: Feynman diagram of annihilation of dark matter (DM) into a pair of photons. This process can proceed only via a loop.

quantities from each model. However, in most cases, a pure analytical treatment is impractical. The best approach is to use numerical tools: they are able to compute the relevant observables for any kind of model and allows scientists to study the phenomenology without being aware of the analytical implications. In this framework, a lot of tools have become available. In this thesis we will focus on MADDM [4], a numerical tool able to compute many relevant quantities related to dark matter. MADDM is a plugin of the numerical tool MADGRAPH5_AMC@NLO [5, 6] and can exploit all its functionalities. In particular, given a dark matter model, MADDM is able to:

- compute the production/annihilation velocity averaged cross section, relevant for both relic density and indirect detection computations;

- compute the nucleon-dark matter scattering cross section, relevant for direct detection;

- compute collider predictions (thanks to its underlying framework MADGRAPH5_AMC@NLO);

- compare theoretical observables against experimental results, by providing statistical tools.

In this thesis we will utilise MADDM in order to analyse an interesting signature of dark matter indirect detection. We will focus on dark matter annihilation into a pair of photons, that is shown in fig. 1.1. This is a two-body process, so the final photons are monochromatic and their energy spectrum is constituted by a sharp line peaked at the mass of the dark matter particle. This is a *smoking gun* signal as the astronomical background is low. However, because dark matter in general is supposed to be electrically neutral, this channel proceeds via a loop-induced process. There are tools that provides a framework in which compute loop-induced processes: MICROMEGAS 3.0 [7] allows the computation of loop-induced Higgs decay in $\gamma\gamma$ and gg, along with the loop-induced annihilation

in γZ and $\gamma\gamma$ in the framework of the Minimal Supersymmetric Standard Model. Moreover, in the case of Supersymmetry, DarkSUSY 6 [8] allows for the computation of loop-induced annihilation of dark matter into $\gamma\gamma$, γZ and gg. However, at the current stage there is no numerical tool allowing for the calculation of loop-induced γ-ray signals for arbitrary models. In this thesis we will fill this gap: MadDM can, in principle, inherit the capability to compute loop-induced processes from MadGraph5_aMC@NLO [9]; we will validate it with two dark matter models. We have chosen the singlet scalar Higgs portal model [10–12] and a simplified top-philic model [13]. The MadDM predictions for these two models can be corroborated with an effective approach for the singlet scalar Higgs portal model [14–16] and with analytical expressions for the top-philic model [17, 18]. We will then use the code to derive limits on the models, exploiting the constraints on γ-ray line signal set by the experiments Fermi-LAT [19] and HESS [20].

The thesis is organised as follows. In chap. 2 we will review the main concepts of cosmology, needed to understand the theory of dark matter. In chap. 3 we introduce dark matter, discussing the main indirect evidences and possible particle candidates; we will then go through the experimental methods that are used today, listing their most interesting results as far as it concerns this thesis. In chap. 4 we review the main numerical techniques that are available to compute loop integrals, and the three Mathematica packages FeynRules [21], FeynArts [22], NLOCT [23] we will use. These packages allow us to implement dark matter models at a Next-to-Leading order level, in a format that can be used in MadDM to compute loop-induced processes. In chap. 5 we present the original part of this work. We introduce the numerical tool MadDM, focusing on its capabilities. We test the loop-induced computation made by MadDM in two models, comparing it to known results. We study the phenomenology of the models, showing the main constraints on their parameter space. We conclude in chap. 6.

Chapter 2

A brief review of cosmology

The aim of this chapter is to provide the reader a brief introduction to cosmology, for what concerns the arguments that are needed in the next chapters. A more complete treatment of the topics can be found in books, for example [24, 25]. We are working in natural units ($c = 1, \hbar = 1$).

2.1   The Friedmann equation

When we observe our Universe on very large scales, we can say larger than $10\,\mathrm{Mpc}^*$, we see that it is both homogeneus and isotropic. Cosmologists sum up these features in what is called Cosmological Principle. When studying cosmology we consider the framework of general relativity, so we write the Einstein's equations:

$$R_{\mu\nu} - \frac{1}{2}g_{\mu\nu}R + \Lambda g_{\mu\nu} = 8\pi G T_{\mu\nu}\,, \qquad (2.1)$$

where $R_{\mu\nu}$ is the Ricci tensor, R is the Ricci scalar, Λ is the cosmological constant, $g_{\mu\nu}$ is the space-time metric, that in our convention is $g_{\mu\nu} = \mathrm{diag}(1,-1,-1,-1)$ (*West Coast* or *mostly minus*) and $T_{\mu\nu}$ is the energy-momentum tensor. By assuming the Cosmological Principle, we can solve them. We obtain a metric that describes our Universe on large scales, with the assumptions of homogeneity and isotropy. This is known as the Friedman-Lemaître-Robertson-Walker metric:

$$ds^2 = dt^2 - a(t)^2\left(\frac{dr^2}{1-kr^2} + r^2 d\vartheta^2 + r^2\sin^2\vartheta d\varphi^2\right), \qquad (2.2)$$

where r, ϑ, φ are the spherical coordinates and $a(t)$ is called scale factor. The factor k is called curvature and can take the possible values: 1 for closed Universe, 0 for flat Universe and -1 for open Universe. We can define the parameter

$$H(t) \doteq \frac{\dot{a}(t)}{a(t)}\,, \qquad (2.3)$$

$^*1\,\mathrm{pc} = 3.086 \times 10^{16}\,\mathrm{m}.$

called the Hubble parameter. The value of $H(t)$ depends on time. Today[†] we have [3]:

$$H_0 = (67.36 \pm 0.54)\,\text{km s}^{-1}\,\text{Mpc}^{-1} \approx h \cdot 100\,\text{km s}^{-1}\,\text{Mpc}^{-1}, \qquad (2.4)$$

where we introduce the standard parametrisation with the dimensionless parameter $h = 0.6736 \pm 0.0054$. The Hubble parameter is a measure for the expansion of the Universe. Today observations agree that the Universe expansion is accelerating. An accelerating expansion means that the rate of change $\dot{a}(t)$ increases in time, so its rate of change $\ddot{a}(t)$ must be positive, $\ddot{a}(t) > 0$. That does not mean that $H(t)$ is increasing in time, in fact if we define the deceleration parameter:

$$q \doteq -\frac{\ddot{a}a}{\dot{a}^2}, \qquad (2.5)$$

we can obtain

$$\frac{dH}{dt} = -H^2(1+q). \qquad (2.6)$$

The deceleration parameter has been measured today to be $q_0 \approx -0.55$, so $\dot{H}_0 < 0$, the Hubble parameter is decreasing in time, though the Universe is in an accelerating expansion. This implies that while observing the Universe at a fixed distance, galaxies crossing that point are moving slower at later time.

Turning back to eq. (2.1), we will focus on the energy-momentum tensor. Its components physically mean the following: T^{00} is the energy density; T^{0j} is the energy flux across the spatial surface $x_j = $ constant, $j \in \{1, 2, 3\}$; T^{i0} is the density of ith component of momentum; T^{ij} is the ith component of momentum flux across the spatial-surface $x_j = $ constant. Normal momentum flux T^{ij}, with $i = j$, causes normal stress on the fluid element and the others T^{ij}, with $i \neq j$, cause shear stress. We can consider the approximation of perfect fluid. Perfect fluids are idealised models of fluids characterised by no viscosity or heat conduction. We can study the energy-momentum tensor in a comoving frame with the perfect fluid. Since heat conduction is null, there is no energy flux, so $T^{0j} = 0$. The absence of viscosity implies that there are not shear stresses $T^{ij} = 0$, with $i \neq j$. Further, isotropy implies that spatial components must be equal, so that $T^{ij} \propto \delta^{ij}$. That means we can cast the energy-momentum tensor in a simple, diagonal form:

$$T^{\mu\nu} = \text{diag}(\rho, -P, -P, -P), \qquad (2.7)$$

where ρ is the energy density and P is the pressure, that characterises normal stresses.

The dynamical equations describing the evolution of the scale factor $a(t)$ can be found solving eq. (2.1), assuming the metric (2.2). The time-time component of eq. (2.1) gives the so called Friedmann equation [24]

$$\dot{a}^2 + k = \frac{8}{3}\pi G\rho a^2, \qquad (2.8)$$

[†]To label a quantity measured *today* we use the subscript 0, e.g. $a_0 = a(t_0)$.

while the space-space components yield

$$\ddot{a} = -\frac{4}{3}(\rho + 3P)a \,, \tag{2.9}$$

From eq. (2.8) we obtain

$$1 + \frac{k}{H(t)^2 a(t)^2} = \rho(t)\frac{8\pi G}{3H(t)^2} \,, \tag{2.10}$$

where we define the critical density:

$$\rho_c(t) \doteq \frac{3H(t)^2}{8\pi G} \,, \tag{2.11}$$

and consequently we introduce the dimensionless density parameter as the ratio

$$\Omega(t) \doteq \frac{\rho(t)}{\rho_c(t)} \,. \tag{2.12}$$

2.2 Composition of the Universe

In the previous section we have considered the perfect fluid approximation and we cast the energy-momentum tensor as in eq. (2.7). It satisfies the continuity equation $\nabla_\mu T^{\mu\nu} = 0$, where ∇_μ is the covariant derivative. Considering the $\nu = 0$ component we obtain the conservation of energy:

$$\frac{\partial \rho}{\partial t} + 3\frac{\dot{a}}{a}(\rho + P) = 0 \,. \tag{2.13}$$

In general we can specify an equation of state for each component of the Universe in the form:

$$P = w\rho \,, \tag{2.14}$$

where w is a constant. The value of w for each component is:

- $w = 0$, for non-relativistic matter (dust). We have $P = nk_B T = \rho k_B T/m$ (k_B is the Boltzmann constant), but for non-relativistic species (see § 2.3) $T \ll m$, so that $P \approx 0$;

- $w = 1/3$, for radiation, because radiation pressure can be expressed as $P = \rho/3$;

- $w = -1$, for dark energy. Today observations show that the expansion of the Universe is accelerated, and this is incompatible with a dust-dominated Universe. The simplest way to take it into account is to assume the presence of Dark Energy, implemented via the celebrated cosmological constant, characterised by $P = -\rho$.
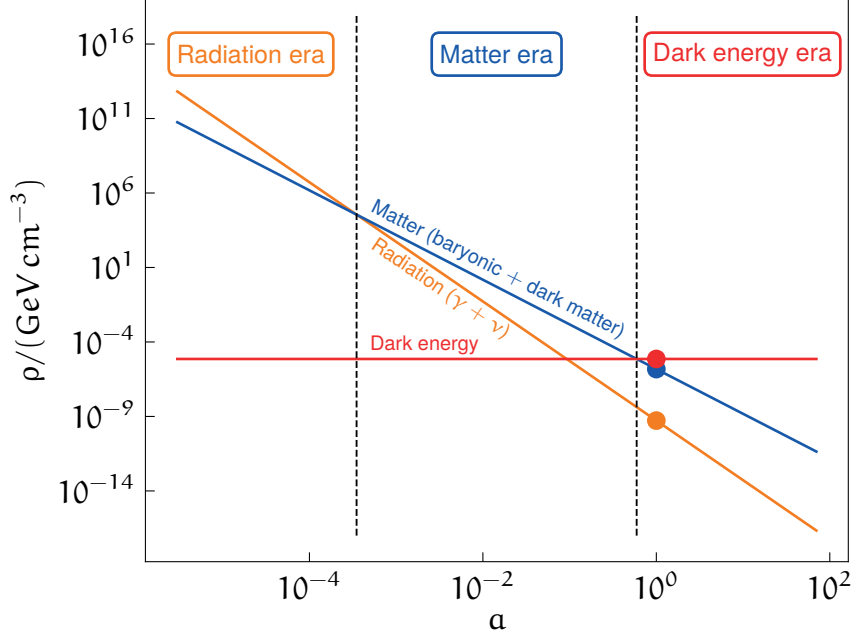
Figure 2.1: Trend of the energy density of the various components of the Universe with the names of the different eras. The highlighted points are relative to today ($a_0 = 1$).

We can integrate (2.13) obtaining

$$\rho \propto a^{-3(1+w)}, \tag{2.15}$$

and so we can write the different trend of the components through time:

$$\rho_r \propto a^{-4}, \tag{2.16a}$$

$$\rho_m \propto a^{-3}, \tag{2.16b}$$

$$\rho_\Lambda \propto a^0. \tag{2.16c}$$

The different dependence of the constituents in eqs. (2.16a) and (2.16b) means that there was an instant in which their energy density was equal and that is called equivalence. Moreover, if we plot the dependencies in eq. (2.16) it is possible to recognise three different epochs: in each of them one of the components is dominant with respect to the others, as we can see in fig. 2.1. We can also compute the time dependence of $a(t)$, by assuming as anstatz a power law $a(t) \propto t^\beta$ and using eq. (2.9) upon substitution of eq. (2.15):

$$a \propto t^{2/(3+3w)}, \tag{2.17}$$

and consequently,

$$a \propto t^{1/2} \quad \text{radiation epoch,} \tag{2.18a}$$

$$a \propto t^{2/3} \quad \text{matter epoch.} \tag{2.18b}$$
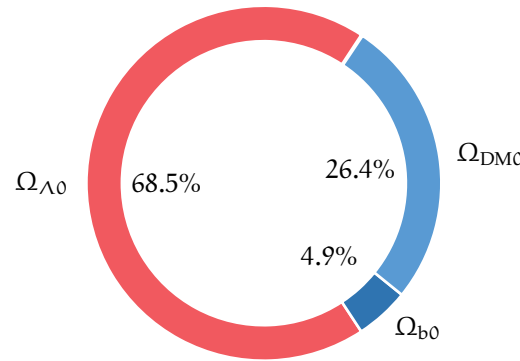
Figure 2.2: A pie chart showing the composition of the Universe today. The radiation component is not shown because is too small compared to the scale of the chart.

The density parameter is given by considering all the contributions of the different components the Universe is made of:

$$\Omega = \sum_{i \in \{ \text{ components } \}} \Omega_i \, . \tag{2.19}$$

Today we know the contribution of each component, thanks to the PLANCK experiment [3]. It has studied the CMB assuming that the Big Bang cosmological model is parametrised by the ΛCDM model. It stares the Universe contains three major components: the cosmological constant Λ, related to dark energy, the cold dark matter (CDM, see § 3.2) and the ordinary matter, described by the Standard Model. Their contribution to the energy budget of the Universe today is:

- Radiation: $\Omega_{r0} \approx 5 \times 10^{-5}$;

- Matter[‡]: $\Omega_{m0} = 0.3153 \pm 0.0073$, that comprises baryonic matter ($\Omega_{b0} \approx 0.0493$) and dark matter ($\Omega_{DM0} \approx 0.264$);

- Dark Energy: $\Omega_{\Lambda 0} = 0.6847 \pm 0.0073$.

The composition of our Universe today is shown in fig. 2.2.

2.3 Equilibrium thermodynamics

The history of the Universe is an history of cooling. If we consider the actual temperature of the Universe, we have $T_0 = 2.73\,\text{K}$, that is the temperature of the CMB radiation. Going backwards in time, in what is called early Universe,

---

[‡]In this chapter we are not making any distinction between baryonic matter and dark matter.

temperature was higher than now. When we talk about the Universe, we need to think of it as made of different species, that are all the known (and unknown) particles. It is important to remark that the temperature is something related to the species. Considering the sizeable interaction strength of the Standard Model gauge groups, the early Universe was in thermal equilibrium in good approximation. When different species are in thermal equilibrium, there are processes (for e.g. elastic scatterings between particles) that maintain the species thermalised. If these processes are faster than the rate of the expansion of the Universe, they are efficient and keep the species in equilibrium. Considering a weakly interacting gas of particles with g internal degrees of freedom we can compute the expression of the number density n, the energy density ρ and the pressure P at thermal equilibrium,

$$n = \frac{g}{(2\pi)^3} \int f(\mathbf{p}) \, d^3\mathbf{p} \,, \tag{2.20}$$

$$\rho = \frac{g}{(2\pi)^3} \int f(\mathbf{p}) E(\mathbf{p}) \, d^3\mathbf{p} \,, \tag{2.21}$$

$$P = \frac{g}{(2\pi)^3} \int \frac{|\mathbf{p}|^2}{3E(\mathbf{p})} f(\mathbf{p}) \, d^3\mathbf{p} \,, \tag{2.22}$$

where $f(\mathbf{p})$ is the phase space distribution function (occupancy function) and the energy is given by $E(\mathbf{p})^2 = |\mathbf{p}|^2 + m^2$. When particles exchange energy and momentum efficiently, the system is in kinetic equilibrium, and the function $f(\mathbf{p})$ is different for fermions and bosons, having the form of the Fermi-Dirac (FD) and Bose-Einstein (BE) distribution functions:

$$f_{\substack{FD \\ BE}}(\mathbf{p}) = \left[\exp\left(\frac{E(\mathbf{p}) - \mu}{T} \right) \pm 1 \right]^{-1} \,, \tag{2.23}$$

where μ is the chemical potential. For a process like

$$a + b \rightleftharpoons c + d \,, \tag{2.24}$$

we say that is in chemical equilibrium when we have the following relation for chemical potentials:

$$\mu_a + \mu_b \rightleftharpoons \mu_c + \mu_d \,. \tag{2.25}$$

We can write the eqs. (2.20)–(2.22) in spherical coordinates. Considering the parameter $x = m/T$ and making the change of variable $\xi = p/T$ we get:

$$n = \frac{g}{2\pi^2} T^3 \int_0^{+\infty} \frac{\xi^2}{\exp\left(\sqrt{\xi^2 + x^2}\right) \pm 1} \, d\xi \,, \tag{2.26}$$

$$\rho = \frac{g}{2\pi^2} T^4 \int_0^{+\infty} \frac{\xi^2 \sqrt{\xi^2 + x^2}}{\exp\left(\sqrt{\xi^2 + x^2}\right) \pm 1} \, d\xi \,, \tag{2.27}$$

$$P = \frac{g}{6\pi^2} T^4 \int_0^{+\infty} \frac{\xi^4}{\sqrt{\xi^2 + x^2}\left(\exp\left(\sqrt{\xi^2 + x^2}\right) \pm 1\right)} \, d\xi \,, \tag{2.28}$$

where we have dropped the chemical potential, because at early time we can assume it to be small, $\mu \approx 0$. It is possible to consider the relativistic and non-relativistic scenarios to cast eqs. (2.26)–(2.28) in a simple form. A species χ in the Universe with mass m_χ is relativistic if $T \gg m_\chi$ ($x \ll 1$). A relativistic species contributes to the energy density of the radiation component of the Universe. Moreover, the energy of the species in thermal equilibrium is larger than m_χ, so that the species χ can be produced by processes involving other species. When, instead, we have $T \ll m_\chi$ ($x \gg 1$), χ becomes non-relativistic. When a species is non-relativistic, there is not enough energy to produce it. We can write a simple expression for the number density and the energy density at thermal equilibrium:

- relativistic case,

$$
n = \begin{cases} \dfrac{\zeta(3)}{\pi^2} g T^3 & \text{bosons,} \\[2mm] \dfrac{3}{4} \dfrac{\zeta(3)}{\pi^2} g T^3 & \text{fermions,} \end{cases}
\tag{2.29}
$$

$$
\rho = \begin{cases} \dfrac{\pi^2}{30} g T^4 & \text{bosons,} \\[2mm] \dfrac{7}{8} \dfrac{\pi^2}{30} g T^4 & \text{fermions,} \end{cases}
\tag{2.30}
$$

$$
P = \frac{\rho}{3} ;
\tag{2.31}
$$

- non-relativistic case,

$$
n = g \left(\frac{m_\chi T}{2\pi} \right)^{3/2} \exp\left(-\frac{m_\chi}{T} \right),
\tag{2.32}
$$

and at lowest order we can consider $E(\mathbf{p}) \approx m_\chi$ and so energy density is equal to the mass density,

$$
\rho = m_\chi n ;
\tag{2.33}
$$

while, considering the equation of state for a perfect gas we have,

$$
P = n T,
\tag{2.34}
$$

and, by the means of $m_\chi \gg T$, we have $P \ll \rho$, so a non-relativistic gas of particles acts like pressureless dust.

The relativistic or non-relativistic nature of a certain species implies a different trend in its temperature during the evolution of the Universe. We can compute those trends using arguments of general relativity, that are shown in [26], obtaining:

$$
T \propto a^{-1} \quad \text{relativistic,}
\tag{2.35}
$$

$$
T \propto a^{-2} \quad \text{non-relativistic.}
\tag{2.36}
$$

When does a species stop to be in thermal equilibrium with the others? Consider the rate of the expansion of the Universe, given by the Hubble parameter H. The thermalisation processes that maintain equilibrium are: the scattering between different species and the annihilation or production of a species. Their rate Γ depends on the cross section and on the relative number density:

$$\Gamma = n\sigma v. \tag{2.37}$$

The thermal equilibrium is maintained as long as $\Gamma > H$. During the expansion of the Universe, the number density of a certain species drops as eqs. (2.29) and (2.32), because of the decreasing temperature, so there will be a time, called decoupling, when the condition above is no longer satisfied, in other words $\Gamma < H$. From that moment on the species considered is no more in thermal equilibrium with the cosmological fluid and its number density, energy density and pressure can not be described by eqs. (2.29)–(2.34). In summary, the key events that happened to the various species during the evolution of the Universe are:

- the transition from being relativistic to being non-relativistic;

- the decoupling: the processes that kept the species thermalised each other becomes inefficient, because their rate is lower than the expansion rate of the Universe.

We can compute the total radiation energy density ρ_r by simply summing eq. (2.30) over the relativistic species,

$$\rho_r(T) = \sum_i \rho_i(T) = \frac{\pi^2}{30} g_\star(T) T^4, \tag{2.38}$$

where $g_\star(T)$ is the effective number of degrees of freedom at a certain temperature T. It has two contributions:

$$g_\star(T) = g_\star^{\text{th}}(T) + g_\star^{\text{dec}}(T) \tag{2.39}$$

- species that are relativistic and in thermal equilibrium with radiation:

$$g_\star^{\text{th}}(T) = \sum_{i\in\{\text{ bosons }\}} g_i + \frac{7}{8} \sum_{i\in\{\text{ fermions }\}} g_i, \tag{2.40}$$

  there is no dependence on the temperature, because all the species are in thermal equilibrium and have the same temperature T;

- species that are relativistic but also decoupled from the cosmological fluid, so are not in thermal equilibrium with the other species:

$$g_\star^{\text{dec}}(T) = \sum_{i\in\{\text{ bosons }\}} g_i \left(\frac{T_i}{T}\right)^4 + \frac{7}{8} \sum_{i\in\{\text{ fermions }\}} g_i \left(\frac{T_i}{T}\right)^4, \tag{2.41}$$

  and we see the dependence on the temperature of the species.

If we consider T larger than the top mass, every particle of the Standard Model is relativistic, so we have:

$$g_\star(T) = \underbrace{2}_{\gamma} + \underbrace{3\cdot 3}_{W^\pm,\, Z} + \underbrace{8\cdot 2}_{g} + \underbrace{1}_{h} + \frac{7}{8}\left(\underbrace{6\cdot 2\cdot 3\cdot 2}_{q_i,\bar{q}_i \forall i\in\{\text{colours}\}} + \underbrace{3\cdot 2\cdot 2}_{e^\pm,\, \mu^\pm,\, \tau^\pm} + \underbrace{3\cdot 2}_{\nu_e,\, \nu_\mu,\, \nu_\tau} \right)$$
$$= 106.75\,,$$

(2.42)

where we assumed three massless neutrino species.

2.4 Entropy

To describe the evolution of the Universe is useful to have a conserved quantity. We can consider the expansion of the Universe as adiabatic, so we have the conservation of entropy. By the Second Law of Thermodynamics we have

$$T\,dS = dU + P\,dV\,,$$

(2.43)

with $U = \rho V$, so we obtain

$$dS = d\left(\frac{\rho + P}{T}V\right)\,.$$

(2.44)

We can define the entropy per comoving volume,

$$s \doteq \frac{S}{V} = \frac{\rho + P}{T}\,,$$

(2.45)

that is conserved in thermal equilibrium. Now we can compute the total entropy per comoving volume, that is dominated by the relativistic species, as we have done in eq. (2.38), obtaining

$$s = \sum_i \frac{\rho_i + P_i}{T_i} = \frac{2\pi^2}{45} g_{\star S}(T) T^3\,,$$

(2.46)

where $g_{\star S}(T)$ is the effective number of degrees of freedom in Entropy at a certain temperature T and it has two contributions:

$$g_{\star S}(T) = g_{\star S}^{\text{th}}(T) + g_{\star S}^{\text{dec}}(T)$$

(2.47)

- species in thermal equilibrium:

$$g_{\star S}^{\text{th}}(T) = \sum_{i\in\{\text{bosons}\}} g_i + \frac{7}{8} \sum_{i\in\{\text{fermions}\}} g_i = g_\star^{\text{th}}(T)\,,$$

(2.48)

- species that are decoupled:

$$g_{\star S}^{\text{dec}}(T) = \sum_{i\in\{\text{bosons}\}} g_i \left(\frac{T_i}{T}\right)^3 + \frac{7}{8} \sum_{i\in\{\text{fermions}\}} g_i \left(\frac{T_i}{T}\right)^3\,.$$

(2.49)

The conservation of s implies that S is conserved:

$$S = sV \propto sa^3 \propto g_{\star S}(T)T^3 a^3 \,. \tag{2.50}$$

Inverting the above expression we have

$$T \propto g_{\star S}^{-1/3} a^{-1} \,. \tag{2.51}$$

Whenever a species becomes non-relativistic we have that $g_{\star S}$ drops, while the temperature of the thermal bath T raises, according to eq. (2.51). This happens because of the conservation of entropy: when a species becomes non-relativistic, its entropy is transferred to the other species in the thermal bath.

2.5   Structure formation

As mentioned in § 2.1, observations of our Universe on large scales suggest that it is both homogeneous and isotropic. However on small scales it is very lumpy, the density of galaxies is about 10^5 times the average density of the Universe and the density of a cluster of galaxies is about 10^2 to 10^3 times the average density of the Universe. So these structures represent a density perturbations in the actual Universe. We can define a density perturbation as

$$\delta \doteq \frac{\delta\rho}{\rho} = \frac{\rho - \overline{\rho}}{\overline{\rho}} \,. \tag{2.52}$$

Today we can measure perturbations of the order $\delta \approx 10^2$. In the past they were surely lower and we can measure them by observing the temperature fluctuations of the CMB. They are of the order

$$\frac{\Delta T}{T} \lesssim 10^{-5} \,, \tag{2.53}$$

so the Universe was very smooth at that time. How could the Universe get from a smooth situation with $\delta \approx 10^{-5}$ to a lumpy situation with 10^2? Cosmologists think that at the basis of the growth of perturbations we can find the gravitational instabilities, that carried the evolution of small inhomogeneities into the larger ones we can observe today.

We will focus on the evolution of a matter density Universe in the presence of a gravitational field. We will treat the problem from a newtonian point of view, without using general relativity: this approximation is valid as long as the cosmic structures are small compared to the curvature of the Universe. We can write the equations of the newtonian motion of a perfect fluid:

$$\frac{\partial\rho}{\partial t} + \boldsymbol{\nabla} \cdot (\rho\boldsymbol{u}) = 0 \qquad\qquad \text{continuity equation,} \tag{2.54}$$

$$\left(\frac{\partial}{\partial t} + \boldsymbol{u} \cdot \boldsymbol{\nabla}\right)\boldsymbol{u} = -\frac{1}{\rho}\boldsymbol{\nabla}P - \boldsymbol{\nabla}\varphi \quad \text{Euler equation,} \tag{2.55}$$

$$\nabla^2\varphi = 4\pi G\rho \qquad\qquad\qquad \text{Poisson equation,} \tag{2.56}$$

where ρ is the matter density, P is the matter pressure, $\mathbf{u}$ is the local fluid velocity and φ is the gravitational potential. To solve the eqs. (2.54)–(2.56) we can use a perturbative approach: consider a known solution and add a small perturbation to it. Moreover, because we want to develop a linear theory, we can consider only first order contributions. The unperturbed solutions (with subscript 0) is related to an homogeneously expanding fluid:

$$\rho_0 = \rho_0(t_0)\left(\frac{a(t_0)}{a}\right)^3, \tag{2.57a}$$

$$\mathbf{u}_0 = \frac{\dot{a}}{a}\mathbf{r}, \tag{2.57b}$$

$$\nabla\varphi_0 = \frac{4\pi G\rho_0}{3}\mathbf{r}, \tag{2.57c}$$

$$\nabla P_0 = 0. \tag{2.57d}$$

We add a small perturbation in the following way:

$$\rho = \rho_0 + \delta_\rho = \rho_0(1+\delta), \tag{2.58a}$$

$$\mathbf{u} = \mathbf{u}_0 + \delta_{\mathbf{u}}, \tag{2.58b}$$

$$\varphi = \varphi_0 + \delta_\varphi, \tag{2.58c}$$

$$P = P_0 + \delta_P. \tag{2.58d}$$

Then it is better to express everything through the following coordinates $\mathbf{x}$, obtaining:

$$\mathbf{r} = a\mathbf{x}, \tag{2.59a}$$

$$\nabla_\mathbf{r} = \frac{1}{a}\nabla_\mathbf{x}, \tag{2.59b}$$

$$\left(\frac{\partial}{\partial t}\right)_\mathbf{r} + H\mathbf{r}\cdot\nabla_\mathbf{r} = \left(\frac{\partial}{\partial t}\right)_\mathbf{x}. \tag{2.59c}$$

Therefore, we obtain the following differential equation,

$$\ddot{\delta}_k + 2H\dot{\delta}_k + \left(\frac{v_s^2 k^2}{a^2} - 4\pi G\rho_0\right)\delta_k = 0, \tag{2.60}$$

called Jeans equation, where $\delta_k(t) \doteq \hat{\delta}(t,\mathbf{k})$ is the Fourier transform of $\delta(t,\mathbf{x})$,

$$\delta(t,\mathbf{x}) = \int \frac{d^3k}{(2\pi)^3}\hat{\delta}(t,\mathbf{k})\exp(-i\mathbf{k}\cdot\mathbf{x}), \tag{2.61}$$

and v_s is the (adiabatic) sound speed,

$$v_s^2 = \left(\frac{\partial P}{\partial\rho}\right)_S. \tag{2.62}$$

It is possible to define the constant

$$k_J = \frac{4\pi G\rho_0 a^2}{v_s^2}, \tag{2.63}$$

called Jeans wavenumber, and with it rewrite eq. (2.60),

$$\ddot{\delta}_k + 2H\dot{\delta}_k + 4\pi G\rho_0\left(\frac{k^2}{k_J^2} - 1\right)\delta_k = 0\,. \tag{2.64}$$

We can see that the Jeans wavenumber separates the gravitationally stable and unstable modes,

- $k \gg k_J$: we have that eq. (2.64) becomes

$$\ddot{\delta}_k + 2H\dot{\delta}_k + \frac{v_s^2 k^2}{a^2}\delta_k = 0\,, \tag{2.65}$$

  that is the equation of a damped harmonic oscillator. The solution is either overdamped or oscillatory with decreasing amplitude. The friction term is given by $2H\dot{\delta}$. In this case the perturbations do not grow.

- $k \ll k_J$: we have that eq. (2.64) becomes

$$\ddot{\delta}_k + 2H\dot{\delta}_k - 4\pi G\rho_0\delta_k = 0\,. \tag{2.66}$$

  In a matter Universe we know that $a(t)$ goes as eq. (2.18b), so we can compute $H(t)$ from eq. (2.3) and $\rho(t)$ from eq. (2.8), we obtain:

$$\ddot{\delta}_k + \frac{4}{3t}\dot{\delta}_k - \frac{2}{3t^2}\delta_k = 0\,, \tag{2.67}$$

  that has two solutions, one of which growing,

$$\delta_k \propto t^{2/3}\,. \tag{2.68}$$

So, in a matter-dominated epoch, perturbations can grow if $k \ll k_J$. If we consider a radiation-dominated epoch, we have that $a(t)$ goes as eq. (2.18a), so, from eq. (2.66), we obtain:

$$\ddot{\delta}_k + \frac{1}{t}\dot{\delta}_k = 0\,, \tag{2.69}$$

that has a solution in the form

$$\delta_k \propto A + B\log(t)\,, \tag{2.70}$$

where A and B are constants. so the growth is possible only if the perturbation has a non null initial velocity $\dot{\delta}_k(t_i)$, such as $B \neq 0$. Anyway, the growth is logarithmic, that means it's really slow compared to the previous case. That happens because in a radiation-dominated epoch the expansion rate is faster than it would be in a matter-dominated one, and the growth of perturbation is moderated. So the matter perturbations can grow only in a matter-dominated Universe. However before the decoupling, matter is strongly coupled to radiation, which implies a large sound speed $c/\sqrt{3}$, that contributes to wipe out the perturbations.

Is it possible to cast k_J in another form, by introducing the Jeans length,

$$\lambda_J \doteq \frac{2\pi}{k_J} . \tag{2.71}$$

In this case the condition for growing perturbations is $\lambda \gg \lambda_J$. In general the Jeans length has the following form:

$$\lambda_J \propto \frac{v_s}{\sqrt{\rho}} . \tag{2.72}$$

As we see, the sound speed opposes to the gravitational collapse, because faster perturbations dissipate easily, resulting in a large value of the Jeans length. On the other hand a larger density makes the collapse easier, because the gravitational field is stronger. Next to the Jeans length we can define the Jeans mass. It is the mass contained in a sphere of radius equal to the Jeans length,

$$M_J \propto \rho \lambda_J{}^3 . \tag{2.73}$$

The propagation of a perturbations of mass M is possible if $M > M_J$.

Chapter 3

Dark matter: evidence and detection

Astrophysical observations [3] show that baryonic matter accounts only for nearly 20% of the total amount of matter in the Universe. The other 80% is a new kind of matter that we are not able to detect and that, for this reason, is called *dark matter*. Understanding the nature of dark matter is certainly one of the most intriguing challenge in the scientific framework. A lot of scientists are working on this topic, trying to build a theory extending the Standard Model and comprising dark matter or to set up experiments in order to detect it. We will start off this chapter by talking about dark matter history, going through its experimental evidences and the possible candidates that are hypothesised, following the reviews [27–29]. Consequently we will focus on one candidate, the Weakly Interacting Massive Particle, talking about its importance in the dark matter searches, and its formation mechanism, referring to [24, 25, 30]. We will finally review the experimental aspects of dark matter searches and observations, giving an hint on their actual situation, following the reviews [31–36].

3.1   What is dark matter?

The development of the concept of *dark matter* has a long history in the astronomical framework. Scientists and philosophers always wondered if there could exist some form of matter that is imperceptible. It is from it that the adjective *dark* born. Astronomical objects can be observed because they emit light, or, on the other hand, they absorb light, and can be observed as well as dark regions. Light has always been the first way to survey the Universe and to trace its matter content. The first evidence we have is that astronomical bodies emit or absorb light in different way. We can quantify the emissivity by a quantity called light-to-mass ratio. However, we also know that not every astronomical object emit or absorb light. In general we can exploit light also to measure indirectly the mass of an astronomical object. Moreover, we can measure it by exploiting the gravitational theory, on the basis of the motion of close objects. However, the two estimates can be different: the gravitational mass sometimes exceeds the luminous mass estimate. From it astronomers have hypothesised the

presence of some kind of dark matter, that we can not see and that accounts for that discrepancy. We will now review the main evidences of dark matter.

Galaxy clusters

The first occurrence of a modern concept of dark matter in science was in the work of the astronomer Fritz Zwicky. He studied the redshift of various galaxy clusters finding that in the Coma cluster the velocity of individual galaxies with respect to the mean velocity of the cluster is higher than the expected value, computed from the estimated mass of the cluster, given by the sum of galaxies masses [1]. He concluded

> 'If this would be confirmed, we would get the surprising result that dark matter is present in much greater amount than luminous matter,'

that is actually referred as the first use of the words *dark matter* (inaccurately, as it was used before to indicate invisible matter). Although, Zwicky mentioned dark matter without referring to its actual meaning: he was assuming cool stars or gases. A similar conclusion was drawn by Sinclair Smith [37] while analysing the mass of the Virgo cluster, finding that the total amount of gravitational mass was much larger than the estimated mass by luminous matter. More discrepancies were then confirmed by other observations of individual pairs or groups of galaxies [38, 39], and the scientific community widely discussed the problem during the International Astronomical Union (IAU) General Assembly [40].

Rotation curves of galaxies

One of the most known results in the dark matter discovery is the observation of the rotation curves of galaxies, that is the circular velocity profile of its stars and gases as a function of their distance from the Galactic Centre. To measure the velocity distribution $v(r)$ until the edge of a galaxy, different techniques can be employed. For instance, velocity of hydrogen clouds are evaluated by measurement of the $21\,cm$ line of neutral hydrogen, because of its low level of absorption in the interstellar medium. Suppose that spiral galaxies are made of a central core (a disk and a bulge), containing the large part of galaxy mass, and an outer region. We can treat them as rigid bodies and compute, recalling Newtonian gravitational law,

$$v(r) = \sqrt{\frac{GM(r)}{r}}\,.$$
(3.1)

Considering the external region, we can set $M(r)$ constant from luminous matter observation, so that we have the velocity profile:

$$v(r) \propto r^{-1/2}\,,$$
(3.2)

expecting $v(r)$ to decrease with distance.

The first experimental result in this topic is due to Horace Babcock. In 1939 he presents the measurement of the rotation curve of galaxy M31 (i.e. Andromeda Galaxy) out to $20\,\mathrm{kpc}$ away from its centre [41]. He found inexplicably high velocities at large radii and, approximating M31 to a sphere surrounded by a flattened ellipsoid, he computed the mass distribution of it, finding a large mass-to-light ratio in the external region with respect to the centre. He interpreted the results as a strong gas absorption in the external region or as the existence of unknown dynamical considerations that would permit a lower mass there. Further measurement come from Jan Oort that studied the galaxy NGC 3115, finding a large mass-to-light ratio in the external region [42]. His student Hendrik C. van de Hulst predicted the $21\,\mathrm{cm}$ emission line of hydrogen, stating that it could be used to measure its velocity. Oort and van de Hulst measured the rotation curve of the galaxy M31 up to about $30\,\mathrm{kpc}$ away from the centre, finding that the mass-to-light ratio was higher in the outer regions [43]. Another measurement of the $21\,\mathrm{cm}$ line of M31 was done by Morton Roberts, confirming the previous results with more accuracy [44]. A step further in terms of quality was done by Kent Ford and Vera Rubin in 1970. They performed spectroscopic observations of M31 up to $30\,\mathrm{kpc}$ and determine that rotation velocity rises slowly with increasing distance from the centre of the galaxy, remaining almost constant over radial distances from $16\,\mathrm{kpc}$ to $30\,\mathrm{kpc}$ [2], confirming previous results and being in complete contrast with the theoretical prediction in eq. (3.2). In 1970 we have the appearance of the first statement arguing that additional mass was needed in the outer parts of the galaxies in order to account for galaxies rotational velocity observations. Ken Freeman compared the radius at which the rotation curve was observed to peak to the theoretically predicted radius obtained with an exponential distribution of matter (the distribution that basically matches the observed luminous matter) [45], and stated

> 'if [the data] are correct, then there must be in these galaxies additional matter which is undetected, either optically or at $21\,\mathrm{cm}$. Its mass must be at least as large as the mass of the detected galaxy, and its distribution must be quite different from the exponential distribution which holds for the optical galaxy.'

A few years later David H. Rogstad and G. S. Shostak analysed the rotation curves of the galaxies: M33, NGC 2403, IC 342, M101 and NGC 6946 [46], the results are shown in fig. 3.1. They noticed the same pattern, the rotation curves remain flat out to the largest radii observed. Moreover, it started to become clear that the optical radius can not be the edge of the galaxies. More and more studies confirmed this property for several galaxies and the astrophysical community widely accepted the conclusion that some invisible mass is present in galaxies.

Cosmic Microwave Background observations

In § 2.3 we have mentioned that the temperature of the Universe today is $T_0 = 2.73\,\mathrm{K}$ and that is due to the CMB radiation. Photons have decoupled from
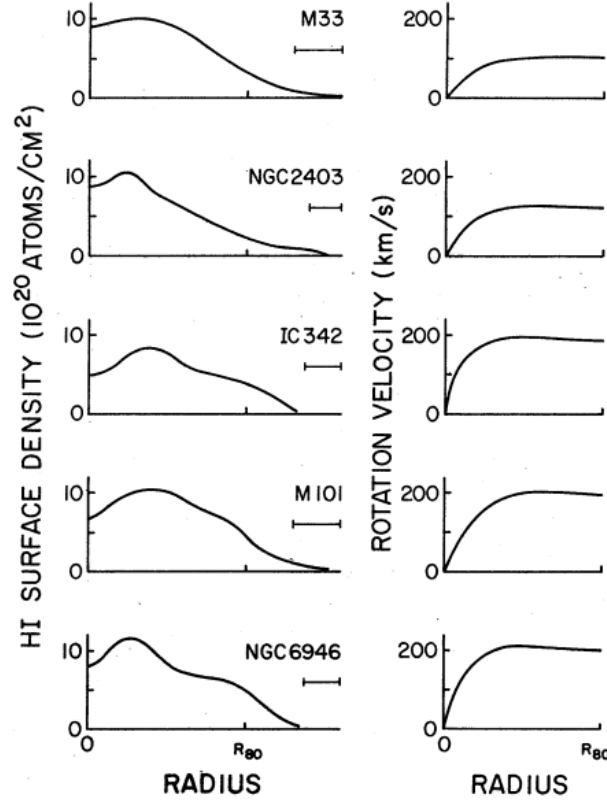
Figure 3.1: The hydrogen surface density profile (left) and the corresponding rotation curves (right) of the five galaxies studied by Rogstad and Shostak [46]. The bars under the galaxy names indicate the effective spatial resolution, while R_{80} is the radius containing the 80% of the observed hydrogen.

the electrons and has been streaming freely through the entire Universe, the CMB is made of the photons coming from the sphere's surface of last scattering with observer in the centre. The analysis of CMB temperature shows that its fluctuations are only $\Delta T/T \lesssim 10^{-5}$. That means CMB photons were causally connected and have the possibility to thermalise, a scenario today explained with the theory of inflation. Anyway, in § 2.5, we have studied a model explaining how density perturbations have grown during the evolution of the Universe. If density perturbations are adiabatic, then we should expect temperature fluctuations of the same order, recalling eq. (2.53), we have $\rho \propto T^4$, that means:

$$\delta_{\text{dec}} = \frac{\delta\rho}{\rho} \approx 3\frac{\Delta T}{T} \lesssim 10^{-5}\,. \tag{3.3}$$

Supposing that all known matter is baryonic, we can compute the value of the density fluctuation today, $\delta(t_0) = \delta_0$. From eq. (2.68) we can write:

$$\delta(t) = Ct^{2/3} = Ca(t)\,, \tag{3.4}$$

with C a simple constant that can be determined by imposing the initial condition at time t_{dec},

$$\delta_{dec} = C a_{dec} \Rightarrow C = \frac{\delta_{dec}}{a_{dec}} \,. \tag{3.5}$$

Therefore we have

$$\delta_0 = \frac{\delta_{dec}}{a_{dec}} a_0 \,. \tag{3.6}$$

We know that $a_0 = 1$, $\delta_{dec} \approx 10^{-5}$ and $a_{dec} \approx 1/1100$, so we compute

$$\delta_0 \approx 10^{-2} \,. \tag{3.7}$$

This result does not agree with the observation, that is $\delta_0 \approx 10^2$. We need a faster growth of the matter perturbations.

The way we can proceed is to introduce a dominant matter component with a negligible pressure term, that is the dark matter, indeed. In § 2.5 we analyse the case of baryonic perturbations: even though they can start growing after the time of equivalence, their growth is suppressed, as long as they are coupled to radiation. Dark matter behaves differently, we will see it decouples earlier than baryons and its perturbations can start growing just after the time of equivalence. So, after decoupling, baryonic perturbations growth is enhanced, because they can exploit the *holes* that dark matter left after its growth. This process is known as baryon catch-up. To compute it we start from the Jeans equation (2.60) for baryonic perturbation in the general case of a cosmological fluid made of different components, with $t > t_{dec}$,

$$\ddot{\delta}_{k,b} + 2H\dot{\delta}_{k,b} + \frac{v_s^2 k^2}{a^2}\delta_{k,b} - 4\pi G \sum_{i \in \{ \text{ components} \}} \rho_{i,0}\delta_{k,i} = 0 \,. \tag{3.8}$$

The sum over index i contains:

$$\sum_{i \in \{ \text{ components} \}} \rho_{i,0}\delta_{k,i} = \rho_{b,0}\delta_{k,b} + \rho_{DM,0}\delta_{k,DM} + \rho_{r,0}\delta_{k,r} \,. \tag{3.9}$$

We know that the density perturbations of the radiation are suppressed and we can assume that the Universe is dominated by dark matter energy density, so as $\rho_{DM,0} \gg \rho_{b,0}$. Moreover we are interested in the case of growing perturbations, $k \ll k_J$, meaning that we can neglect the term $v_s^2 k^2 a^{-2}$. We are left with

$$\ddot{\delta}_{k,b} + 2H\dot{\delta}_{k,b} - 4\pi G \rho_{DM,0}\delta_{k,DM} = 0 \,. \tag{3.10}$$

The solution of this equation is

$$\delta_{k,b}(t) = \delta_{k,DM}(t)\left(1 - \frac{a_{dec}}{a(t)}\right) , \tag{3.11}$$

the perturbations follows the growth of the dark matter, reaching it when $a(t) \gg a_{dec}$. The presence of dark matter can justify a faster growth of the baryonic perturbations, needed to match the observations.

An alternative: modified gravity paradigm

The need to hypothesise the presence of a new kind of invisible matter in order to account observations has given rise to speculations on the validity of Newton's Law. In 1982 Mordehai Milgrom published his work [47–49] in which he proposed a Modified Newtonian Dynamics (MOND) model that modifies Newton's Law for very low accelerations. This model is able to describe motion of stars and gas within galaxies without any need of dark matter. The Newton's Law results in the following modification:

$$F = m\frac{a^2}{a_0} \tag{3.12}$$

in the limit of very low accelerations $a \ll a_0$, where $a_0 \approx 1.2 \times 10^{-10}\,\mathrm{m\,s^{-2}}$. The MOND theory very well explains the constant galactic rotation curves [50, 51] for hundreds of galaxies and softens the mass discrepancy in galaxy clusters (though it has not been so successful, because significant quantities of dark matter are still required). However, MOND is a non-relativistic model and a relativistic formulation is quite difficult to accomplish. Only in 2004 a relativistic theory in the MOND framework was proposed by Jacob Bekenstein under the name of TeVeS, shorthand for Tensor-Vector-Scalar gravity [52]. TeVeS has become the leading theory of MOND and received great attention. Nevertheless, there are few cases in which MOND theory fails. The most known is the case of the Bullet Cluster, observed in 2006 [53]. It is a cosmological structure generated by the merging of two clusters. As a result of the collision, the distribution of stars and galaxies is separated from the hot X-ray emitting gas, which constitutes the majority of baryonic mass. Studying the lensing properties and the X-ray maps of the Bullet Cluster, astronomers have found out that the mass does not trace the distribution of baryons, so dark matter is required and it must dominate the mass of the system.

3.2   Cold, hot and warm dark matter

A first and simple classification of dark matter can be done by introducing three categories:

- cold dark matter (CDM): it decouples from radiation after becoming non-relativistic;

- hot dark matter (HDM): it decouples from radiation while still relativistic;

- warm dark matter (WDM): it is an intermediate case between HDM and CDM.

A particle with mass m becomes non-relativistic when $T \ll m$, so heavier particles becomes non-relativistic before lighter ones. Therefore, CDM and WDM candidates will be heavier than HDM ones. We can observe that HDM particles have a larger velocity than CDM, WDM particles at the time of decoupling,

because they are still relativistic particles. As we mentioned previously, dark matter is a type of collisionless matter, so its speed is not defined as the sound speed, meaning the ratio between the gradient of pressure and the gradient of density. The concept of speed of dark matter is intended as the thermal velocity, that is the dispersion velocity of the particles it is made of. Thermal velocities of dark matter particles have a direct influence on the structure formation. Indeed, they tend to erase perturbations below a certain scale, which depends both on the mass of the dark matter particle and on its formation mechanism. The length that a particle travels before the perturbations start to grow is called free-streaming length [54], defined as:

$$\lambda_{fs} \doteq \int_0^{t_{eq}} \frac{v(t)}{a(t)} \, dt \approx \int_0^{t_{nr}} \frac{c}{a(t)} \, dt + \int_{t_{nr}}^{t_{eq}} \frac{v(t)}{a(t)} \, dt \,, \tag{3.13}$$

with t_{nr} the epoch when the particle becomes non-relativistic. Below λ_{fs} all perturbations are wiped out. In the HDM scenario, dark matter particles are relativistic, we can easily infer that only large scale structures will form, being the λ_{fs} high.
In the same way, we can recall eq. (3.8):

$$\ddot{\delta}_{k,b} + 2H\dot{\delta}_{k,b} = \left[4\pi G\bar{\rho}(t) - \frac{v_s^2(t)k^2}{a^2}\delta_{k,b}\right]\delta_{k,i} \,, \tag{3.14}$$

where $\bar{\rho}(t)$ is defined as the sum in eq. (3.9). We can compute the Jeans mass, obtaining:

$$M_J = \frac{4}{3}\pi\rho_b(t)\left[\frac{\pi v_s^2(t)}{4G\bar{\rho}(t)}\right]^{3/2} . \tag{3.15}$$

We know that a perturbation can grow only if its mass is higher than the Jeans mass. In eq. (3.15) we see that M_J depends on time, in the sense that both the densities of the components and the velocity of dark matter depend on it. Therefore, it is possible to compute the maximum value of M_J, meaning the minimum value of mass that a perturbation must have in order to grow (see [25, 55] and references therein):

$$M_{min} \approx \begin{cases} 10^5 \div 10^6 M_\odot & \text{CDM,} \\ 10^{16} M_\odot & \text{HDM,} \\ 10^{11} M_\odot & \text{WDM.} \end{cases} \tag{3.16}$$

This gives rise to different scenarios in the structure formation:

- bottom-up: the first structures to collapse are the smaller ones, larger structures originates from the merging of them; this is the CDM scenario: dark matter particles move slowly, so the growth of small-scale perturbations is not suppressed, that means structure formation can begin earlier [56, 57];

- top-down: the first structures that can form are large scale *pancake*-like structures, that undergo fragmentation in smaller structures; this is the

HDM scenario: dark matter particles move with relativistic velocities, so they wash out small scale perturbations and structure formation begins relatively late [58–61];

- intermediate scenario: in the case of WDM, the structure formation is characterised by a top-down approach for formation of smaller structures and a bottom-up for larger ones; WDM candidates are faster than CDM candidates, and small structures are washed out.

The simulation of both scenarios and their comparison with observations of the Large Scale Structures suggest that a top-down approach is flawed, that means the HDM scenario is ruled out. In this project we will focus on CDM candidates.

3.3 Dark matter candidates

The existence of dark matter is well established, albeit the nature of its physical constituents is yet to be discovered. By the late 1980s, an increasing number of particle physicists became interested in the dark matter problem and the hypothesis that the missing mass might be made of unknown particles has gained more and more support. Today there is a widespread belief that dark matter is made of new particles. A good dark matter candidate must be neutral and stable on cosmological timescales and, in principle, there is a huge range of mass. Theory has provided a lot of dark matter candidates, we will now review the most studied ones. In general, dark matter may be made of several components, and not just one single particle.

Relic neutrinos

Standard model neutrinos were the first suggested candidates for dark matter. They have dark matter-like properties: they are neutral, massive, stable and they weakly interact with other particles. The adjective *relic* is referred to the fact that they have decoupled (see § 3.5 for reference) from radiation and has formed the Cosmic Neutrino Background [62]. After the decoupling, that happened at $T_{\nu,\text{dec}} \approx 1\,MeV$ neutrinos were no more in thermal equilibrium with electrons and photons, and their temperature followed eq. (2.35). Later on, temperature dropped below the mass of electron, so as they are no more part of the relativistic degrees of freedom. Their entropy transferred to photons and not to neutrinos. Computing the effective degrees of freedom of the components in thermal equilibrium we have:

$$g_\star^{\text{th}}(m_e < T < T_{\nu,\text{dec}}) = 2 + \frac{7}{8}(2 \cdot 2) = \frac{11}{2}\,, \qquad (3.17)$$

$$g_\star^{\text{th}}(T < m_e) = 2\,, \qquad (3.18)$$

so that T_γ changed from $T_\gamma = T_\nu$ to

$$T_\gamma = \left(\frac{11}{4}\right)^{1/3} T_\nu \,. \tag{3.19}$$

Knowing $T_{\gamma,0}$ we can compute $T_{\nu,0}$, and consequently $n_\nu(T_0)$ from eq. (2.29). Standard Model neutrinos have a small mass and at some point they have become non-relativistic. Therefore we can compute $\rho_\nu(T_0)$ with eq. (2.33) and their relic density results:

$$\Omega_\nu h^2 = \sum_{i \in \{\, e,\mu,\tau \,\}} \frac{m_i}{93\,eV} \,. \tag{3.20}$$

It is possible to constrain the sum of neutrino masses from PLANCK data [63], obtaining

$$\sum_{i \in \{\, e,\mu,\tau \,\}} m_i < 0.12\,eV \,, \tag{3.21}$$

however this constrains their relic density to

$$\Omega_\nu h^2 < 0.0013 \,, \tag{3.22}$$

that is too low to account for dark matter relic density (see eq. (3.49) [3]). Moreover, their low mass implies they are HDM candidates and we have previously seen how the structure formation mechanism in that paradigm is in contrast with observations.

Axions

Another (cold) dark matter candidates are the axions. They have been introduced in the study of Quantum Chromo Dynamics (QCD) to solve the strong CP problem. We can add the following term to the QCD lagrangian:

$$\mathcal{L}_{QCD} \supset \vartheta \frac{g_s^2}{21\pi^2} G^{a\mu\nu} \tilde{G}_{a\mu\nu} \,, \tag{3.23}$$

where g_s is the strong coupling constant and $\tilde{G}_{a\mu\nu}$ is the dual gluon field strength. The number ϑ is related to the vacuum phase, its value must be very low, $\vartheta \approx 1 \times 10^{-10}$ to account observations. Indeed, eq. (3.23) introduces a charge-parity violation that makes neutron electric dipole higher than expected, so we need to keep the contribution of this term low. In order to account for this value of ϑ, in 1977 Roberto Peccei and Helen Quinn proposed a model characterised by a new $U(1)$ global symmetry that is spontaneously broken and allows to drive the value of ϑ to zero [64]. The Goldstone boson associated with it is the pseudoscalar field a called axion. Its interaction lagrangian is:

$$\mathcal{L}_a = -\frac{g_s^2}{32\pi^2} \frac{a}{f_a} \varepsilon^{\mu\nu\rho\sigma} G^a_{\mu\nu} G^a_{\rho\sigma} \,, \tag{3.24}$$

where f_a is the scale at which the symmetry is broken. The axion acquires a small mass, proportional to f_a^{-1}. In order to describe a valid dark matter candidate, this particle has to be light and weakly interacting to avoid constraints from particle physics observations and therefore be stable on cosmological time scale.

Sterile neutrinos

The right-handed (sterile) neutrinos were proposed as a (warm) dark matter candidates in 1994 by Dodelson and Widrow [65]. They are siglet fermions that mix with the Standard Model left neutrinos. These particles are predicted by many extension of the Standard Model, for example in the type-I seesaw model, where we add n right-handed neutrinos to the Standard Model, see [66] for further details. As pointed out in [65], sterile neutrinos with a keV mass scale can play the role of warm dark matter (we have seen how lighter neutrinos are related to a top-down scenario for structure formation). These neutrinos are produced in the early Universe at high temperatures and, unlike other particles, their feeble interaction means that they were never in thermal equilibrium. Sterile neutrinos possesses a radiative loop-mediated decay $\nu_2 \to \nu_1 + \gamma$ [67], where ν_1, ν_2 are mass eigenstates with $m_{\nu_1} < m_{\nu_2}$. This produces a γ-ray line signature at half of the ν_s mass that can be exploited to detect them.

WIMPs

One of the most popular (cold) dark matter candidate is the Weakly Interacting Massive Particle (WIMP). As the name suggests, it is a massive particle interacting through weak interaction. The large interest around them is due to the fact that WIMPs can predict the correct value of the dark matter relic density easily, fact that is known as the WIMP miracle (see § 3.6). Examples of WIMPs can be found in supersymmetry, one of the most popular extension of the Standard Model.
In the beginning of 1970s, physicists considered to add a new symmetry able to relate bosons and fermions of the Standard Model [68–71], called supersymmetry. In the framework of supersymmetry, each particle has a superpartner, a particle having the same quantum number, but the spin, differing by 1/2. Lot of new particles has so been postulated. The most popular WIMP dark matter candidate coming from supersymmetry is the neutralino[*]. We will examine WIMPs in the following sections.

3.4   Boltzmann equation

In the early Universe, species were in thermal equilibrium. However there have been a certain number of departures from equilibrium as the temperature decreases. This phenomenon has allowed certain species to survive until now with a constant density. To compute this value and to describe how it has changed we need to analyse the moment of decoupling.
Consider a certain species in the Universe, in absence of interactions the

---

[*]Note that other non-WIMP dark matter candidates exist in supersymmetry such as the gravitino or axino.

number of particles per comoving volume, $N_i = n_i a^3$, is constant in time:

$$\frac{dN_i}{dt} = 0 \Rightarrow \frac{dn_i}{dt} a^3 + 3\frac{da}{dt} a^2 n_i = 0 \Rightarrow \frac{dn_i}{dt} + 3Hn_i = 0. \tag{3.25}$$

If we want to include the interactions, we need to add a collision term, regarding how the species interacts with the others:

$$\frac{1}{a^3} \frac{d}{dt}\left(n_i a^3\right) = \mathcal{C}_i\left[\{\,n_j\,\}\right]. \tag{3.26}$$

This is the Boltzmann equation.

Now we want to obtain a form for the Boltzmann equation for a dark matter particle χ. In thermal equilibrium it interacts with the other species. The collision term in eq. (3.26) is given by the depletion rate of dark matter particles $\sigma_{\chi\chi} v n_\chi^2$. The velocity v is not a fixed value, but a spectrum of velocities, following a certain distribution (Fermi-Dirac or Bose-Einstein). Therefore we need to average over that distribution, obtaining the following equation

$$\dot{n}_\chi(t) + 3Hn_\chi(t) = -\langle\sigma_{\chi\chi}v\rangle\left(n_\chi(t)^2 - n_\chi^{eq}(t)^2\right), \tag{3.27}$$

where we have

$$\langle\sigma_{\chi\chi}v\rangle = \int d^3v_1 d^3v_2 P_{\boldsymbol{r}}(\boldsymbol{v}_1) P_{\boldsymbol{r}}(\boldsymbol{v}_2)\sigma v, \tag{3.28}$$

with $P_{\boldsymbol{r}}(\boldsymbol{v}_i)$ being the velocity distribution of the ith particle at position $\boldsymbol{r}$, and $v = |\boldsymbol{v}_1 - \boldsymbol{v}_2|$ is the relative velocity.

3.5 Freeze-out

During the evolution of the Universe, processes that maintain species in equilibrium may become inefficient. When this happens the species freezes-out, that means its density, known as relic density becomes constant until today. To analyse the freeze-out we need to solve the Boltzmann equation. After defining the yield as

$$Y \doteq \frac{n_\chi}{T^3}, \tag{3.29}$$

we can express the Boltzmann equation as follow,

$$\frac{1}{a^3}\frac{d}{dt}\left(na^3\right) = -\langle\sigma_{\chi\chi}v\rangle\left(n_\chi^2 - n_\chi^{eq2}\right) \Rightarrow T^3\frac{d}{dt}\left(\frac{n}{T^3}\right) = -\langle\sigma_{\chi\chi}v\rangle T^6\left(\frac{n_\chi^2}{T^6} - \frac{n_\chi^{eq2}}{T^6}\right), \tag{3.30}$$

where we have used eq. (2.35) to express the temperature before decoupling. We obtain

$$\frac{dY(t)}{dt} = -\langle\sigma_{\chi\chi}v\rangle T(t)^3\left(Y(t)^2 - Y_{eq}(t)^2\right). \tag{3.31}$$

We can change the time variable in order to use $x = m_\chi/T$ that is better suited to keep track of the relativistic or non-relativistic nature of the dark matter. We

assume that the decoupling of dark matter happens in a radiation-dominated Universe. That means a scales as eq. (2.18a) and

$$H = \frac{\dot{a}}{a} = \frac{1}{2t} . \tag{3.32}$$

From eq. (2.8), with $k = 0$, $\rho_b \ll \rho_r$ and ρ_r given by eq. (2.38), we have

$$H = \left(\frac{8}{3} \pi G \rho_r \right)^{1/2} = \left(\frac{4}{45} \pi^3 G g_\star T^4 \right)^{1/2} = \frac{\left(\frac{4}{45} \pi^3 G g_\star m_\chi^4 \right)^{1/2}}{x^2} = \frac{H(m_\chi)}{x^2} , \tag{3.33}$$

that means we can write, from eq. (3.32)

$$\frac{dx}{dt} = \frac{d}{dt} \left(\sqrt{2tH(m_\chi)} \right) = \frac{H(m_\chi)}{x} , \tag{3.34}$$

so

$$\frac{d}{dt} = \frac{H(m_\chi)}{x} \frac{d}{dx} . \tag{3.35}$$

It is important to notice that the term $g_\star$ in eq. (3.33) is not constant during the evolution of the Universe and depends on the species that at each instant are decoupled. Here we make an approximation, considering it constant. This means that in our discussion we deal with high variations of temperature, covering however regions in which $g_\star$ may be considered constant. Substituting in eq. (3.31) we obtain

$$\frac{dY}{dx} = -\frac{\lambda}{x^2} \left(Y^2 - Y_{eq}^2 \right) , \tag{3.36}$$

with

$$\lambda \doteq \frac{\langle \sigma_{\chi\chi} v \rangle m_\chi^3}{H(m_\chi)} . \tag{3.37}$$

While in equilibrium, from eq. (2.29), the yield of the particles is given by

$$Y_{eq}(x) = \frac{\zeta(3)}{\pi^2} g_{eff} \qquad\qquad \text{relativistic,} \tag{3.38}$$

$$Y_{eq}(x) = \frac{g}{(2\pi)^{3/2}} x^{3/2} \exp(-x) \quad \text{non-relativistic,} \tag{3.39}$$

where $g_{eff} = g$ (bosons), $\frac{3}{4} g$ (fermions). We observe that in the relativistic regime the process in fig. 3.2 can happen in both direction: the equilibrium density of χ remains constant. In the non-relativistic regime, particles have not enough energy to produce a pair of χ particles. The only allowed process is the annihilation, so the equilibrium density drops. The Boltzmann equation in the form (3.36) is a particular type of Riccati equation, it has no analytical solution, so we need an approximate method to solve it. We can draw some qualitative conclusions. First of all, knowing that H can be expressed as eq. (3.33), and that the interaction rate Γ can be expressed as in eq. (2.37),

$$\Gamma = \langle \sigma_{\chi\chi} v \rangle n_\chi^{eq} = \frac{\langle \sigma_{\chi\chi} v \rangle m_\chi^3 Y_{eq}}{x^3} , \tag{3.40}$$
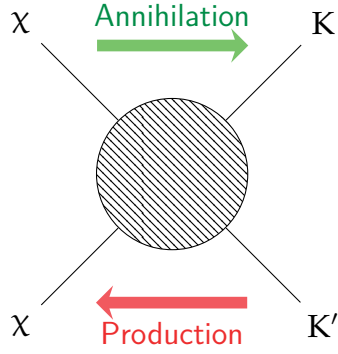
Figure 3.2: Annihilation and production processes involving χ and generic Standard Model particles K.

we can cast eq. (3.36) in the form

$$\frac{x}{Y_{eq}}\frac{dY}{dx} = -\frac{\Gamma}{H}\left(\frac{Y^2}{Y_{eq}^2} - 1\right). \tag{3.41}$$

As the temperature becomes lower (x increases), we have that Γ evolves as

$$\Gamma(x) \propto x^{-3} \qquad\qquad \text{relativistic,} \tag{3.42}$$

$$\Gamma(x) \propto x^{-3/2}\exp(-x) \quad \text{non-relativistic,} \tag{3.43}$$

so in both scenarios Γ decreases. It will reach the point in which annihilation processes become inefficient and freeze. This happens roughly when $\Gamma \approx H$, the moment of thermal decoupling; we will call the freeze-out point x_f. The ratio Γ/H in eq. (3.41) is a measure of the effectiveness of annihilations. Temperatures continue to decrease, so Γ/H does, the more this factor is small compared to 1, the more the relative change of the χ number density $\Delta Y/Y_{eq}$ is lower:

$$\frac{\Delta Y}{Y_{eq}} \sim \frac{x\frac{dY}{dx}}{Y_{eq}} \sim \frac{\Gamma}{H} < 1. \tag{3.44}$$

Therefore we expect that

$$Y(x) \approx Y_{eq}(x) \quad \text{for } x < x_f, \tag{3.45}$$

$$Y(x) \approx Y_{eq}(x_f) \quad \text{for } x > x_f, \tag{3.46}$$

the number density of χ tracks the equilibrium value before reaching the freeze-out point, at which it remains constant on the value it has when departing from equilibrium.

We can now analyse how freeze-out works for different types of dark matter:

- hot dark matter: the freeze-out occurs when the species is still relativistic, $x_f < 1$, when Y_{eq} is constant in time. That means the final value of Y does not depend on the value of x_f, resulting in $Y_\infty = Y_{eq}(x_f)$;
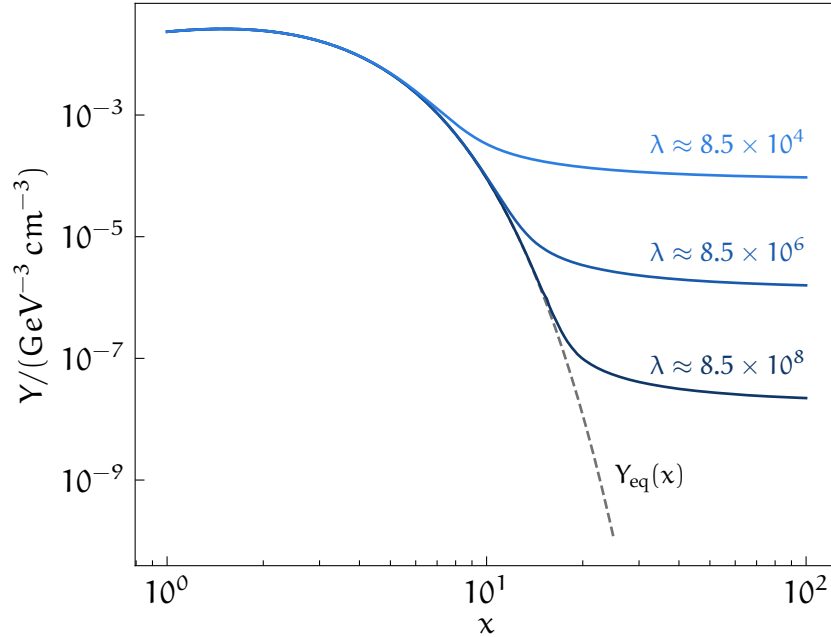
Figure 3.3: A graphical visualisation of the Boltzmann equation in the case of a cold relic. In the non-relativistic regime, the equilibrium density drops exponentially until the freeze-out point, at which it becomes constant. We can see that increasing values of λ are characterised by a lower relic density, due to a later freeze-out.

- cold dark matter: freeze-out happens when the species is non-relativistic, that means the details of freeze-out are important. When the particle becomes non-relativistic, the equilibrium density drops as eq. (3.39) until freeze-out. After freeze-out, the relic abundance is $Y(x) = Y(x_f)$, while $Y_{eq}(x)$ is exponentially suppressed, therefore we have $Y(x) \gg Y_{eq}(x)$, and eq. (3.36) becomes:

$$\frac{dY}{dx} = -\frac{\lambda}{x^2}Y^2 \, , \tag{3.47}$$

which can be solved by simply integrating from x_f to $+\infty$. If λ does not depend on x, we obtain a simple solution for the point $x' \gg x_f$:

$$Y(x') \approx \frac{x_f}{\lambda} \, , \tag{3.48}$$

by assuming $Y(x_f) \gg Y(x')$. That means the relic abundance at a given x_f decreases as λ increases. This is a direct consequences of the fact that λ is proportional to the interaction rate Γ, as can be seen by comparing eqs. (3.37) and (3.40). A graphical representation of these concepts is shown in fig. 3.3.
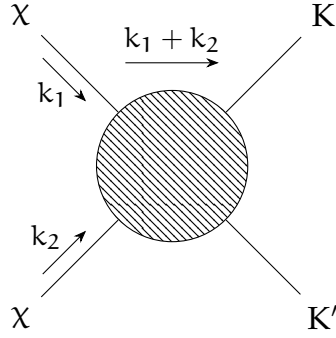
Figure 3.4: Annihilation of two WIMPs in Standard Model particles K.

3.6 WIMP miracle

When dark matter freezes-out after thermal decoupling, its density remains constant. The actual value of the relic density has been measured by the PLANCK experiment [3]

$$\Omega h^2|_{\text{PLANCK}} = 0.1200 \pm 0.0012 \,. \tag{3.49}$$

Therefore, when studying a dark matter model, we can infer strong constraints on the parameters space, in order to reproduce the measured relic density in eq. (3.49). From a theoretical point of view we can compute the relic density by solving the Boltzmann equation. We assume a CDM candidate that interacts through electroweak interaction, the so called WIMP. For example, in the annihilation process in fig. 3.4, we have $T \ll m_\chi$. We can write the cross section of the process according to electroweak theory, by implicitly assuming that $m_\chi \ll m_Z$, namely in Fermi limit of the theory:

$$\sigma_{\chi\chi} = \frac{\pi \alpha^2 m_\chi^2}{c_w^4 m_Z^4} \,, \tag{3.50}$$

where $c_w \doteq \cos \vartheta_w$ and ϑ_w is the Weinberg's angle. In order to compute $\langle \sigma_{\chi\chi} v \rangle$ we need to do the thermal average of eq. (3.50), because we have seen particles velocity follows a certain distribution (that may be a Fermi-Dirac or a Bose-Einstein distribution). Following eq. (3.28), we need the relative velocity of the particles. The velocity v_i of a particle with momentum $\mathbf{k}_i$ and energy k_i^0 is

$$v_i = \frac{|\mathbf{k}_i|}{k_i^0} \approx \frac{|\mathbf{k}_i|}{m_\chi} \ll 1 \,, \tag{3.51}$$

so that the relative velocity is

$$v = \left| \frac{\mathbf{k}_1}{k_1^0} - \frac{\mathbf{k}_2}{k_2^0} \right| \,. \tag{3.52}$$

Notice that the velocity of the particles is lower than 1 because we are in a non-relativistic scenario. We can compute the centre-of-mass energy in the centre

of momentum frame

$$s = (k_1 + k_2)^2 = 2m_\chi^2 + 2k_1^0 k_2^0 - 2\mathbf{k}_1 \cdot \mathbf{k}_2 = 2m_\chi^2 + 2(k_1^0)^2 + 2|\mathbf{k}_1|^2 = 4m_\chi^2 + 4|\mathbf{k}_1|^2$$
$$= 4m_\chi^2 (1 + v_1^2),$$

(3.53)

so we have

$$v_1{}^2 = \frac{s}{4m_\chi^2} - 1.$$

(3.54)

Turning back to eq. (3.52), it becomes

$$v = \left| \frac{\mathbf{k}_1}{k_1^0} + \frac{\mathbf{k}_1}{k_1^0} \right| = 2\frac{|\mathbf{k}_1|}{k_1^0} = 2v_1,$$

(3.55)

so that, using eq. (3.54) we compute

$$m_\chi^2 v^2 = 4m_\chi^2 v_1^2 = s - 4m_\chi^2.$$

(3.56)

Using this formalism, we can find a simple formula for the thermally averaged cross section. Considering the condition $T \lesssim 3m_\chi$, the velocity of χ particles follows approximately the Boltzmann distribution. We can write the thermally averaged cross section in the following way [72]

$$\langle \sigma_{\chi\chi} v \rangle = \frac{2\pi^2 T \int_{4m_\chi^2}^\infty ds \sqrt{s}(s - 4m_\chi^2) K_1\left(\frac{\sqrt{s}}{T}\right) \sigma_{\chi\chi}(s)}{\left(4\pi m_\chi^2 T K_2\left(\frac{m_\chi}{T}\right)\right)^2},$$

(3.57)

where $K_1(x)$, $K_2(x)$ are the modified Bessel functions of the second kind. This expression involves only a single integration. Moreover, when the condition $T \lesssim 3m_\chi$ is no longer satisfied, the velocity distribution of χ will be a Fermi-Dirac or a Bose-Einstein distribution, however we can still use safely eq. (3.57). To get an analytical estimation, we can consider an approximation for the relative velocity v at a given temperature T in a non-relativistic case:

$$\frac{1}{2}m_\chi v^2 = T \Rightarrow v = \sqrt{\frac{2T}{m_\chi}},$$

(3.58)

so that we can expand $\langle \sigma_{\chi\chi} v \rangle$ at first order in v,

$$\langle \sigma_{\chi\chi} v \rangle = \sigma_{\chi\chi} v + \mathcal{O}(v^2) = \frac{\pi \alpha^2 m_\chi^2}{c_w^4 m_Z^4} \sqrt{\frac{2T}{m_\chi}} + \mathcal{O}(v^2).$$

(3.59)

To compute the value of the relic density we need to integrate eq. (3.47), with λ given by eq. (3.37):

$$\lambda(x) = \frac{\langle \sigma_{\chi\chi} v \rangle m_\chi^3}{H(m_\chi)} = \left(\frac{2}{45}\pi G g_\star\right)^{-1/2} \frac{\alpha^2 m_\chi^3}{c_w^4 m_Z^4} \frac{1}{\sqrt{x}} + \mathcal{O}(v^2) \doteq \frac{\bar{\lambda}}{\sqrt{x}},$$

(3.60)

where we have made the substitutions according to eqs. (3.33) and (3.59) In order to have $\bar{\lambda}$ constant we need $g_\star$ constant. We consider two different temperature intervals:

- From $T \approx m_Z \approx 90\,\text{GeV}$ to $T \approx m_b \approx 5\,\text{GeV}$: this is the interval related to the electroweak energy scale. Above m_b, $g_\star$ does not change much, from eq. (2.39) we get:

$$g_\star(T) \approx 100\,, \tag{3.61}$$

because the only species that is non-relativistic is the top quark. For our purposes, it is useful to compute also the degrees of freedom in entropy, from eq. (2.47):

$$g_{\star S}(T) = g_\star(T)\,. \tag{3.62}$$

- From $T \approx m_b \approx 5\,\text{GeV}$ to today: when T falls below m_b, $g_\star$ drops dramatically, the today value is

$$g_\star(T_0) \approx 3.36\,, \tag{3.63}$$

given by the photons and the background of relativistic decoupled neutrinos. In the same way we compute $g_{\star S}$:

$$g_{\star S}(T_0) \approx 3.91\,. \tag{3.64}$$

For the first interval we integrate the Boltzmann equation (3.47) from the freeze-out point x_f to a point $x' \gg x_f$ above m_b:

$$\frac{dY}{dx} = -\frac{\overline{\lambda}}{x^{5/2}}Y^2 \Rightarrow Y(x') = \frac{x_f^{3/2}}{\overline{\lambda}} = \frac{x_f}{\lambda(x_f)}\,, \tag{3.65}$$

where we have assumed $Y(x') \ll Y(x_f)$. Now, $Y(x')$ evolves in the second temperature interval, where we are in a non-relativistic regime. We can exploit eq. (2.33) and the dependence in eq. (2.16b) to write:

$$\rho_\chi(T_0) = \rho_\chi(T')\left(\frac{a'}{a_0}\right)^3 = m_\chi Y(x')T'^3\left(\frac{a'}{a_0}\right)^3 = m_\chi Y(x')T_0^{\,3}\left(\frac{a'T'}{a_0 T_0}\right)^3\,. \tag{3.66}$$

Using the conservation of entropy, that brings to the proportionality expressed in eq. (2.51), we have

$$\left(\frac{a'T'}{a_0 T_0}\right)^3 = \frac{g_{\star S}(T_0)}{g_{\star S}(T')} \approx \frac{3.91}{100} \approx \frac{1}{25}\,. \tag{3.67}$$

Now we can compute the relic density from eq. (2.12)

$$\begin{aligned}
\Omega_\chi h^2 &\approx h^2 \frac{m_\chi Y(x')T_0^3}{25}\frac{8\pi G}{3H_0^2} = h^2 \frac{m_\chi T_0^3}{25}\frac{x_f H(m_\chi)}{\langle\sigma_{\chi\chi}v\rangle(x_f)\,m_\chi^3}\frac{8\pi G}{3H_0^2} \\
&\approx 0.12\,\frac{x_f}{23}\,\frac{\sqrt{g_\star(m_\chi)}}{10}\,\frac{1.7\times 10^{-9}\,\text{GeV}^{-2}}{\langle\sigma_{\chi\chi}v\rangle(x_f)}\,.
\end{aligned} \tag{3.68}$$

We can immediately notice that the relic density depends (approximately) only on the thermally averaged cross section:

$$\Omega h^2 \overset{\approx}{\propto} \frac{1}{\langle\sigma_{\chi\chi}v\rangle}\,, \tag{3.69}$$

that means only the ability of dark matter to interact is important to determine its current density. In order to finish the computation we need to find the freeze-out point x_f. As we know, at the moment of decoupling we have the rate of annihilation Γ equal to the rate of expansion of the Universe H:

$$\Gamma(x_f) = H(x_f). \tag{3.70}$$

We can substitute eqs. (3.33) and (3.40), with Y_{eq} given by eq. (3.39), the velocity v given by eq. (3.58) and g the number of relevant degrees of freedom of the WIMP:

$$\frac{\sigma_{\chi\chi} m_\chi^3}{x_f^3} \frac{g}{(2\pi)^{3/2}} x_f^{3/2} \exp(-x_f) \sqrt{\frac{2}{x_f}} = \left(\frac{4}{45}\pi^3 G\, g_\star(T_{dec}) m_\chi^4\right)^{1/2} \frac{1}{x_f^2} \tag{3.71}$$

$$\vdots$$

$$\exp(-x_f) = \frac{2}{3\sqrt{5}} \frac{\sqrt{g_\star(T_{dec})}}{g} \frac{\pi^3 \sqrt{G}}{\sigma_{\chi\chi} m_\chi}. \tag{3.72}$$

If we assume $g = 2$, corresponding to a complex scalar, we can solve the equation finding:

$$x_f \approx \begin{cases} 20 & \text{for } m_\chi = 10\,GeV, \\ 23 & \text{for } m_\chi = 30\,GeV, \\ 26 & \text{for } m_\chi = 60\,GeV. \end{cases} \tag{3.73}$$

Choosing for example $x_f = 23$, $m_\chi = 30\,GeV$ and computing the relic density with eq. (3.68), recalling eq. (3.59), we obtain

$$\Omega_\chi h^2 \approx 0.12 \frac{x_f}{23} \frac{\sqrt{g_\star(m_\chi)}}{10} \frac{c_w^4 m_Z^4}{\pi\alpha^2 m_\chi^2} \sqrt{\frac{x_f}{2}} 1.7 \times 10^{-9}\,GeV^{-2}$$

$$\approx 0.12 \left(\frac{x_f}{23}\right)^{3/2} \frac{\sqrt{g_\star(m_\chi)}}{10} \left(\frac{35\,GeV}{m_\chi}\right)^2 \tag{3.74}$$

$$\approx 0.12,$$

that is the value of the relic density measured by PLANCK (3.49). So, assuming a CDM candidate with an electroweak scale mass, whose annihilation process is mediated by weak interaction, we obtain a value of the relic density that is compatible with measurements. This fact is known as the WIMP miracle. In terms of thermal averaged cross section, from eq. (3.68) we find that it has to be nearly

$$\langle \sigma_{\chi\chi} v \rangle \approx 1.7 \times 10^{-9}\,GeV^{-2} \approx 3 \times 10^{-26}\,cm^3\,s^{-1}. \tag{3.75}$$

3.7 Coannihilation

Until now we have supposed dark matter consists of one single particle. However, in many models, the dark matter sector contains more than one particle. Suppose to have N different particles, labelled χ_i, with mass m_{χ_i}, such that $m_{\chi_i} < m_{\chi_j}$ if $i < j$. They annihilate in Standard Model particles K:

$$\chi_i \chi_j \to K\bar{K}', \tag{3.76}$$

and other processes are possible, as the elastic scattering,

$$\chi_i K \to \chi_j K', \tag{3.77}$$

or the decay of heavier states into lighter ones,

$$\chi_j \to \chi_i K K'. \tag{3.78}$$

If decays are rapid enough, then today we are left only with χ_1, that is the actual dark matter candidate, because it is the lightest particle in the dark matter sector. In the case of $N = 1$ we turn back to the simple case of one single particle with only one single process $\chi_1 \chi_1 \to K\bar{K}$ contributing to the relic density. In the general case, we have different annihilation processes, as in eq. (3.76) contributing to the relic density and they are much more efficient. The number density of each χ_i is n_i and their equilibrium density is n_i^{eq}, that follows eq. (2.32) with g_i degrees of freedom if we suppose all the χ_i's being non-relativistic. We can define the total equilibrium density

$$n = \sum_{i=1}^{N} n_i, \tag{3.79}$$

that determines the observed relic density. We can write a Boltzmann equation for each particle χ_i and obtain N different Boltzmann equations. Following the arguments in [73], as long as the equilibrium between the species is maintained with the processes in eq. (3.77), the ratios of abundances track their equilibrium value and we have

$$\frac{n_i}{n} \approx \frac{n_i^{eq}}{n^{eq}}, \tag{3.80}$$

that we can exploit in order to reduce the number of independent equations. At the end, we are left with only one Boltzmann equation, that governs the evolution of n:

$$\dot{n} + 3Hn = -\sum_{i=1}^{N} \langle \sigma v \rangle (n_i n_j - n_i^{eq} n_j^{eq}), \tag{3.81}$$

and that we can cast in

$$\dot{n} + 3Hn = -\langle \sigma_{\text{eff}} v \rangle (n^2 - n^{eq\,2}). \tag{3.82}$$

The term σ_{eff} is defined as:

$$\sigma_{\text{eff}} \doteq \sum_{i,j} \sigma_{ij} \frac{n_i^{eq} n_j^{eq}}{n^{eq\,2}}, \tag{3.83}$$

and can be expressed in the following way:

$$
\begin{aligned}
\sigma_{\text{eff}} &= \sum_{i=1}^{N} \sigma_{ij} \frac{g_i g_j \left(\frac{m_{\chi_i}}{m_{\chi_1}}\right)^{3/2} \left(\frac{m_{\chi_j}}{m_{\chi_1}}\right)^{3/2} \exp\left(-\frac{m_{\chi_i}+m_{\chi_j}-2m_{\chi_1}}{T}\right)}{\left(\sum_{k=1}^{N} g_k \left(\frac{m_{\chi_k}}{m_{\chi_1}}\right)^{3/2} \exp\left(-\frac{m_{\chi_k}-m_{\chi_1}}{T}\right)\right)^2} \\
&= \sum_{i=1}^{N} \sigma_{ij} \frac{g_i g_j (1+\Delta_i)^{3/2}(1+\Delta_j)^{3/2} \exp\left(-x(\Delta_i+\Delta_j)\right)}{\left(\sum_{k=1}^{N} g_k (1+\Delta_k)^{3/2} \exp(-x\Delta_k)\right)^2} \\
&= \sum_{i=1}^{N} \sigma_{ij} \frac{g_i g_j}{g_{\text{eff}}^2} (1+\Delta_i)^{3/2}(1+\Delta_j)^{3/2} \exp\left(-x(\Delta_i+\Delta_j)\right),
\end{aligned}
\tag{3.84}
$$

where $\Delta_i \doteq (m_{\chi_i} - m_{\chi_1})/m_{\chi_1}$, $x = m_{\chi_1}/T$ and

$$
g_{\text{eff}} \doteq \sum_{k=1}^{N} g_k (1+\Delta_k)^{3/2} \exp(-x\Delta_k). \tag{3.85}
$$

We can further suppose that all the χ_i's have similar masses. In this case the exponential suppression $\exp(-x\Delta_i)$ is not too high. The annihilation is more efficient and $\langle \sigma_{\text{eff}} v \rangle$ is in general higher than only $\langle \sigma_1 v \rangle$, when we have only one particle belonging to the dark matter sector. In the WIMP case we can reproduce the correct value of the relic density, by having $\langle \sigma v \rangle$ as in eq. (3.75). In the case of coannihilation, $\langle \sigma v \rangle$ contains contributions from the various channels in eq. (3.76), while $\langle \sigma_1 v \rangle$ due to $\chi_1 \chi_1 \to K\bar{K}$ is smaller. We can exploit the proportionality $\langle \sigma_1 v \rangle \propto s^{-1} \propto m_{\chi_1}^{-2}$ and see that a lower value of $\langle \sigma_1 v \rangle$ translates into an higher value of m_{χ_1}.

3.8   The dark matter hunt

The search of dark matter relies on its interactions with other particles. Assuming that the actual observed relic density comes from the freeze-out mechanism, we can assume that dark matter interacts not only gravitationally. Indeed, we saw how a weakly interacting candidate is suitable to predict the correct observed value of the relic density. Therefore searches for dark matter can be done by looking at its interactions with other particles. There are different way to proceed:

- indirect detection: aims to look at the products of the annihilation processes involving dark matter particles;

- direct detection: aims to detect dark matter elastic scatterings off Standard Model's particles;

- collider searches: aim to produce dark matter particles via the scattering of particles in a collider.
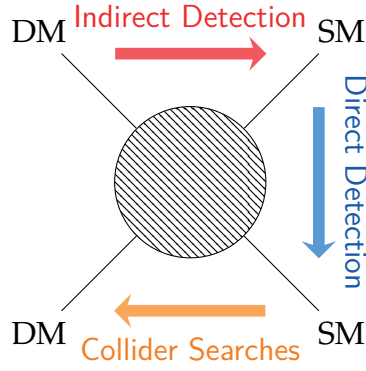
Figure 3.5: A graphical representation of the detection methods of dark matter (DM), with respect to Standard Model (SM). The arrows go from the initial particles to the final ones.

A graphical representation of the three different approaches can be found in fig. 3.5.

In the next sections we will review the main characteristics of these methods In this thesis we will focus on indirect detection.

3.9   Indirect detection

In § 3.5 we saw that dark matter's density drops when particles become non-relativistic until the annihilation process becomes suppressed. After that, the comoving number density remains constant until now, but its distribution changed considerably during the structure formation. In particular, dark matter is concentrated in areas with a large amount of gravitational matter, and formed structures called halos. In halos the dark matter density has a peak so the annihilation process is significantly enhanced. In those regions the annihilation of dark matter is active today, so we can detect the products coming from it. Dark matter particles are nearly at rest in halos, because their kinetic energy is very small. Therefore, the centre-of-mass energy of annihilation processes is simply given by $\sqrt{s} \approx 2m_\chi$, where χ is the dark matter candidate. The self-annihilation of dark matter particles can produce any pair of kinematically allowed particles. Those can be either stable particles of the Standard Model or unstable ones, which undergo decays and hadronisation in stable particles as photons, neutrinos, protons, antiprotons or heavy nuclei. Some examples of dark matter interaction processes are:

$$\chi\chi \to \ell^+\ell^- \,, \tag{3.86a}$$

$$\chi\chi \to q\bar{q} \to p\bar{p} + X \,, \tag{3.86b}$$

$$\chi\chi \to \tau^+\tau^-, W^+W^-, b\bar{b} + X \to \ell^+\ell^-, p\bar{p} + X \,, \tag{3.86c}$$

where ℓ is a lepton, q is a quark, p is the proton and X is any possible extra QCD radiation in that event. Antiparticles are rarer and so can give a distinctive signal.

The different products of dark matter annihilation follow different paths before reaching our detectors. Charged particles do not follow a straight path, they interact easily with interstellar gas and will diffuse in the galactic magnetic fields, so we do not get any directional information from them. Those particles constitute the Cosmic Rays, that can be studied by modeling their propagation, and matching the observed fluxes, in the hypothesis of a dark matter origin. The other possible final state is given by neutral particles, such as photons or neutrinos. In this case they propagate in a straight line, and we can infer their trajectory. Neutrinos travel basically undisturbed in the galaxy. They can be detected with large Čerenkov detectors, by analysing the interaction products of neutrinos with the medium in the detector volume. Conversely, photons are easier to detect, but they are characterised by larger background. Looking into indirect detection in γ-rays, dark matter can produce different photon's spectra:

1. Hadronic, eqs. (3.86b) and (3.86c): dark matter annihilates to $\tau^+\tau^-$, gauge bosons or any combination of quarks. A large number of pions are produced by subsequent decays. The neutral ones decay in photons pairs $\pi^0 \to \gamma\gamma$ with a 99% branching ratio, producing a photon-rich spectrum, along with electrons and positrons from the decay of charged pions. The outcome of this processes is a continuum spectrum of photons.

2. Leptonic, eq. (3.86a): dark matter annihilates predominantly to electrons and muons. Photons can be produced only as a part of three body decays, via final state radiation or internal bremsstrahlung. The rate of photon production is suppressed and copious charged leptons are produced. The photons spectrum will be continuum, characterised by a peak towards the dark matter mass.

3. Line: dark matter annihilates directly to $\gamma\gamma$. It is a two-body process, so the photons have fixed energy and their spectrum is given by a monoenergetic line with energy $E_\gamma \approx m_\chi$. This channel is extremely promising for what concerns astrophysical backgrounds: it is indeed difficult to explain a γ-ray spectral line with conventional astrophysics. However dark matter carries no charge, thus it can not couple directly to photons: this can happen only via a loop diagram, that means the process is suppressed and the signal is expected to be small. This kind of processes, without a tree level diagram, are called loop-induced processes.

Photon flux

As we saw, photons reach Earth in a straight line from the point of dark matter annihilation, hitting our detector. Our view of the sky is two-dimensional, therefore detected photons are characterised by a certain solid angle $\Delta\Omega$ in the sky within a time interval Δt. Suppose the signal arising from a volume ΔV expressed

in spherical coordinates (r', ϑ, φ), where Earth is in the origin of the coordinates, and suppose our detector has area A. Moreover, consider a Majorana fermion[†] dark matter candidate and suppose that it annihilates into a certain particle i with branching ratio of $\mathcal{B}_i$ and that each annihilation produces a spectrum $\frac{dN_\gamma^i}{dE_\gamma}$ of photons. Finally, suppose their energy does not change between production and detection (so we neglect redshift and absorption, which is a good approximation for galactic signals). The number ΔN_γ of photons received within a certain energy ΔE in a time interval Δt is:

$$\frac{\Delta N_\gamma}{\Delta E_\gamma \Delta t \Delta V} = \sum_i \mathcal{B}_i \frac{dN_\gamma^i}{dE_\gamma} \frac{A}{4\pi r'^2} \frac{1}{2} \langle \sigma v \rangle \, n(\mathbf{r})^2 \,, \tag{3.87}$$

where $\mathbf{r} = \mathbf{r}(\mathbf{r}')$ is the coordinate of the annihilation point with respect to the centre of the dark matter source. In the limit of a localised source, small time and energy intervals we have:

$$\frac{d^2 \Phi_\gamma}{dE_\gamma \, dV} = \sum_i \mathcal{B}_i \frac{dN_\gamma^i}{dE_\gamma} \frac{A}{8\pi r'^2} \langle \sigma v \rangle \frac{\rho(\mathbf{r})^2}{m_\chi^2} \,, \tag{3.88}$$

where we have defined the flux of photons

$$\Phi_\gamma \doteq \frac{dN_\gamma}{dt} \,, \tag{3.89}$$

and the number density

$$n(\mathbf{r}) = \frac{\rho(\mathbf{r})}{m_\chi} \,. \tag{3.90}$$

We can integrate over the solid angle and along the line of sight (l.o.s.), that is the distance from the observer to the annihilation event, recalling that in spherical coordinates $dV = r'^2 \, d\Omega \, dr'$:

$$\frac{d\Phi_\gamma}{dE_\gamma} = \sum_i \mathcal{B}_i \frac{dN_\gamma^i}{dE_\gamma} \frac{A}{8\pi m_\chi^2} \langle \sigma v \rangle \int_{\Delta\Omega} d\Omega \int_{\text{l.o.s.}} dr' \, \rho\big(\mathbf{r}(r', \Omega)\big)^2 \,. \tag{3.91}$$

The last expression can be split in two parts: the first one related to particle physics and the other one related to the distribution of dark matter mass density. That can be determine with the help of N-body simulations or by gravitational measurements. We define the J-factor of the source in the following way:

$$J \doteq \frac{1}{8\pi} \int_{\Delta\Omega} d\Omega \int_{\text{l.o.s.}} dr \, \rho\big(\mathbf{r}(r', \Omega)\big)^2 \,. \tag{3.92}$$

The distribution of dark matter is a key input for indirect detection. We can model for simplicity $\rho(\mathbf{r})$ as a spherically-symmetric distribution, so that $\rho(\mathbf{r}) = \rho(r)$ and introduce the following standard density profiles:

[†]If it is not, the next formulae will have a factor $1/2$.

- generalised Navarro-Frenk-White (NFW) profile [74]:

$$\rho_{\mathrm{NFW}}(r) = \rho_0 \left(\frac{r}{r_s}\right)^{-\gamma} \left(1 + \frac{r}{r_s}\right)^{\gamma - 3}, \tag{3.93}$$

where r_s is the scale radius. The NFW profile is an example of a cuspy profile. The $\gamma = 1$ case corresponds to the canonical NFW profile. As ρ_0 we can use the dark matter density at the Sun position $\rho_\odot$;

- Einasto profile [75]:

$$\rho_{\mathrm{Ein}}(r) = \rho_0 \exp\left\{-\frac{2}{\alpha}\left[\left(\frac{r}{r_s}\right)^\alpha - 1\right]\right\}, \tag{3.94}$$

with the scale radius r_s and the parameter α, which controls the curvature of the profile;

- Burkert profile [76]:

$$\rho_{\mathrm{Bur}}(r) = \rho_0 \left(1 + \frac{r}{r_s}\right)^{-1} \left(1 + \frac{r^2}{r_s^2}\right)^{-1}, \tag{3.95}$$

where, again, r_s is the radius. The Burkert profile is an example of a cored profile, meaning that it is characterised by a flatter density behaviour.

In the case of the Milky Way, the values of the free parameters can be read in [77]. In fig. 3.6 we show an illustration of the three profiles, we see that the differences between the NFW and Einasto profiles are marginal, while the Burkert profile shows a reduced dark matter density in the centre of the halo. The three profiles describe the dark matter density following a smooth pattern. The particle physics part is instead related to the thermally averaged cross section $\langle \sigma v \rangle$, already defined in eq. (3.28). We can express it in terms of the centre-of-mass velocity $v_{\mathrm{CM}} = (v_1 + v_2)/2$ and the relative velocity $v = v_2 - v_1$:

$$\langle \sigma v \rangle = \int dv\, \tilde{P}_r(v) \sigma v, \tag{3.96}$$

with

$$\tilde{P}_r(v) \doteq 4\pi v^2 \int d^3 v_{\mathrm{CM}}\, P_r\left(v_{\mathrm{CM}} + \frac{v}{2}\right) P_r\left(v_{\mathrm{CM}} - \frac{v}{2}\right). \tag{3.97}$$

Considering a Maxwell-Boltzmann distribution $P_r(v) = \pi^{-3/2} v_0^{-3} \exp\left(-v^2/v_0^2\right)$ with most probable velocity v_0, also the relative velocity will follows a Maxwell-Boltzmann distribution with most probable velocity $\sqrt{2}v_0$:

$$\tilde{P}_r(v) = \sqrt{\frac{2}{\pi}} \frac{v^2}{v_0^3} \exp\left(-\frac{v^2}{2v_0^2}\right). \tag{3.98}$$

As we have pointed out before, dark matter annihilates nearly at rest (tipically $v_0 \approx 1 \times 10^{-3}$), because it is non-relativistic, so we can expand the cross section in powers of v:

$$\sigma v = a + bv^2 + \mathcal{O}\left(v^4\right), \tag{3.99}$$
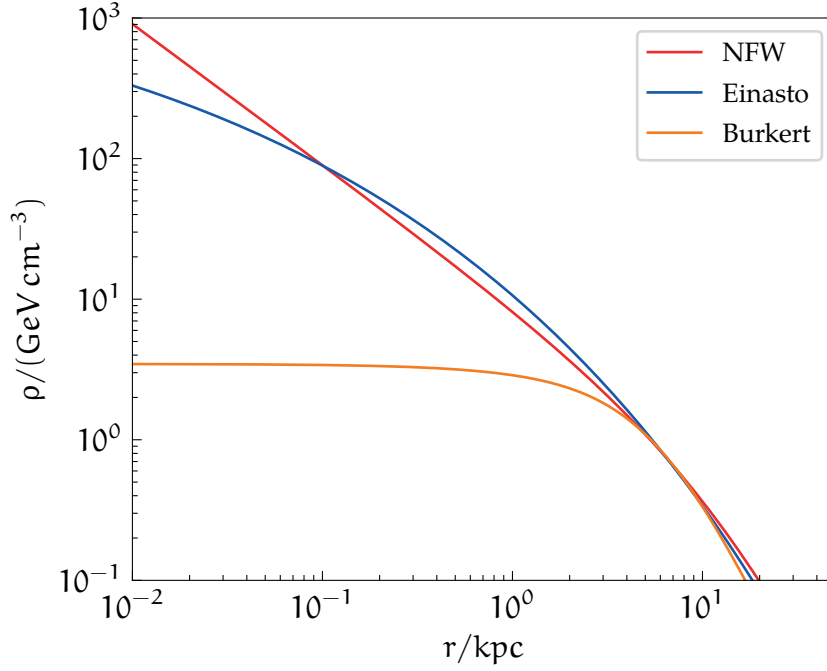
Figure 3.6: Illustration of the standard density profiles. Parameters are normalised to the Milky Way, we have taken the mean values reported in [77].

the a and b factors are related, related respectively to the s-wave and p-wave contribution to the cross section. For a p-wave dominated cross section we can compute $\langle \sigma v \rangle = 3bv_0^2$ considering b constant. In this approximation the velocity averaging is equivalent to the evaluation of σv, with $v = \sqrt{3}v_0$.

Recent experiments and results

In eq. (3.91) we have seen that the astrophysical contribution is a key parameter for indirect searches of dark matter. In particular, the J-factor plays an important role, the higher it is, the stronger will be the signal. Therefore, the best locations to search for dark matter are those with an extraordinary matter density, in order to have an high J-factor, so that annihilation is enhanced. One of the most prominent target is given by the Milky-Way Galactic Centre, containing a huge variety of large substructures, such as the central black hole *Sag A**, supernovae remnants, neutron stars and pulsars. The Galactic Centre is a very bright objective for γ-ray searches, though it is a challenging region, due to a multiplicity of astrophysical backgrounds:

- cosmic-ray protons striking interstellar gas, producing pions that decays in photons;

- cosmic-ray electrons interacting with the electromagnetic field of interstellar gas, producing photons via bremsstrahlung;

- production of high energy photons, by inverse Compton scattering, due to cosmic-ray electrons interacting with starlight;

- synchrotron radiation produced by the propagation of cosmic-ray electrons in the strong magnetic fields of the galaxy.

Dealing with the large background of the Galactic Centre is not a simple task for experiments. However, we have seen that the annihilation of dark matter in a pair of photons produces a line spectrum. This signature is basically free of background and is a promising target for indirect detection.

The analysis of it is the main topic of this thesis.

The Galactic Centre has been investigated for a γ-ray line signal. The experiments FERMI-LAT and HESS have placed upper limits [19, 20] on it, over the GeV and TeV regions in the dark matter mass. These limits have been obtained for different dark matter density profiles and in this thesis we will use them to constrain the parameters space of two dark matter models. They are shown in fig. 3.7. The Galactic Centre has also been surveyed for a continuum γ-ray spectrum. Different experiments have found interesting signals, that still lack of a conclusive explanation. The first example is the so called Galactic Centre Excess, found by [78–80] and later confirmed by the FERMI Collaboration [81]. They have observed a peak in the continuum γ-ray spectrum arising from the Galactic Centre and the inner Galaxy at approximately $10°$ from the Galactic Centre. There are different hypothesis about its origin: a dark matter annihilation contribution is promising, but there is also a possible explanation in terms of an unseen population of pulsars [82].

Although the Galactic Centre is a perfect objective for dark matter searches, dealing with its high γ-ray background is quite challenging. For this reason, another promising targets for indirect detection of photons are the dwarf spheroidal galaxies (dSphs), satellite of the Milky Way. They are small, low-luminosity spherical-shaped galaxies, hosting few old stars and little gas, so that they are essentially free of γ-ray background. Moreover, they are believed to be dark matter dominated [83]. This features makes them good targets for γ-ray detection, even if their J-factors are lower than the Galactic Centre one. The FERMI-LAT and HESS collaborations have carried out researches [84, 85] in order to find signatures of dark matter annihilation, placing limits on the thermally averaged cross section for various channels.

Another interesting channel for indirect detection is given by the cosmic rays. The flux of electrons and positrons has been measured by PAMELA in 2008 [86], and it was observed an increase in the positron fraction $N_{e^+}/(N_{e^+} + N_{e^-})$ for energies above $10\,GeV$. This phenomena was confirmed also by FERMI [87] and AMS-02 [88], that observed a rise up to $300\,GeV$. This excess implies the presence of a new source of positron. We can explain this feature with dark matter, that can in principle annihilates and supply another source of positron. However the excess can also be explained with conventional astrophysics, supposing that it is generated by a pulsar [89].

(a)

(b)

(c)
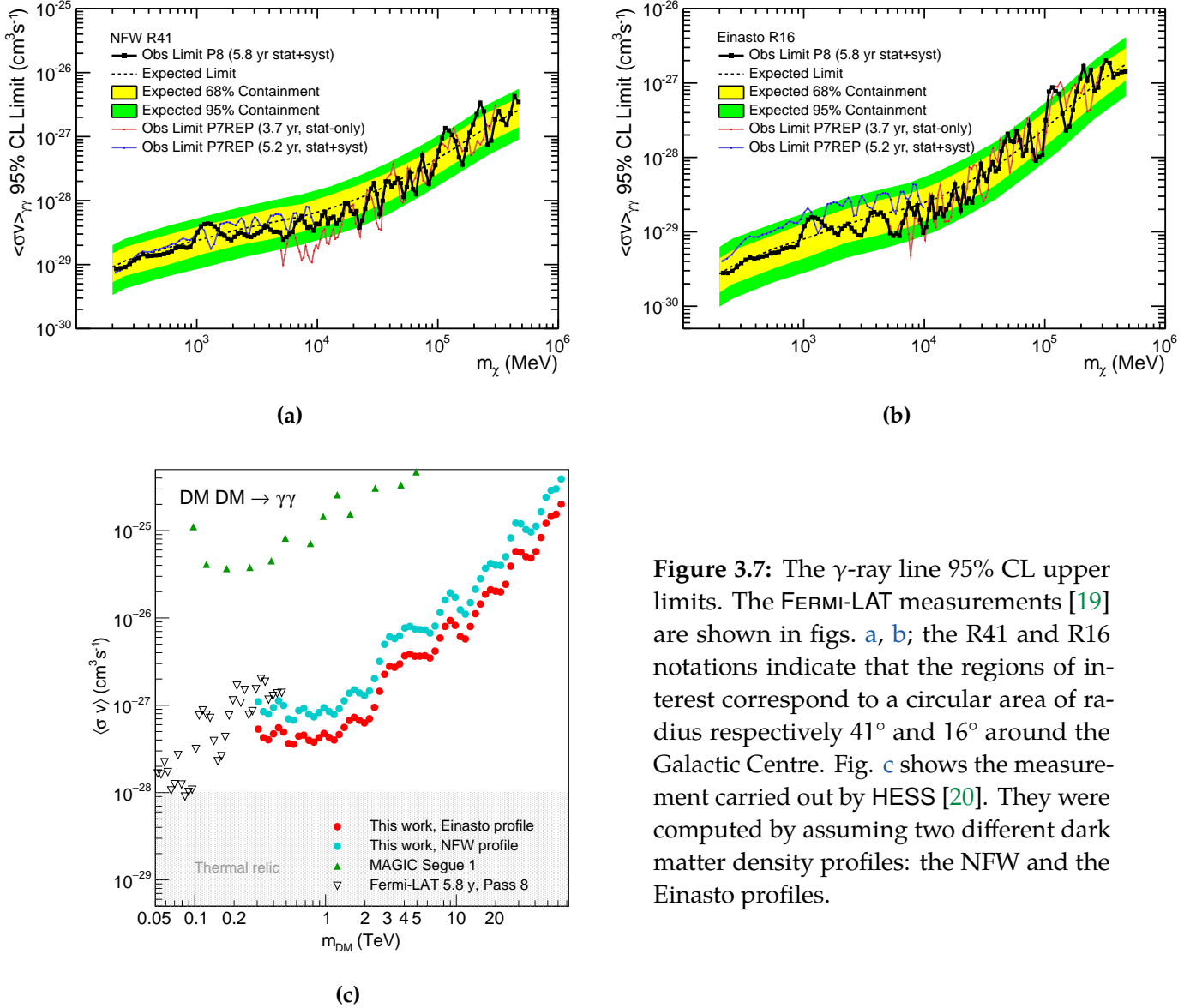
Figure 3.7: The γ-ray line 95% CL upper limits. The FERMI-LAT measurements [19] are shown in figs. a, b; the R41 and R16 notations indicate that the regions of interest correspond to a circular area of radius respectively 41° and 16° around the Galactic Centre. Fig. c shows the measurement carried out by HESS [20]. They were computed by assuming two different dark matter density profiles: the NFW and the Einasto profiles.

3.10 Direct detection

Direct detection experiments rely on the scattering of dark matter particles in the Milky Way halo in a detector on Earth. Dark matter elastically scatters off the atomic nucleus and the momentum transfer gives rise to a nuclear recoil, that is detectable. Direct detection detectors are usually set up undergrounds: they must be shielded from cosmic radiation and natural radioactivity, that are the most important backgrounds. The signal can be detected by exploiting three different phenomena: energy deposition in calorimeters, scintillation light and ionisation. The rate of WIMPs scattering off atomic nucleus depends both on dark matter astrophysical properties and on particle physics one. From an astrophysical point of view we need to consider the local dark matter density $\rho_0 \approx (0.39 \pm 0.03)\,\text{GeV}\,\text{cm}^{-3}$ [90], the velocity distribution in the laboratory frame $f(\boldsymbol{v}, t)$ of the dark matter particles in the halo and the dark matter mass m_χ.

From a particle physics perspective, the important parameters are the nuclear recoil energy E_R and the scattering cross section σ. We obtain the rate R:

$$\frac{dR}{dE_R} = \frac{\rho_0 M}{m_N m_\chi} \int_{v_{min}}^{v_{esc}} v f(v, t) \frac{d\sigma}{dE_R} \, dv \,, \tag{3.100}$$

where M is the target mass of the detector. The velocity $v_{esc} \approx 544 \, \mathrm{km \, s^{-1}}$ [91] is the escape velocity of dark matter particles, above this value dark matter is no more bounded to the potential well of the Milky Way, while the minimum velocity v_{min} to have a recoil in an elastic scattering case is

$$v_{min} = \sqrt{\frac{E_R m_N}{2\mu_N^2}} \,, \tag{3.101}$$

where μ_N is the reduced mass of the WIMP-nucleus system, m_N being the nucleus mass,

$$\mu_N = \frac{m_N m_\chi}{m_N + m_\chi} \,. \tag{3.102}$$

The velocity distribution of dark matter particles in the laboratory frame is subjected to an annual modulation due to the relative motion of Earth orbiting around the Sun and of the Sun orbiting around the Milky Way centre. Considering the distribution $\tilde{f}(v)$ of dark matter velocity with respect to the Galactic Centre we can make a Galileian boost:

$$f(v, t) = \tilde{f}(v_{obs}(t) + v) \,, \tag{3.103}$$

where

$$v_{obs}(t) = v_\odot + v_\oplus(t) \tag{3.104}$$

is the motion of the laboratory frame with respect to the Galactic Centre, with $v_\odot$ being the velocity of the Sun and $v_\oplus$ the velocity of the Earth in that frame. A simple description of the dark matter halo is achieved by the Standard Halo Model (SHM) [92]: we consider the galactic halo as a smooth, isotropic and spherically symmetric halo, characterised by a Maxwell-Boltzmann velocity distribution $\tilde{f}(v)$

$$\tilde{f}(v) = \frac{1}{N} \left(\frac{1}{\pi v_0^2} \right)^{3/2} \exp\left(-\frac{|v|^2}{v_0^2} \right) \,, \tag{3.105}$$

with N being a normalisation constant and v_0 is the most probable velocity. In the framework of the SHM, v_0 is the average velocity of the material around the Galactic Centre, that is the velocity of the Local Standard of Rest, an ideal point moving on a perfectly circular orbit around the Galactic Centre at the same distance as the Sun. In the galactic coordinates[‡] we have $v_0 \approx (0, 235, 0) \, \mathrm{km \, s^{-1}}$ [93]. The Sun motion in galactic coordinates is [94]:

$$v_\odot \approx v_0 + (-11, 12, 7) \, \mathrm{km \, s^{-1}} \,. \tag{3.106}$$

[‡]The galactic reference frame is a cylindrical frame centered in the Galactic Centre and coordinates $(r, \vartheta, z) = r\,\hat{r} + \vartheta\,\hat{\vartheta} + z\,\hat{z}$, with $\hat{r}$ pointing away from the Galactic Centre, $\hat{z}$ pointing to the galactic north and $\hat{\vartheta} = \hat{r} \times \hat{z}$.

The velocity of Earth can be expressed through the following expression:

$$\boldsymbol{v}_\oplus \approx v_\oplus \cos(\vartheta) \cos\big(\omega(t - t_0)\big), \tag{3.107}$$

with $\omega = 2\pi/T$, $T = 1$ year, t_0 is chosen in order to measure the maximum value of $|\boldsymbol{v}_\oplus|$ when $t = t_0$, $\vartheta \approx 60°$ is the inclination angle between Earth's orbit and the galactic plane, while $v_\oplus \approx 30\,\mathrm{km\,s^{-1}}$.

Dark matter particles scatter off with a non-relativistic velocity, so that its de Broglie wavelength is small, compared to the nucleon's wavelength. Therefore, dark matter can not resolve the nucleons inside a nucleus, but it scatters off the entire atomic nucleus. The WIMP-nucleus scattering cross section depends on the recoil energy and on the velocity:

$$\frac{d\sigma}{dE_R} = \frac{2m_N}{\pi v^2} \big\langle |\mathcal{A}_{NR}|^2 \big\rangle, \tag{3.108}$$

where $\mathcal{A}_{NR}$ is the non-relativistic limit of the scattering amplitude. It is possible to study the amplitude using an effective approach: we have a spin-independent (SI) cross section (with a scalar $\mathcal{L}_S \sim \bar\chi\chi\bar{N}N$ or vector-mediated $\mathcal{L}_V \sim \bar\chi\gamma^\mu\chi\bar{N}\gamma_\mu N$ effective vertex) and a spin-dependent (SD) cross sections (characterised by an axial-vector $\mathcal{L}_A \sim \bar\chi\gamma^\mu\gamma^5\chi\bar{N}\gamma_\mu\gamma^5 N$ effective vertex).

In the spin-independent case we have:

$$\frac{d\sigma}{dE_R} = \frac{2m_N}{\pi v^2} \Big[Zf_p + (A - Z)f_n \Big]^2 F_{SI}^2(E_R), \tag{3.109}$$

where f_n, f_p are the WIMP couplings to neutrons and protons respectively. The term $F_{SI}(E_R)$ is the nuclear form factor. Each interaction is characterised by the momentum transfer $q = \sqrt{2m_N E_R}$, of the order of MeV, so that dark matter can not resolve the internal nucleus structure. For large momentum transfer, the de Broglie wavelength decreases and part of the nucleons can participate to the interaction, modifying the cross section. This effect is encoded in the form factor. Eq. (3.109) is referred as spin-independent because does not depend on the nuclear spin. In the spin-dependent case we have:

$$\frac{d\sigma}{dE_R} = \frac{16m_N G_F^2}{\pi v^2} \Big(a_p \langle S_p \rangle + a_n \langle S_n \rangle \Big)^2 \frac{J + 1}{J} F_{SD}^2(E_R), \tag{3.110}$$

where G_F is the Fermi constant, a_p, a_n are the effective WIMP-nucleon couplings, $\langle S_p \rangle$, $\langle S_n \rangle$ are the average spin contributions of the nucleon. It is important to point out that the nuclear form factor is different from the spin-independent case.

There are several experiments for direct searches of dark matter, for example XENON1T [95], LUX [96], DarkSide-50 [97], PandaX-II [98] and SuperCDMS [99]. It is important to notice that they work with different nuclei, XENON1T, LUX and PandaX-II work with Xe, DarkSide-50 works with Ar, while SuperCDMS works with Ge, so, in order to compare the results, we need to cast eq. (3.109) in another form. We can factor out the dependence on the target nucleus:

$$\frac{d\sigma}{dE_R} = \frac{2m_N}{4\mu_N^2 v^2} \sigma_{SI} F_{SI}^2(E_R) \tag{3.111}$$
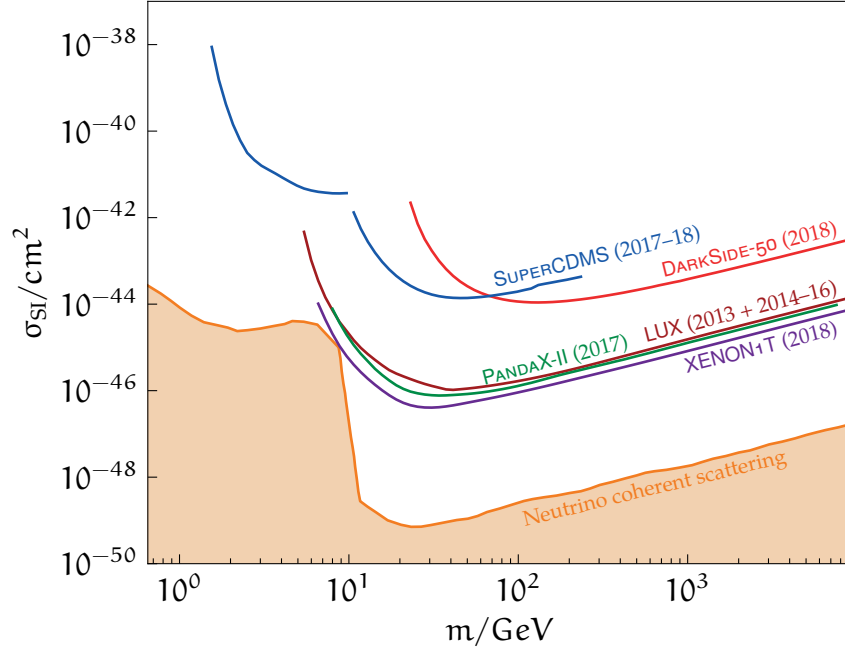
Figure 3.8: Summary of the current 90% CL upper limits for the spin-independent WIMP-nucleon cross section. We have considered the experiments XENON1T [100], LUX [101, 102], PandaX-II [103], DarkSide-50 [104] and SuperCDMS [105, 106]. The shaded region denotes the values of the cross section sensitive to the coherent neutrino scattering off nuclei [107].

and considering the spin-independent cross section σ_{SI}

$$\sigma_{SI} = \frac{\mu_N^2}{\mu_p^2} A^2 \sigma_p \, , \tag{3.112}$$

where we have assumed $f_n = f_p$, so that dark matter couples coherently to the entire nucleus and the cross section increases with the number of nucleons. It depends on the WIMP-nucleon cross section σ_p and on the reduced mass of WIMP-nucleon system μ_p. The more recent results of the mentioned experiments are shown in fig. 3.8, as 90% CL upper limits on the spin-independent WIMP-nucleon cross section for different values of the WIMP mass.

3.11 Collider searches

The search for dark matter through colliders is based on the assumption that it can interact with Standard Model particles: this can happen directly with couplings to colliding quarks or leptons, or indirectly with a mediator. Therefore, dark matter can in principle be produced by Standard Model particles collision. This is the aim of collider searches. From the point of view of detection, dark matter particles are similar to neutrinos, being without any electromagnetic or

colour charge. If dark matter is the lightest and stable particle of new states, the collider signature would be a cascade decays of the heavier new states, eventually producing multi-parton or multi-lepton final states, together with missing energy. One of the advantages of colliders is that they are equipped with multipurpose detectors with which we can measure a lot of observables and reconstruct the kinematic of the dark matter production process. A second important feature is the high luminosity of colliders. The luminosity is a key parameter in collider experiments, expressing the rate of the events per seconds, having high luminosity means a huge amount of data, that can potentially contain a lot of dark matter-related events. Last, background processes can be studied in detail with the help of simulations. The combination of these three features makes colliders a promising methods for dark matter searches. That being said, if we discover a new particle with dark matter properties through colliders, we will in addition learn a lot of properties of that particle. Nonetheless, the detection of dark matter signature is quite challenging and revealing a particle that does not decay in the detector volume does not mean it is stable on cosmological time, that is the first requirement we need for dark matter in order to explain the relic density.

There are two kinds of colliders: electron colliders and hadron colliders.

Electron colliders

In an electron collider the colliding particles are e^+, e^-. In a lepton collider we know exactly the initial state, so we can reconstruct the four-momenta of final particles starting from the initial ones. Production of dark matter can happen in different ways, the simplest is the pair production. If we want to obtain two dark matter particles χ of mass m_χ then we need a centre-of-mass energy $\sqrt{s} \geqslant 2m_\chi$. This kind of signal is hard to identify, because it is invisible to our detector. Another possibility is to look for dark matter production along with another particle, such as a photon. This process can happen if the photon is radiated off one of the incoming electrons, and it is called initial state radiation. The experimental signature is often referred as γ *plus missing momentum*. In spite of being characterised by a clean environment, electron colliders can not reach high centre-of-mass energy in their collision. Moreover, that kind of process requires the production of an hard photon and this lowers the rates of significant events.

Hadron colliders

Hadron colliders are instead characterised by high centre-of-mass energies, however the experimental environment is far more complicated, there is a lot of background related to the QCD processes and computations are less precise. In colliders we consider two kinds of processes: signal and background. We are interested in the signal, so we need to isolate the background, that is made of known processes and is described by QCD. Moreover we have to isolate interesting data, so we need to set up a trigger that evaluates whether an event is relevant for

our dark matter research. The drawback of hadron collider is the impossibility to exactly determine the initial state. With the Large Hadron Collider (LHC) [108] at CERN we are able to make protons beams collide with energy $7\,TeV$ each; at these high energies we can resolve the internal structure of protons, so we need to describe the initial state on the basis of quarks and gluons. Consequently, the actual energy of the collision is at the TeV scale. Moreover we can not predict the energy distribution of quarks and gluons, because it depends on the Parton Distribution Functions [109], that can be determined only through experiments. We can not reconstruct the four-momenta of the dark matter particles emerging from the collision, but we can analyse the transverse momentum, that is supposed to be zero both for initial and final state. The transverse momentum of a certain particle i is defined as:

$$\mathbf{p}_{T,i} \doteq \mathbf{p}_i \sin\vartheta\,, \tag{3.113}$$

where ϑ is the outgoing angle of the particle. Because we can not detect dark matter particle directly, this will lead to an unbalanced of the total transverse momentum. We can define a new observables, the missing transverse momentum $\mathbf{p}_T^{miss}$, given by:

$$\mathbf{p}_T^{miss} \doteq -\sum_i \mathbf{p}_{T,i}\,. \tag{3.114}$$

A missing transverse momentum different from zero is a potential signature for an invisible particle. We define another quantity, the missing transverse energy as $E_T^{miss} \doteq |\mathbf{p}_T^{miss}|$. The measurement of E_T^{miss} relies on a precise measurement of the entire recoil. This is characterised by several experimental problems: particles hitting the structure of the detectors, wrong reconstruction of jet events or non functional parts of the detectors can lead to a fake missing energy. However, it is possible to keep into account these effects by making cuts on the missing energy value.

A recent result accomplished by CMS is the search for invisible decays of Higgs boson [110], that allows to place an upper limit on the branching ratio of Higgs boson to invisible particles:

$$\mathcal{B}(h \to inv.) < 0.33 \text{ at } 95\% \text{ CL.} \tag{3.115}$$

If dark matter couples to the Higgs boson, we can suppose that those invisible particles are indeed dark matter particles and exploit this result in order to constrain the parameter space of dark matter models.

Chapter 4

Automation of loop-induced amplitude computations

In chap. 3 we have seen that the γ-ray line signature arises from annihilation of dark matter into a pair of photons. Because dark matter is supposed to be electrically neutral, this process can proceed only via a loop, even at Leading Order (LO), and does not have any tree-level contribution. Processes like this are called loop-induced processes. Their calculation will involve loop integrals, that in this case are unavoidable, and can be computed using numerical techniques. In this chapter we describe the numerical tool MADGRAPH5_AMC@NLO [5, 6] focusing on the main techniques it uses to handle loop-induced computations. A complete treatment of the topic can be found in [6], while here we are interested in giving an outline of what operations are done, which external softwares are used and how they work together to produce the final result.

4.1 Construction of the matrix element

Considering a $2 \to n$ process, MADGRAPH5_AMC@NLO computes the following quantity:

$$\mathrm{d}\sigma \propto \overline{\sum_{\substack{\text{spin} \\ \text{colour}}} |\mathcal{A}|^2}, \tag{4.1}$$

where we can express the square amplitude as:

$$|\mathcal{A}|^2 = \left|\mathcal{A}^{(n,0)} + \mathcal{A}^{(n,1)}\right|^2 = \left|\mathcal{A}^{(n,0)}\right|^2 + \left|\mathcal{A}^{(n,1)}\right|^2 + 2\mathcal{R}e\left\{\mathcal{A}^{(n,0)}\mathcal{A}^{(n,1)*}\right\}, \tag{4.2}$$

where the term $\mathcal{A}^{(n,\ell)}$ means the amplitude of a process $2 \to n$ characterized by the presence of ℓ loops. The term $\left|\mathcal{A}^{(n,0)}\right|^2$ is the tree-level (called also Born level) amplitude, in the case of loop-induced processes this is null. We are left with the term $\left|\mathcal{A}^{(n,1)}\right|^2$ alone. The computation of this amplitude is done by a dedicated module of MADGRAPH5_AMC@NLO, called MADLOOP. The amplitude $\mathcal{A}^{(n,1)}$ can be expressed as a sum over the contribution $\mathcal{C}$ given by the different Feynman

diagrams that participate to the process:

$$\mathcal{A}^{(n,1)} = \sum_{\text{diagrams}} \mathcal{C}. \tag{4.3}$$

There are different numerical technique available to handle this computation. The first implementation of MadLoop, that we will call MadLoop4 [111], was based on the Ossola, Papadopoulos, Pittau (OPP) technique [112]. Its update in MadGraph5_aMC@NLO, called MadLoop5, uses the Tensor Integral Reduction (TIR) technique [113, 114], first introduced by Passarino and Veltman. Both allow to reduce the master loop integrals as a linear combination of simpler integrals, called scalar integrals plus a rational term, that we will call R. Consequently, $\mathcal{C}$ is cast as:

$$\mathcal{C} = \text{Red}[\mathcal{C}] = \sum_i d_i(\mathcal{C}) \left(\begin{array}{c}\boxed{}\end{array}\right)_i + \sum_i c_i(\mathcal{C}) \left(\begin{array}{c}\triangleleft\end{array}\right)_i$$

$$+ \sum_i b_i(\mathcal{C}) \left(\begin{array}{c}\bigcirc\end{array}\right)_i + \sum_i a_i(\mathcal{C}) \left(\begin{array}{c}\bigcirc\end{array}\right)_i + R(\mathcal{C}), \tag{4.4}$$

where each diagram (in order: box, triangle, bubble, tadpole) shown is a one-loop (scalar) integral independent of $\mathcal{C}$. The scalar integrals are defined as follows, using the conventions of 't Hooft and Veltman [115], in d dimensions:

$$\bigcirc \doteq A_0(m) = \frac{(2\pi\mu)^{4-d}}{i\pi^2} \int d^d q \, \frac{1}{q^2 - m^2}, \tag{4.5}$$

$$\bigcirc \doteq B_0(p, m_1, m_2) = \frac{(2\pi\mu)^{4-d}}{i\pi^2} \int d^d q \, \frac{1}{[q^2 - m_1^2][(q+p)^2 - m_2^2]}, \tag{4.6}$$

$$\triangleleft \doteq C_0(p_1, p_2, m_1, m_2, m_3) = \frac{(2\pi\mu)^{4-d}}{i\pi^2}$$

$$\times \int d^d q \, \frac{1}{[q^2 - m_1^2][(q+p_1)^2 - m_2^2][(q+p_1+p_2)^2 - m_3^2]}, \tag{4.7}$$

$$\boxed{} \doteq D_0(p_1, p_2, p_3, m_1, m_2, m_3, m_4) = \frac{(2\pi\mu)^{4-d}}{i\pi^2}$$

$$\times \int d^d q \, \frac{1}{\begin{array}{c}[q^2 - m_1^2][(q+p_1)^2 - m_2^2] \\ \cdot [(q+p_1+p_2)^2 - m_3^2][(q+p_1+p_2+p_3)^2 - m_4^2]\end{array}}, \tag{4.8}$$

where we have dropped the $i\varepsilon$ prescription and added a normalisation constant with the dimension of mass. The main difference between these techniques is in the algebraic method employed to compute the coefficients and R. MadLoop5 (from now on we will call it simply MadLoop) is implemented with both the techniques and can switch between them.

The next step is to cast the expression of the one-loop amplitude in d dimension, where $d = 4 - 2\varepsilon$, with $\varepsilon \to 0$, to recover 4 dimensions. We can express $\mathcal{C}$ as

$$\mathcal{C} = \int d^d \bar{l}\, \bar{C}(\bar{l})\,, \tag{4.9}$$

with

$$\bar{C}(\bar{l}) = \frac{\bar{N}(\bar{l})}{\prod_{i=1}^{k} \bar{D}_i}\,, \tag{4.10}$$

where we have assumed that the loop is made of k propagators and

$$\bar{D}_i = (\bar{l} + p_i)^2 - m_i{}^2 \tag{4.11}$$

is the inverse of the ith propagator, related to a particle with mass m_i and momentum p_i. In d dimensions we can make the decomposition of the loop momentum $\bar{l}$ in:

$$\bar{l} = l + \tilde{l}\,, \tag{4.12}$$

where l is the 4-dimensional part, while $\tilde{l}$ is the (-2ε)-dimensional one. Clearly we have:

$$l \cdot \tilde{l} = 0\,. \tag{4.13}$$

A similar relation holds also for Dirac matrices $\bar{\gamma}^\mu$ and for the metric tensor $\bar{g}^{\mu\nu}$. Therefore it is possible to define the 4-dimensional part of the numerator in eq. (4.10):

$$N(l) = \lim_{\varepsilon \to 0} \bar{N}(\bar{l} = l;\, \bar{\gamma}^\mu = \gamma^\mu,\, \bar{g}^{\mu\nu} = g^{\mu\nu})\,, \tag{4.14}$$

and consequently express the (-2ε)-dimensional part as:

$$\tilde{N}(l, \tilde{l}) = \bar{N}(\bar{l}) - N(l)\,. \tag{4.15}$$

The new quantity in eq. (4.14) is a 4-dimensional quantity and can be treated numerically without any issues. That means we can express $\mathcal{C}$ as

$$\mathcal{C} = \mathcal{C}_{\text{non-R}_2} + R_2\,, \tag{4.16}$$

where we have defined

$$\mathcal{C}_{\text{non-R}_2} = \int d^d \bar{l}\, \frac{N(l)}{\prod_{i=1}^{k} \bar{D}_i}\,, \tag{4.17}$$

$$R_2 = \int d^d \bar{l}\, \frac{\tilde{N}(l, \tilde{l})}{\prod_{i=1}^{k} \bar{D}_i}\,. \tag{4.18}$$

We see that they still depend on a $(4-2\varepsilon)$-dimensional quantity, but the numerator is a 4-dimensional function. We can obtain a representation of the amplitude in eq. (4.3) separating the contribution coming from non-R_2 and R_2 terms, recalling eq. (4.16):

$$\left|\mathcal{A}^{(n,1)}\right|^2 = \left|\mathcal{A}_{\text{non-R}_2}^{\text{LI}}\right|^2 + \left|\mathcal{A}_{\text{R}_2}^{\text{LI}}\right|^2 + 2\mathcal{R}e\left\{\mathcal{A}_{\text{non-R}_2}^{\text{LI}} \mathcal{A}_{\text{R}_2}^{\text{LI}\,*}\right\}\,. \tag{4.19}$$

It is important to remark that loop-induced processes are finite, they are not characterised by any divergences. Given that there are no tree-level vertices, it is indeed not possible to obtain counterterms with which cancel the eventual divergences. That means the only external ingredients we need to provide are the R_2 terms. They are defined as the integral in eq. (4.18); it can be shown [116] that the result is a set of a process-independent Feynman rules. That means they can be computed once and only once for each model. So, the R_2 terms are theory-dependent parts, to be added to the definition files of the model, before importing it in MADLOOP. Their computation can be done in an automatised way, using three MATHEMATICA packages: FEYNRULES [21], FEYNARTS [22] and NLOCT [23]. What we obtain at the end is the Unified FEYNRULES Output (UFO) [117] format of the model, that is a set of Python files that can be imported in MADGRAPH5_aMC@NLO.

The amplitude $\left|\mathcal{A}_{\text{non-R}_2}^{\text{LI}}\right|^2$ is the element specific to the loop-induced computation. It can be written as:

$$\sum_{\text{colours}} \left|\mathcal{A}_{\text{non-R}_2}^{\text{LI}}\right|^2 = \sum_{\text{colours}} \sum_{h=1}^{H} \left(\sum_{l_1=1}^{L} \lambda_{l_1} \int d^d \bar{q} \, \frac{N_{h,l_1}(q)}{\prod_{i=1}^{k_{l_1}} \bar{D}_{i,l_1}} \right)$$
$$\times \left(\sum_{l_2=1}^{L} \lambda_{l_2} \int d^d \bar{q} \, \frac{N_{h,l_2}(q)}{\prod_{i=1}^{k_{l_2}} \bar{D}_{i,l_2}} \right)^*, \quad (4.20)$$

where λ_{l_i} are the colour structures. The indexes h and l_i label the helicity state and the subamplitude, they are summed over their total numbers H and L. The integer n_{l_i} denotes the number of loop propagators in the subamplitude l_i. The integrals can be reduced using one of the mentioned OPP or TIR techniques. However, if we consider the reduction (formally indicated by the operator Red[·]) we find the expression

$$\sum_{\text{colours}} \left|\mathcal{A}_{\text{non-R}_2}^{\text{LI}}\right|^2 = \sum_{h=1}^{H} \sum_{l_1=1}^{L} \sum_{l_2=1}^{L} \left(\text{Red}\left[\frac{N_{h,l_1}}{\prod_{i=1}^{k_{l_1}} \bar{D}_{i,l_1}} \right] \text{Red}\left[\frac{N_{h,l_2}(q)}{\prod_{i=1}^{k_{l_2}} \bar{D}_{i,l_2}} \right]^* \sum_{\text{colours}} \lambda_{l_1} \lambda_{l_2}^* \right).$$
$$(4.21)$$

We notice that the loop amplitudes interfere each other. The sum depends on L^2 terms, so it has a quadratic dependence on the number of different diagrams. The technique that is used to reduce the integral is important to reduce the computational time and MADLOOP can switch between the two mentioned techniques in order to choose the best one. For further details on the numerical computation of this amplitude, see [9].

4.2 Computation of the R_2 terms

The software FEYNRULES, FEYNARTS and NLOCT allow to compute the R_2 terms for each model, and export the model in the UFO format in order to be used by MADGRAPH5_aMC@NLO. In general, they are also able to compute the

UV counterterms (that are theory-dependent, too) in order to produce a model that can be used also for Next-to-Leading Order (NLO) computations. In this case we focus only on the computation of the R$_2$ terms, summarising the main steps.

After implementing the model in FEYNRULES and write the lagrangian, we can perform its renormalisation with FEYNRULES itself. The renormalised lagrangian is then passed to FEYNARTS, that expresses the various vertices in the following form:

$$\text{vertices} = \sum_i c_i L_i, \tag{4.22}$$

where the ith vertex is characterized by the coupling c_i and the Lorentz structure L_i. The latter contains all the kinematical information, such as Dirac matrices, metric tensors, momenta, Levi-Civita tensors. Consequently, we can call NLOCT that is able to solve the renormalisation conditions and compute the UV counterterms and the R$_2$ terms. The computation of those terms requires that the model is renormalisable and is written in the Feynman's gauge (as also MADLOOP works with it). The computation starts with the generation of the one-loop amplitudes for a given number of external scalar, fermion and vector fields. So now we compute the R$_2$ terms, following eq. (4.18). First we make use of the Feynman parameters to express the integral numerator and denominator. Then we can substitute the products of the loop momenta with:

$$p^\mu p^\nu p^\rho p^\sigma \to p^4 \frac{1}{d(d+2)} (g^{\mu\nu} g^{\rho\sigma} + g^{\mu\rho} g^{\nu\sigma} + g^{\mu\sigma} g^{\rho\nu}), \tag{4.23a}$$

$$p^\mu p^\nu \to p^2 \frac{1}{d} g^{\mu\nu}. \tag{4.23b}$$

Carrying out the loop-integration of the R$_2$ terms we obtain:

$$\int d^d p \, \frac{\varepsilon}{p^2 - m^2} \quad = i\pi^2 m^2, \tag{4.24a}$$

$$\int d^d p \, \frac{\varepsilon}{(p^2 - \Delta)^2} \quad = i\pi^2, \tag{4.24b}$$

$$\int d^d p \, \frac{p^2(a\varepsilon + b)}{(p^2 - \Delta)^2} = i\pi^2 (2a - b)\Delta, \tag{4.24c}$$

$$\int d^d p \, \frac{p^2(a\varepsilon + b)}{(p^2 - \Delta)^3} = i\pi^2 \left(a - \frac{1}{2}b\right), \tag{4.24d}$$

$$\int d^d p \, \frac{p^4(a\varepsilon + b)}{(p^2 - \Delta)^4} = i\pi^2 \left(a - \frac{5}{6}b\right), \tag{4.24e}$$

where a and b are polynomials on the Feynman parameters.

The lists of the R$_2$ terms and of the UV counterterms are written on an external file by NLOCT. That file must be imported in FEYNRULES, in order to obtain the NLO UFO format of the model. The resulting UFO format will contain all the computed terms and it is ready to be used in MADGRAPH5_AMC@NLO to analyse loop-induced processes. The new vertices inferred by the R$_2$ terms allow

to compute the amplitude $\mathcal{A}_{R_2}^{LI}$ that appears in eq. (4.19). That is a tree-level amplitude, that can be handled easily by MadGraph5_aMC@NLO.

Chapter 5

MᴀᴅDM applications to dark matter models

In §§ 3.9–3.11 we have seen different experimental approaches in order to study dark matter. There is a widespread belief that it could be made of new particles, which belong to the so called dark sector. For this reason, plenty of theoretical dark matter models are now available, with different mass scales, number of particles or interaction strength. In order to study these models efficiently, determine if they are compatible with experimental constraints and obtain important predictions, the key ingredient is the possibility to compute the relevant quantities related to each one. However, a pure analytical treatment is impractical: models become more and more complicated and, in order to investigate the entire parameter space, we need eventually to solve the Boltzmann equation, whose analytical solutions are approximated. The best approach is to use a numerical tool, that must be able to compute all interesting physical quantities and eventually contain all the experimental results that are available now.

In this thesis we focus on the numerical tool MᴀᴅDM [4], giving an outline of its capabilities in this chapter. We will then discuss the possibility to compute loop-induced processes with it. The aim of this thesis is, in fact, to validate this feature in MᴀᴅDM with two dark matter models. From an experimental point of view, loop-induced processes are related to the annihilation of dark matter in a pair of photons, that is an important process in the framework of indirect detection, because it gives a characteristic monochromatic signature.

As we mentioned, many dark matter models are available today: we have decided to focus on WIMP models. In order to build a valid model, the first thing we need to do is to make assumptions on quantum numbers related to our dark matter candidate. We assume the existence of only one stable particle, to generate the entire dark matter density of the Universe. Its mass is assumed to be in the range from GeV to TeV, while its density comes from the thermal production during the cooling of the Universe. Postulate a new particle is not enough to study dark matter properties. From the freeze-out mechanism, we know that dark matter has to couple with Standard Model. So we need to postulate also a

way for our candidate to communicate with it. This means we need a mediator, his choice depends on the model. This approach is known as simplified models. The idea behind a simplified model is to enrich the known Standard Model framework by adding just the particles describing the dark matter sector and a mediator. It is someway similar to an Effective Field Theory (EFT) approach. In EFT one studies a low energy model, characterised by the presence of high dimension operators. They comes from particles that emerges only at high energy, so that one can integrate them out at low energy. In this case, we incorporate new particles (dark matter and the mediator) in the Standard Model, that is treated as an EFT description of a more general model containing those new particles. The dark matter models we will study in this thesis are: the singlet scalar Higgs portal model and a simplified top-philic model. Both of them are simple extension of the Standard Model. The first one has a new real scalar field that couples with Higgs boson, that is the mediator. The second one has a fermionic dark matter candidate, that couples to the Standard Model through a coloured scalar. Both the models will be implemented in a UFO format at an NLO level, because we need to deal with loop-induced processes, as explained in chap. 4. We will study the loop-induced annihilation in photons, comparing the numerical results coming from MADDM with analytical results. Moreover we will study the phenomenology of the models, analysisng their parameter space and implementing the various constraints on indirect detection, direct detection and collider searches. In particular, we will exploit the constraints on the γ-ray line signature coming from FERMI-LAT [19] and HESS [20].

5.1   What is MADDM?

MADDM is a numerical tool able to compute the most relevant quantities related to dark matter for any dark matter model in UFO format. Its first release [118] provided the possibility to compute the relic density for a certain dark matter model. The second release [119] added the computation of dark matter-nucleon cross section along with the double differential event rates of nuclear recoils for a generic experiment. Moreover, it implements the LUX experimental likelihoods [120] to compare with data. The last version implements the indirect detection module, which allows to perform the computation of the main observables relative to indirect detection. It is now possible to predict the fluxes of γ-rays, neutrinos or cosmic rays coming from dark matter annihilation in the Milky Way or in neighbour galaxies. Moreover, in this version, MADDM is a plugin of MADGRAPH5_AMC@NLO, and can inherit its capabilities. The computation of $\langle \sigma v \rangle$ can be performed at tree-level for different final states in two ways: either with the approximation of fixed dark matter velocity, or by generating events according to a Maxwell-Boltzmann velocity distribution for the dark matter in the galactic halo. In the last case, the annihilation is performed with a centre-of-mass energy of $\sqrt{s} = 2m_\chi \left(1 + v_{\text{rel}}^2/8\right)$, with m_χ being dark matter mass and $v_{\text{rel}} = \sqrt{3}v_0$ (see § 3.9). Another new feature in MADDM is the experiment module: it allows

to test model points against direct and indirect experimental constraints. The current version of MADDM considers the following limits for direct detection: XENON1T [121] and LUX [102] for spin-independent cross section; LUX [122] and Pico60 [123] for spin-dependent cross section respectively on neutron and proton. For what concerns the indirect detection, MADDM has implemented the FERMI-LAT likelihood for prompt γ-rays coming from the analysis of dwarf spheroidal galaxies [124, 125]. Further details on the capabilities of MADDM can be found in [4].

At the current version, MADDM can compute annihilation cross sections for any tree-level process. In this thesis we will focus on loop-induced processes, in particular on indirect detection into two photons, studying the γ-ray line signature. The capability of performing loop-induced computation should be inherited by MADGRAPH5_AMC@NLO (see chap. 4) and we will validate it with two dark matter models. Moreover, this feature will allow to study other processes such as annihilation in γZ or γh, that, together with $\gamma\gamma$, are called the *smoking guns* signatures of dark matter.

5.2   Singlet scalar Higgs portal model

The singlet scalar Higgs portal model [10–12, 30] is one of the simplest extension of Standard Model which can explain dark matter. It consists of the addition of a new scalar field S, which is a singlet for all of the Standard Model gauge groups. The new interactions are renormalisable. To be a valid dark matter candidate, the particle must be stable. We can satisfy this request by assuming a $\mathbb{Z}_2$ symmetry, under which S is odd, $S \to -S$, while the Standard Model is even.

The lagrangian of the model reads:

$$\mathcal{L} = \mathcal{L}_{\text{SM}} + \frac{1}{2}\partial_\mu S \partial^\mu S - \frac{1}{2}m_{S0}^2 S^2 - \frac{1}{4}\lambda_S S^4 - \frac{1}{2}\lambda_{hS}\varphi^\dagger\varphi S^2 \,, \tag{5.1}$$

where m_{S0} is the mass of the field S before electroweak symmetry breaking and λ_S is the quartic coupling of S. The field φ is the usual Higgs Standard Model doublet, that after the electroweak symmetry breaking and in the unitary gauge has the form:

$$\varphi = \frac{1}{\sqrt{2}}\begin{pmatrix} 0 \\ v+h \end{pmatrix}, \tag{5.2}$$

with h being the Higgs boson and $v = 246\,\text{GeV}$ the vacuum expectation value. We see that the coupling λ_{hS} is the coupling between dark matter and the Standard Model: h works as the mediator. After the electroweak symmetry breaking we can write the following lagrangian:

$$\mathcal{L} = \mathcal{L}_{\text{SM}} + \frac{1}{2}\partial_\mu S \partial^\mu S - \frac{1}{2}m_S^2 S^2 - \frac{1}{4}\lambda_S S^4 - \frac{1}{2}\lambda_{hS}vhS^2 - \frac{1}{4}\lambda_{hS}h^2 S^2 \,, \tag{5.3}$$

where we have defined $m_S^2 = m_{S0}^2 + \lambda_{hS}\frac{v^2}{2}$.

Looking at eq. (5.1) we have three parameters to describe the model: two of them (m_{S0}^2 and λ_S) are related to S sector, while the last one (λ_{hS}) regards the interaction of S with the mediator. We can study more deeply the parameter space, in order to find the constraints on the couplings, discussing the vacuum stability and the symmetry breaking pattern. Considering the entire scalar potential from eq. (5.1) we have:

$$V = \frac{1}{2}m_{S0}^2 S^2 + \frac{1}{4}\lambda_S S^4 + \frac{1}{2}\lambda_{hS}\,\varphi^\dagger\varphi S^2 - \mu_h{}^2\varphi^\dagger\varphi + \lambda_h\left(\varphi^\dagger\varphi\right)^2, \qquad (5.4)$$

where the last two terms come from the Higgs lagrangian of the Standard Model. We can discuss the following properties [11]:

- vacuum stability: the scalar potential is bounded from below if the couplings obey the relations

$$\lambda_S, \lambda_h \geqslant 0, \qquad (5.5a)$$
$$\lambda_S\lambda_h \geqslant \lambda_{hS}^2 \quad \text{if } \lambda_{hS} < 0; \qquad (5.5b)$$

- correct symmetry breaking pattern: S does not take a vacuum expectation value: $\langle 0|S|0\rangle = 0$, by the means of the $\mathbb{Z}_2$ symmetry imposed on it. That means we are working with a dark real scalar. This prevents S from affecting the electroweak Symmetry breaking, by mixing with φ, therefore $m_{S0}^2 > 0$.

Our model can be exploited to study dark matter properties. As we saw, the value of the parameter λ_S is important to guarantee the vacuum stability, but for our purposes is highly unconstrained and can be chosen arbitrarily, though it must not be too high in order to guarantee also perturbativity, as can be seen in [126]. So we are left with only two parameters, one related to the mass of our WIMP candidate and the other related to the coupling with the Higgs boson. In the lagrangian in eq. (5.1), we notice the presence of the operator $\varphi^\dagger\varphi$: it is the only one in the Standard Model with dimension two and so can be used to study a lot of phenomena: invisible decay width of the Higgs boson, the annihilation of dark matter through Higgs channels and the interaction $SS \rightarrow hh$. We can study the model deeply by computing some relevant quantities related to dark matter and see if we can reproduce the experimental results by assuming some values for the parameters. In fig. 5.1 we see the annihilation diagrams related to the model: in particular fig. 5.1a is relative to the annihilation in Standard Model particles by a $2 \rightarrow 2$ process at tree-level. Let us focus on a light dark matter scalar and let's consider the leading decay of Higgs boson in $b\bar{b}$ ($\mathcal{B}(h \rightarrow b\bar{b}) \approx 60\%$):

$$SS \rightarrow h \rightarrow b\bar{b}, \qquad (5.6)$$

where Higgs boson is eventually off shell. Its diagram is shown in fig. 5.2. We can write the amplitude for the process:

$$\mathcal{A}(k_1, k_2) = \bar{u}(k_1)\frac{-im_b}{v}v(k_2)\frac{i}{(k_1 + k_2)^2 - m_h^2 + im_h\Gamma_h}(-i\lambda_{hS}v), \qquad (5.7)$$
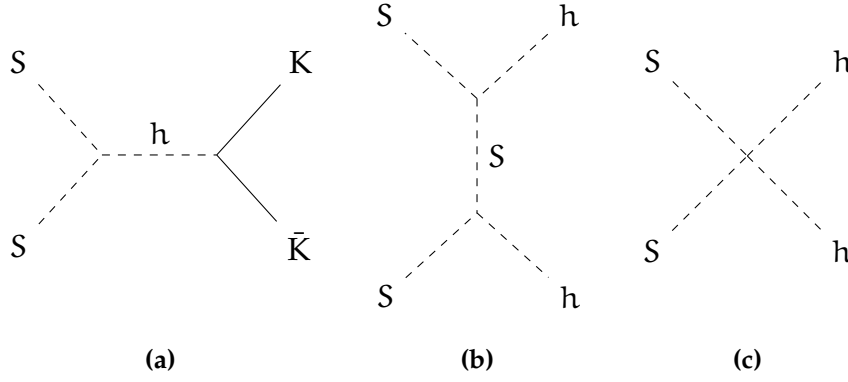
Figure 5.1: Leading order $2 \to 2$ annihilation diagrams for the singlet scalar Higgs portal model, K is a generic Standard Model particle.
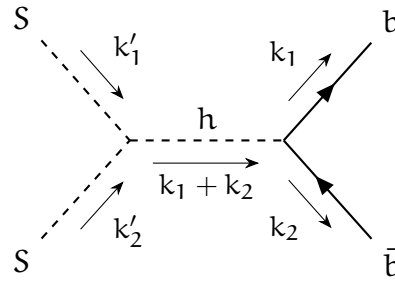
Figure 5.2: Annihilation diagram of dark matter in b, $\bar{b}$.

where $\bar{u}(k)$, $v(k)$ are the spin states of the final fermions and $\Gamma_h \approx 4.07\,\text{MeV}$ is the Higgs's width [127]. Notice that we have multiplied everything by 2, because S is a boson, so we can exchange the initial particles without changing the diagram: this produces the factor 2 that simplifies with the symmetry factor of the vertex coupling. Now we need to square the matrix element, sum over the spin polarisations and the colours, and take the average:

$$\overline{\sum_{\substack{\text{spin} \\ \text{colour}}} |\mathcal{A}(k_1, k_2)|^2} = 2 N_C \lambda_{hS}^2 m_b^2 \frac{s - 4 m_b^2}{(s - m_h^2)^2 + m_h^2 \Gamma_h^2} , \tag{5.8}$$

where we have defined the centre-of-mass energy $s = (k_1 + k_2)^2 = (k_1' + k_2')^2$. We can now compute the total cross section, using the formula for quasi-elastic scattering:

$$\sigma = \frac{\overline{\sum |\mathcal{A}|^2}}{16 \pi s} \sqrt{\frac{s - 4 m_b^2}{s - 4 m_S^2}} = \frac{N_C}{8 \pi \sqrt{s}} \lambda_{hS}^2 m_b^2 \sqrt{\frac{1 - \frac{4 m_b^2}{s}}{s - 4 m_S^2}} \frac{s - 4 m_b^2}{(s - m_h^2)^2 + m_h^2 \Gamma_h^2} . \tag{5.9}$$

To compute the velocity-averaged cross section today we consider the non-relativistic limit: from eq. (3.56), we obtain $s \approx 4 m_S^2$. Moreover, considering the

approximation $\langle \sigma v \rangle = \sigma v + \mathcal{O}(v^2)$ and assuming $m_S \gg m_b$ we can finally write:

$$\langle \sigma v \rangle \Big|_{SS \to b\bar{b}} \approx \frac{N_C \lambda_{hS}^2 m_b^2}{4\pi} \frac{1}{(4m_S^2 - m_h^2)^2 + m_h^2 \Gamma_h^2} . \qquad (5.10)$$

We now study three different cases, related to the different values of the mass of our candidate with respect to Higgs mass and extract the value of λ_{hS} needed to reproduce the correct value of the relic density in eq. (3.49):

- resonance: we study the case $m_S = m_h/2$, we have:

$$\langle \sigma v \rangle \Big|_{SS \to b\bar{b}} = \frac{N_C \lambda_{hS}^2 m_b^2}{4\pi m_h^2 \Gamma_h^2} \implies \langle \sigma_{XX} v \rangle = \frac{1}{\mathcal{B}(h \to b\bar{b})} \langle \sigma v \rangle \Big|_{SS \to b\bar{b}} \approx \frac{27 \lambda_{hS}^2}{\text{GeV}^2}, \qquad (5.11)$$

  from which we obtain:

$$\langle \sigma v \rangle \approx \frac{1.7 \times 10^{-9}}{\text{GeV}^2} \Leftrightarrow \lambda_{hS} \approx 8 \times 10^{-6} ; \qquad (5.12)$$

- lighter scalar: the denominator in eq. (5.10) is characterised by two terms, we see that the second one $m_h^2 \Gamma_h^2$ is negligible unless the first $(4m_S^2 - m_h^2)^2$ one is null, that means only in resonance condition. So we consider the case $m_h \gg m_S \gg m_b$ and obtain:

$$\langle \sigma v \rangle \Big|_{SS \to b\bar{b}} \approx \frac{N_C \lambda_{hS}^2 m_b^2}{4\pi m_h^4} \approx \frac{\lambda_{hS}^2}{125^2 \cdot 60^2 \text{GeV}^2} \approx \frac{1.7 \times 10^{-9}}{\text{GeV}^2} \Leftrightarrow \lambda_{hS} \approx 0.31 ; \qquad (5.13)$$

- heavier scalar: there are other important annihilation channels:

$$SS \to \tau^+ \tau^-, W^+ W^-, ZZ, hh, t\bar{t} . \qquad (5.14)$$

For the final state $t\bar{t}$ we can use the previous formula, by substitution of m_b with m_t and by the approximation $m_S \gg m_h$. However, the final states in vector bosons can not be studied with the same relation. In the unitary gauge, the vector bosons have a degree of freedom given by the Goldstone boson generated by the spontaneous symmetry breaking in the Higgs doublet φ. The final states in $W^+ W^-$ or in ZZ present that degree of freedom. In order to estimate the result, we can consider a final state with a similar degree of freedom, for example the Higgs pairs, as the Higgs boson comes from the same doublet. The annihilation $SS \to hh$ is given by the three diagrams in fig. 5.1, respectively a s, t-channel and a 4-vertex interaction. The amplitudes of the s-channel and the 4-vertex interaction can be written straightforwardly:

$$\mathcal{A}_4 = -i\lambda_{hS} , \qquad (5.15)$$

$$\mathcal{A}_s = (-i\lambda_{hS} v) \frac{i}{s - m_h^2} \left(-3i \frac{m_h^2}{v} \right) = -\frac{3i m_h^2 \lambda_{hS}}{s - m_h^2} . \qquad (5.16)$$
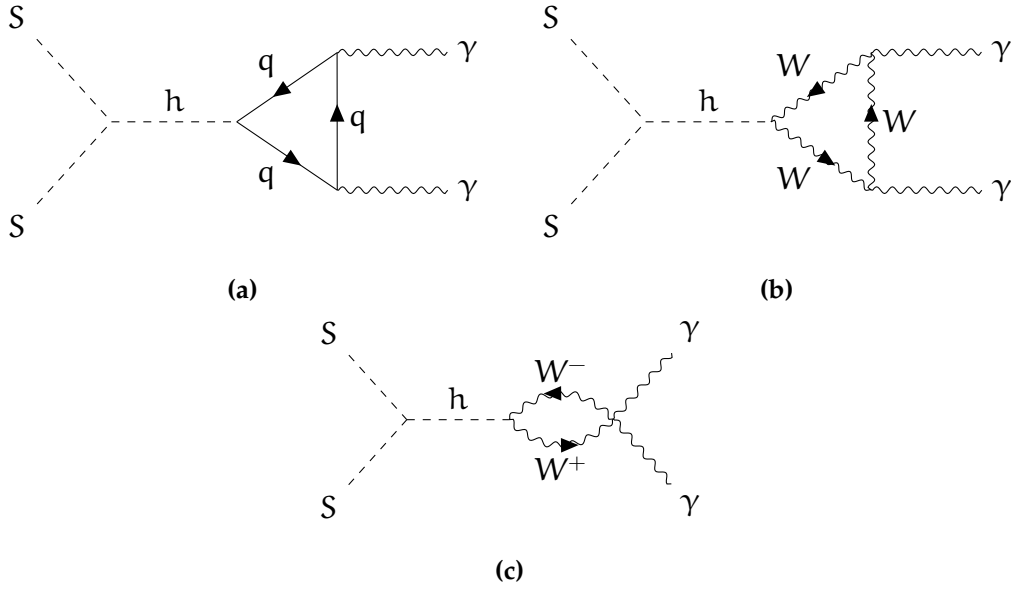
Figure 5.3: Loop-induced annihilation diagrams in photons (unitary gauge) for the singlet scalar Higgs portal model.

They are proportional to λ_{hS}, so we can neglect the t-channel, being it proportional to λ_{hS}^2. Assuming the threshold $s = 4m_S^2$ and $m_S \gg m_h$ we have:

$$\mathcal{A}_s = -\frac{3im_h^2\lambda_{hS}}{4m_S^2 - m_h^2} \ll \mathcal{A}_4 \, , \tag{5.17}$$

so that we can neglect the s-channel and consider only $\mathcal{A}_4$. Using the same arguments as in the previous cases we can obtain a formula for the cross section; assuming $m_S = 200\,GeV$:

$$\langle \sigma v \rangle \bigg|_{SS \to hh} \approx \frac{\lambda_{hS}^2}{32\pi m_S^2} \approx \frac{\lambda_{hS}^2}{4 \times 10^6\,GeV^2} \approx \frac{1.7 \times 10^{-9}}{GeV^2} \Leftrightarrow \lambda_{hS} \approx 0.08 \, . \tag{5.18}$$

We see that the right choice of the parameters allows us to reproduce the correct relic density for this model. The annihilation processes shown in fig. 5.1 results in a continuum spectrum of γ-rays, due predominantly to $\pi_0 \to \gamma\gamma$.

Loop-induced annihilation $SS \to \gamma\gamma$
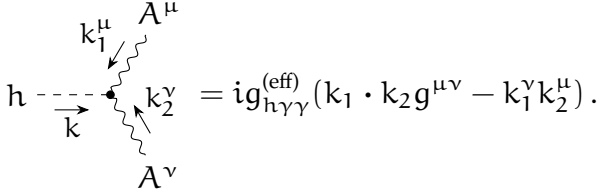
The annihilation $SS \to h \to \gamma\gamma$ is a loop-induced process, the related Feynman diagrams can be found in fig. 5.3 in the unitary gauge. The singlet scalar Higgs portal model has been implemented in UFO format with NLO corrections in order to be imported by MADDM.
We have carried out the numerical computation of this process and compared the results with an effective field theory approach, using the Higgs Effective Theory (HEFT) [14–16].

The HEFT provides a new piece of lagrangian, that contains the new interaction vertex $h\gamma\gamma$:

$$\mathcal{L}_{\text{HEFT}} = -\frac{1}{4}g^{(\text{eff})}_{h\gamma\gamma}F_{\mu\nu}F^{\mu\nu}h\,, \qquad (5.19)$$

where $F_{\mu\nu} = \partial_\mu A_\nu - \partial_\nu A_\mu$ is the field strength tensor of the electromagnetic vector field A^μ. The new Feynman rule we have to deal with is:

$$
\begin{array}{c}
A^\mu \\
k_1^\mu \\
h \cdots\bullet\; k_2^\nu \quad = ig^{(\text{eff})}_{h\gamma\gamma}(k_1 \cdot k_2 g^{\mu\nu} - k_1^\nu k_2^\mu)\,. \\
\overrightarrow{k} \\
A^\nu
\end{array}
\qquad (5.20)
$$

In order to find the expression for the $g^{(\text{eff})}_{h\gamma\gamma}$ we have to make a matching between the singlet scalar Higgs portal model and the HEFT approach. This can be done by comparing the expression for the amplitudes arising from the processes $SS \to \gamma\gamma$ in both models. The complete calculation of this process involves the three diagrams in fig. 5.3, which are loop diagrams that have the same loop structure of the diagrams relative to the decay $h \to \gamma\gamma$. In particular, we will use the results from [128]. However, in this case we have to deal with the process $SS \to \gamma\gamma$, so the amplitude will contain the coupling constant $-i\lambda_{hS}v$ and the Higgs propagator. Moreover, every occurrence of m_h^2 in the results from [128] must be substituted with s, the actual centre-of-mass energy. With these precautions, we can write the amplitude for the processes in fig. 5.3:

$$i\mathcal{A}_{\text{NLO}} = (-i\lambda_{hS}v)\frac{i}{s - m_h^2}\frac{\alpha_e}{2\pi v}F \cdot (k_1 \cdot k_2 g^{\mu\nu} - k_1^\nu k_2^\mu)\varepsilon^A_\mu(k_1)\varepsilon^B_\nu(k_2)\,, \qquad (5.21)$$

where α_e is the fine-structure constant, ε^P_μ is the polarisation vector associated to the massless vector field A_μ with P the polarisation index and

$$F = F_W\Big(\frac{4m_W^2}{s}\Big) + \sum_f N_C(f)Q_f^2 F_f\Big(\frac{4m_f^2}{s}\Big)\,, \qquad (5.22)$$

with f being any Standard Model massive particle, $N_C(f) = 3$ if f is a quark, $N_C(f) = 1$ otherwise; Q_f is the electric charge of f. The functions $F_W(x)$, $F_f(x)$ are defined as follows:

$$F_W(x) = 2 + 3x + 3x(2 - x)f(x)\,, \qquad (5.23)$$
$$F_f(x) = -2x\big[1 + (1 - x)f(x)\big]\,, \qquad (5.24)$$

where

$$f(x) = \begin{cases} \arcsin^2(\sqrt{x}) & \text{for } x \geqslant 1\,, \\ -\dfrac{1}{4}\Big[\log\Big(\dfrac{1 + \sqrt{1 - x}}{1 - \sqrt{1 - x}}\Big) - i\pi\Big]^2 & \text{for } x < 1\,. \end{cases} \qquad (5.25)$$

Now we have to write the amplitude for the HEFT approach. The process $SS \to \gamma\gamma$ is now described by a tree-level diagrams, shown in fig. 5.4. The
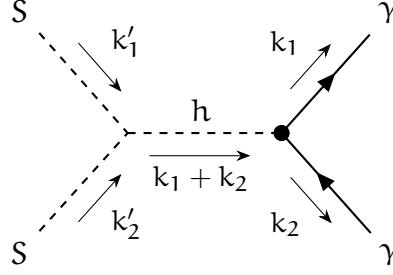
Figure 5.4: Leading order annihilation diagrams in photons for the singlet scalar Higgs portal model in HEFT.

amplitude computation is straightforward

$$i\mathcal{A}_{\text{HEFT}} = (-i\lambda_{hS}v)\frac{i}{s - m_h^2}ig_{h\gamma\gamma}^{(\text{eff})}(k_1 \cdot k_2 g^{\mu\nu} - k_1^\gamma k_2^\mu)\varepsilon_\mu^A(k_1)\varepsilon_\nu^B(k_2). \quad (5.26)$$

A comparison between eqs. (5.21) and (5.26) allows to compute:

$$g_{h\gamma\gamma}^{(\text{eff})} = \frac{\alpha_e}{2\pi v}F. \quad (5.27)$$

The HEFT approach allows us to compute the annihilation $SS \to \gamma\gamma$ as a tree-level process. These kind of processes are handled easily by MADDM, so we can use them to test the loop-induced computation. Therefore, we implemented the singlet scalar Higgs portal model with the HEFT approach in FEYNRULES, retrieving the UFO file. We have merged our model files with the ones coming from the model [129], and we have slightly modified it, by using the exact expression eq. (5.27) for $g_{h\gamma\gamma}^{(\text{eff})}$. In particular, considering every quark and lepton massless apart for b and t, we obtain:

$$g_{h\gamma\gamma}^{(\text{eff})} = \frac{\alpha_e}{2\pi v}\left[F_W\left(\frac{4m_W^2}{s}\right) + \frac{4}{3}F_f\left(\frac{4m_t^2}{s}\right) + \frac{1}{3}F_f\left(\frac{4m_b^2}{s}\right)\right]. \quad (5.28)$$

We have then chosen some values of the parameters and tested several benchmark points with MADDM, making the comparison in tab. 5.1. We see that the results are consistent, that means MADDM computes the loop-induced integrals correctly.

Phenomenology of the singlet scalar Higgs portal model

The singlet scalar Higgs portal model has only two free parameters, m_S and λ_{hS}, and the study of its phenomenology is quite simple. Our aim is to see for which values of the parameters we are able to reproduce the correct relic density measured by PLANCK [3]:

$$\Omega h^2|_{\text{PLANCK}} = 0.1200 \pm 0.0012, \quad (3.49)$$

Table 5.1: Comparison between the numerical computation made by MᴀᴅDM of the process $SS \to \gamma\gamma$ both in the general case and in HEFT approach, in the framework of the singlet scalar Higgs portal model. We have fixed $\lambda_\chi = 0.1$.

m_S/GeV		$\langle \sigma v \rangle_{\gamma\gamma}/(cm^3\,s^{-1})$
50	NLO	2.02×10^{-29}
	HEFT	2.00×10^{-29}
60	NLO	7.08×10^{-28}
	HEFT	7.03×10^{-28}
70	NLO	1.16×10^{-28}
	HEFT	1.15×10^{-28}
100	NLO	1.01×10^{-29}
	HEFT	1.01×10^{-29}
200	NLO	1.66×10^{-31}
	HEFT	1.66×10^{-31}

and to implement the main experimental results, constraining our model.

We have computed the relic density for different values of (m_S, λ_{hS}), doing a scan over the parameter space according to the following ranges:

- $m_S \in [5, 1000]\ GeV$, in logarithmic scale;

- $\lambda_{hS} \in [1 \times 10^{-4}, 1]$, in logarithmic scale;

- the Higgs's resonance region $m_S \in [62.4, 63]\ GeV$ requires an accurate sampling, where $\Delta m_S = m_S(n+1) - m_S(n) \approx 4.07\ MeV$ is equal to the Higgs's width [127].

Remember that the centre-of-mass energy is $\sqrt{s} \approx 2m_S \in [10, 2000]\ GeV$ and it is equal to the four-momentum of the Higgs boson. So, the possible processes are determined by the decay modes of the Higgs boson at different energies:

- $m_S \lesssim 50\ GeV$: final states in low mass quarks and in leptons, as shown in fig. 5.1a, where $K \in \{u, d, c, s, b, e^-, \mu^-, \tau^-\}$, mostly in $b\bar{b}$, $\tau^+\tau^-$ final states;

- $50\ GeV \lesssim m_S \lesssim m_{W,Z}$: the annihilation processes in low mass quarks and leptons become less important, there are new $2 \to 3$ processes, due to final states in WW^*, ZZ^*, where the off shell gauge bosons decay in two fermions, as shown in fig. 5.5;

- $m_{W,Z} \lesssim m_S < m_h$: the annihilations processes are in W^+W^-, ZZ, with a low contribution of $b\bar{b}$;
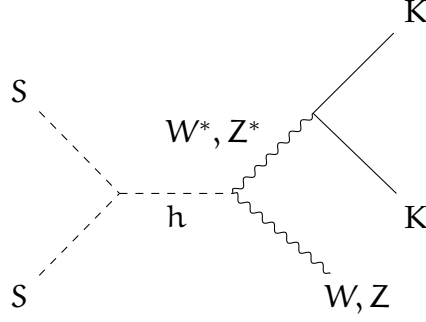
Figure 5.5: The $2 \to 3$ annihilation processes arising when $50\,\mathrm{GeV} \lesssim m_S \lesssim m_{W,Z}$. Dark matter annihilates in WW^*, ZZ^*, and the off shell gauge bosons decay in Standard Model fermions KK'.

- $m_h \leqslant m_S \leqslant m_t$: in this mass range, the final state in hh becomes available, with three diagrams, that are those in fig. 5.1, other important channels are in W^+W^-, ZZ;

- $m_S \geqslant m_t$: for masses greater than the t quark mass, we have a new channel in $t\bar{t}$, in addition to the previous ones.

The channels in gg and in $\gamma\gamma$ are loop suppressed, so we have not considered them. We have computed the relic density with MicrOMEGAs 5.0.9 [130], by considering the simple case in which all the dark matter comes from our model. We have not used MadDM, because at the current stage the computation of the relic density does not consider $2 \to 3$ processes. In this case their contribution is important in the dark matter mass range $50\,\mathrm{GeV} \lesssim m_S \lesssim m_{W,Z}$, indeed, a comparison between MadDM and MicrOMEGAs 5.0.9 shows a difference of about 20–30%.

Thereupon we have computed the values of the parameters in order to obtain the correct relic density in eq. (3.49). For the singlet scalar Higgs portal model we have the following (approximate) proportionality relation:

$$\Omega h^2 \underset{\approx}{\propto} \frac{1}{\langle \sigma v \rangle} \underset{\approx}{\propto} \frac{1}{\lambda_{hS}^2} \,, \tag{5.29}$$

Therefore, fixing $\lambda_{hS}^{(n)}$ and computing $\Omega h^2_{(n)}$, we can apply the following recursive formula

$$\lambda_{hS}^{(n+1)} = \sqrt{\frac{\Omega h^2_{(n)}}{\Omega h^2|_{\text{PLANCK}}}} \lambda_{hS}^{(n)} \,. \tag{5.30}$$

until we have that $\Omega h^2_{(n+1)}$ is sufficiently close to the value $\Omega h^2|_{\text{PLANCK}}$. We associated to that number a theoretical uncertainty of 10%. In order to compute the values of λ_{hS} related to the uncertainty we can use the same previous formulae,

but we have to change the value of $\Omega h^2|_{\text{PLANCK}}$ according to:

$$\Omega h^2|_{\text{PLANCK}}^{\pm 10\%} = \frac{1}{1 \mp 10\%} \Omega h^2|_{\text{PLANCK}} . \tag{5.31}$$

Consequently we have added the γ-ray line 95% CL upper limits by FERMI-LAT [19] and HESS [20]: we will see that the possibility to compute the value of $\langle \sigma v \rangle_{\gamma\gamma}$ makes possible to determine the maximum value of λ_{hS} for each value of dark matter mass considered by the experiments. This has been done by exploiting the following relation, valid for a certain value of m_S:

$$\langle \sigma v \rangle_{\gamma\gamma} \propto \lambda_{hS}^2 , \tag{5.32}$$

Fixing m_S and $\lambda_{hS} = \lambda_{hS}^*$ we can compute $\langle \sigma v \rangle_{\gamma\gamma} = \langle \sigma v \rangle^*$ with MaDDM and then compute

$$\lambda_{hS}^{\text{ul}} = \sqrt{\frac{\langle \sigma v \rangle_{\gamma\gamma}^{\text{ul}}}{\langle \sigma v \rangle^*}} \lambda_{hS}^* , \tag{5.33}$$

where λ_{hS}^{ul} is the upper limit on λ_{hS}, due to the γ-ray line limits, expressed as $\langle \sigma v \rangle_{\gamma\gamma}^{\text{ul}}$.

Moreover we have studied the limits coming from direct detection, by considering the spin-independent cross section 90% CL upper limit as measured by XENON1T [100], by computing the maximum value of λ_{hS} for each value of m_S according to the following formula [131]:

$$\sigma_{\text{SI}} = \frac{\lambda_{hS}^2 f_n^2}{4\pi} \frac{\mu_n^2 m_n^2}{m_h^4 m_S^2} , \tag{5.34}$$

where $f_n = 0.30$. The term μ_n is the reduced mass of the dark matter-nucleon system, while $m_n = 0.939 \, \text{GeV}$ is the average between the proton and the neutron masses.

The last experimental result we have shown comes from the Higgs invisible decay width [110]. Considering the latter related only to Higgs decay in our dark matter candidate S, we can compute the invisible decay width [132]:

$$\Gamma_{\text{inv}} = \Gamma(h \to SS) = \frac{\lambda_{hS}^2 v^2}{32\pi m_h} \sqrt{1 - \frac{4m_S^2}{m_h^2}} , \tag{5.35}$$

where we have, recalling eq. (3.115),

$$\mathcal{B}(h \to \text{inv.}) = \frac{\Gamma_{\text{inv}}}{\Gamma_{\text{SM}} + \Gamma_{\text{inv}}} < 0.33 \, \text{at } 95\% \, \text{CL,} \tag{5.36}$$

where $\Gamma_{\text{SM}} = 4.07 \, \text{MeV}$ as pointed out above. Therefore we can compute the maximum value of λ_{hS} for each m_S using the eqs. above.

Plotting all the discussed results, we obtain the graph in fig. 5.6. First of all, the part of the parameter space below the relic density line is excluded, because it accounts for an higher relic density. This happens because the coupling
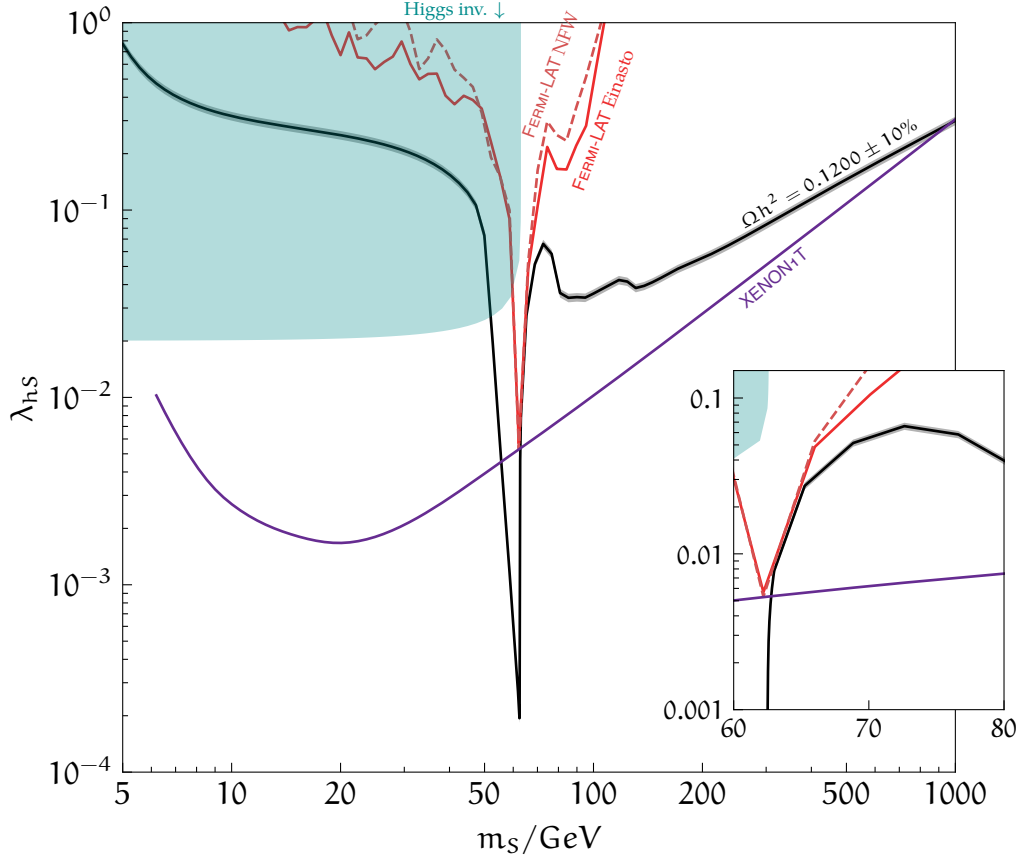
Figure 5.6: Parameter space of the singlet scalar Higgs portal model. The black line is the coupling that provides the observed relic density (Planck [3]) for each value of mass, with a 10% theoretical uncertainty grey band. Moreover we show the γ-ray line 95% CL upper limits from Fermi-LAT [19] (HESS [20] limits are not visible for these values of the parameters) for two different density profiles: Einasto (solid line) and NFW (dashed line). We show also the 90% CL upper limits from XENON1T [100] on the spin-independent cross section. Finally, the shaded area represents the excluded region due to Higgs invisible width 95% CL upper limit [110].

is low, so that annihilation proceeds at a lower rate. What is above that line represents instead the part of the parameter space that accounts for a relic density lower than the observed one, because the coupling is high. In principle this part is not excluded: if we suppose that our model does not describe the total amount of dark matter, but only a fraction of it, the value of the relic density we have to reproduce will be lower than the observed one. As expected, the relic density line drops when $m_S \approx m_h/2$, that is the resonance region, because $\langle \sigma v \rangle$ is enhanced. Other local minimum can be found around $m_{W,Z}$, when the processes in W^+W^-, ZZ are accessible, and where $m_S \approx m_h$, when the hh final state becomes available. The zoomed region represents an area of the parameter space when the constraints coming from Fermi-LAT limits are particularly close to the exclusion limits of the relic density. Adding up the XENON1T limit we are able to constrain a large part of the parameter space. The only available slice

becomes the part from $m_S \approx 55$ to $63\,\mathrm{GeV}$, delimited above by the XENON₁T upper limits, and below by the relic density lower limit. Another little slice can be found around $m_S \approx 1000\,\mathrm{GeV}$, when the relic density line drops below XENON₁T limit.

5.3   Simplified top-philic model

The simplified top-philic model we have considered is a simple extension of the Standard Model [13], made of a Majorana dark matter candidate χ, acting as a singlet under Standard Model gauge groups, and a coloured scalar particle $\tilde{t}$ with the same quantum numbers as the right t quark. We assume a $\mathbb{Z}_2$ symmetry, under which Standard Model particles are even, while $\chi \to -\chi$ and $\tilde{t} \to -\tilde{t}$ are odd. In this way we have that the dark matter candidate is stable when $m_\chi < m_{\tilde{t}}$. We can therefore write the following lagrangian:

$$\mathcal{L}_{\text{t-philic}} = \mathcal{D}_\mu \tilde{t}(\mathcal{D}^\mu \tilde{t})^\dagger - m_{\tilde{t}}^2 \tilde{t}^\dagger \tilde{t} + \overline{\chi}(i\slashed{\partial} - m_\chi)\chi + \lambda_\chi \tilde{t}\,\overline{t}\,P_L \chi + \text{h.c.}, \qquad (5.37)$$

where $\mathcal{D}_\mu$ is the covariant derivative. The term P_L is the left chirality projector, defined as $P_L = (1 - \gamma^5)/2$, where $\gamma^5 = i\gamma^0\gamma^1\gamma^2\gamma^3 = \text{diag}(-\mathbb{1}_2, \mathbb{1}_2)$. The particle $\tilde{t}$ is the t-channel mediator that allows dark matter to interact with Standard Model through the coupling λ_χ. The model has three free parameters: m_χ, $m_{\tilde{t}}$, λ_χ. We can make a parallelism with the Minimal Supersymmetric Standard Model (MSSM) [68–71] and recognise in $\tilde{t}$ the supersymmetric partner of t quark, called stop, while χ is the neutralino. In the MSSM, the neutralino is given by a mixing of bino e wino, and in this case the coupling is fixed $\lambda_\chi^{\text{MSSM}} = \frac{2\sqrt{2}e}{3\cos\vartheta_W} \approx 0.33$, by their gauge couplings. However, the model can be also considered as a low energy limit of a non-supersymmetric scenario. This is indeed the case we are interested on, treating λ_χ as a free parameter. We notice that the lagrangian (5.37) can in principle contain another interaction term: $\tilde{t}^\dagger \tilde{t} \varphi^\dagger \varphi$, where φ is the Higgs boson doublet. That interaction will affect the $\tilde{t}\tilde{t}$ annihilation cross section, the coannihilation rate, the χ-nucleon scattering rate and the loop-induced annihilation of χ via an Higgs boson. However we can neglect that term by imposing its related coupling very low. Moreover, we will consider a mass splitting $\Delta m = m_{\tilde{t}} - m_\chi \geqslant 10\,\mathrm{GeV}$, so that we can safely neglect the effects of flavour-violating coupling of $\tilde{t}$ to other up-like quarks [133]. This kind of couplings can indeed be generated by the renormalisation group, but they are negligible if the mass splitting is sufficiently high. The main annihilation and coannihilation $2 \to 2$ LO diagrams that contribute to the relic density are shown in fig. 5.7.

Loop-induced annihilation $\chi\chi \to \gamma\gamma$

We know that annihilation of dark matter in photons $\chi\chi \to \gamma\gamma$ is a loop-induced process, and this can be seen clearly in the related diagrams in fig. 5.8.
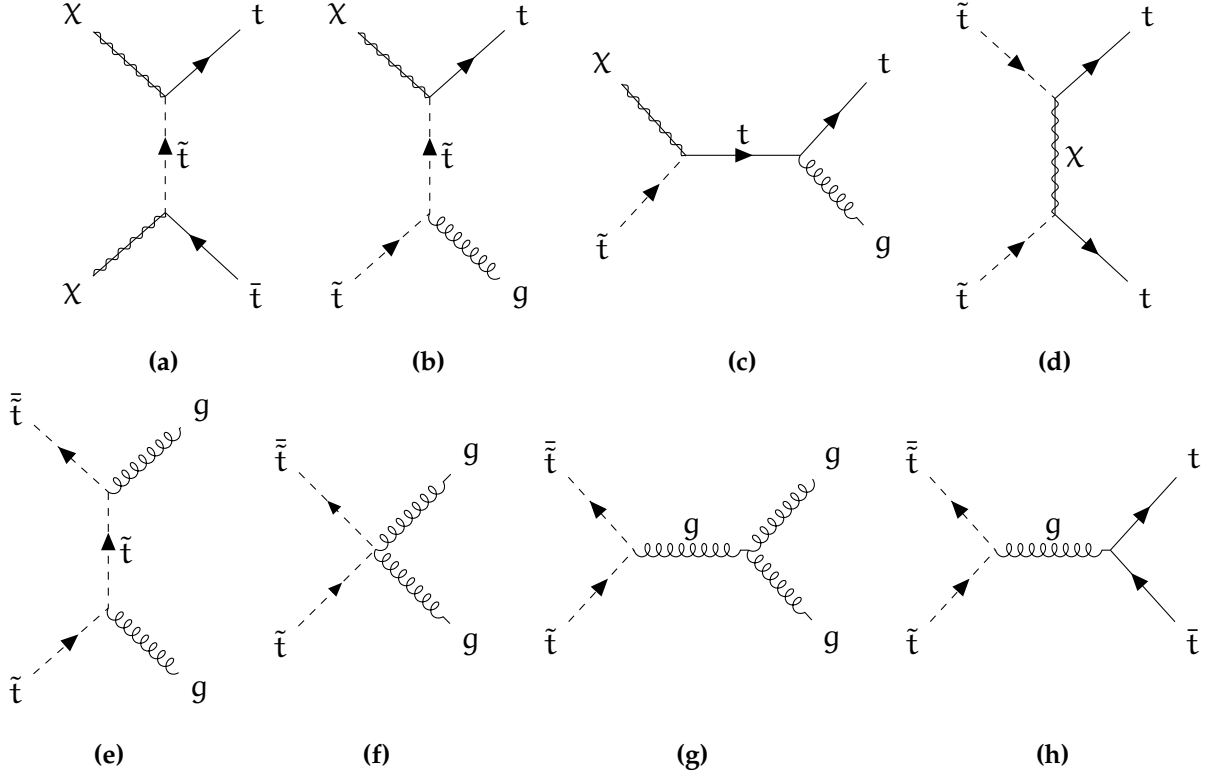
Figure 5.7: Leading-Order $2 \to 2$ annihilation and coannihilation diagrams for the simplified top-philic model. Fig. a shows the only one proper annihilation diagram.

We have implemented the model in UFO format with NLO correction, to import it in MADDM. To test the numerical computation of the loop-induced integral we have compared the results with analytical formulae [17, 18]. Those come from the general MSSM, but we can simplify them by considering our simple model, where the neutralino couples only to squarks. We obtain:

$$\langle \sigma v \rangle_{\gamma\gamma} = \frac{N_C^2 Q_t^4 \lambda_\chi^4 \alpha_e^2}{16\pi^3 m_\chi^2} \left[\left(\mathcal{R}e\tilde{A}_{t\tilde{t}}\left(\frac{m_\chi^2}{m_{\tilde{t}}^2}, \frac{m_t^2}{m_{\tilde{t}}^2}\right) \right)^2 + \left(\mathcal{I}m\tilde{A}_{t\tilde{t}}\left(\frac{m_\chi^2}{m_{\tilde{t}}^2}, \frac{m_t^2}{m_{\tilde{t}}^2}\right) \right)^2 \right], \quad (5.38)$$

where $N_C = 3$, $Q_t = 2/3$. We have the definitions of the functions

$$\mathcal{R}e\tilde{A}_{t\tilde{t}}(a,b) = \frac{1}{4}\frac{b}{1+a-b}\left(I_1(a,b) + 2\,I_3(a,b)\right) + \frac{1}{4}\frac{1}{1-b}\left(I_2(a,b) - b\,I_3(a,b)\right),$$
$$(5.39)$$

$$\mathcal{I}m\tilde{A}_{t\tilde{t}}(a,b) = -\frac{\pi}{4}\frac{b}{1+a-b}\log\left(\frac{1+\sqrt{1-b/a}}{1-\sqrt{1-b/a}}\right)\vartheta(a-b), \quad (5.40)$$

with $\vartheta(x)$ being the *Heaviside's Theta function*. The functions I_1, I_2, I_3 arise from three point loop integrals. Before going through them, it is useful to define the quantities:

$$\Delta_1(a,b) \doteq (a+b-1)^2 + 4a, \quad (5.41a)$$
$$\Delta_2(a,b) \doteq (b-a-1)^2 - 4a. \quad (5.41b)$$
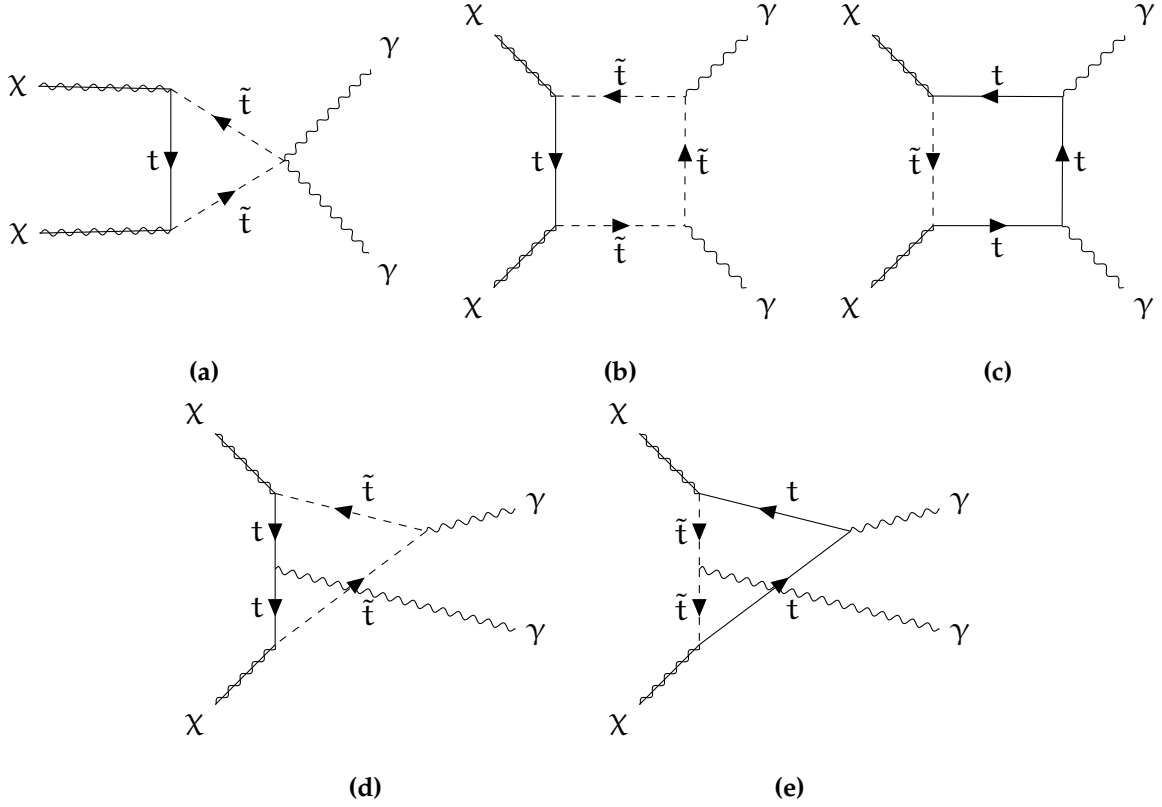
Figure 5.8: Loop-induced annihilation diagrams in photons (unitary gauge) for the simplified top-philic model.

We can write:

$$I_1(a, b) = \frac{1}{2}\left[\log^2\left(\frac{1 + \sqrt{1 - b/a}}{1 - \sqrt{1 - b/a}}\right) - \pi^2\right]\vartheta(a - b)$$
$$- 2\arctan^2\left(\frac{1}{\sqrt{b/a - 1}}\right)\vartheta(b - a), \qquad (5.42)$$

$$I_2(a, b) = -\operatorname{Li}_2\left(\frac{1 - a - b - \sqrt{\Delta_2(a, b)}}{2}\right) - \operatorname{Li}_2\left(\frac{1 - a - b + \sqrt{\Delta_1(a, b)}}{2}\right)$$
$$+ \left[\operatorname{Li}_2\left(\frac{1 + a - b - \sqrt{\Delta_2(a, b)}}{2}\right) + \operatorname{Li}_2\left(\frac{1 + a - b + \sqrt{\Delta_2(a, b)}}{2}\right)\right]\vartheta(\Delta_2(a, b))$$
$$+ 2\mathcal{R}e\operatorname{Li}_2\left[\sqrt{a}\exp\left(i\arccos\left(\frac{1 + a - b}{2\sqrt{a}}\right)\right)\right]\vartheta(-\Delta_2(a, b)),$$
$$(5.43)$$

Table 5.2: Comparison between the numerical computation made by MADDM and the analytical formulae for $\langle \sigma v \rangle_{\gamma\gamma}$ in the framework of the simplified top-philic model. We have fixed $\lambda_\chi = 0.1$.

m_χ/GeV	$m_{\tilde{t}}/\text{GeV}$		$\langle \sigma v \rangle_{\gamma\gamma}/(\text{cm}^3\,\text{s}^{-1})$
200	300	numerical	4.59×10^{-34}
		analytical	4.66×10^{-34}
400	500	numerical	1.954×10^{-34}
		analytical	1.979×10^{-34}
500	600	numerical	1.444×10^{-34}
		analytical	1.457×10^{-34}
700	800	numerical	8.867×10^{-35}
		analytical	8.943×10^{-35}
750	800	numerical	1.008×10^{-34}
		analytical	1.022×10^{-34}
1000	1200	numerical	3.55×10^{-35}
		analytical	3.62×10^{-35}
1100	1200	numerical	4.40×10^{-35}
		analytical	4.44×10^{-35}

$$I_3(a,b) = -I_2(a,b) + \log^2\left(\frac{1+a+b+\sqrt{\Delta_1(a,b)}}{2\sqrt{b}}\right)$$
$$- \log^2\left(\frac{1-a+b+\sqrt{\Delta_2(a,b)}}{2\sqrt{b}}\right)\vartheta\left(\Delta_2(a,b)\right)$$
$$+ \left[\frac{\pi}{2} - \arctan\left(\frac{1+b-a}{\sqrt{-\Delta_2(a,b)}}\right)\right]^2 \vartheta\left(-\Delta_2(a,b)\right), \quad (5.44)$$

The function $\text{Li}_2(z)$ is the dilogarithm function, defined as:

$$\text{Li}_2(z) = -\int_0^z \frac{\log(1-t)}{t}\,dt\,. \quad (5.45)$$

We have chosen few values of the parameters and made the comparison in tab. 5.2. The numerical results agree with the analytical ones with a maximum relative error of 1.9%. MADDM is in very good agreement with the analytical formulae.

Phenomenology of the simplified top-philic model

The simplified top-philic model has three free parameters, m_χ, $m_{\tilde{t}}$, λ_χ. Hence, the study of the phenomenology is more complex than in the singlet scalar Higgs

portal model. A recent result can be found in [13], where the same model is analysed and characterised in depth. We will take the main results from it, we will add the γ-ray line limits [19, 20] and the direct detection limit [100]. The parameter space we have studied is (m_χ, λ_χ), $m_{\tilde{t}}$ is fixed by choosing:

$$\Delta m = m_{\tilde{t}} - m_\chi = m_t \approx 172 \, GeV. \tag{5.46}$$

For the relic density, we have adopted the results from [13], where the authors performed the computation for different values of the parameters:

- $m_\chi \in [100, 2 \times 10^5] \, GeV$, in logarithmic scale;

- $\lambda_\chi \in [0.3, 14]$, in logarithmic scale.

A mass splitting as in eq. (5.46) ensures that the relic density is governed by the usual freeze-out mechanism, because $\tilde{t}$ and χ are in chemical equilibrium, i.e. the condition in eq. (3.80) holds. A lower mass splitting would make that assumption breaking down; in this case the relic density is governed by the so called conversion-driven freeze-out [134], that we will not discuss.
In the case of chemical equilibrium between $\tilde{t}$ and χ, we have that the relic density depends on the annihilation and coannihilation processes involving χ, t and $\tilde{t}$. The velocity-averaged cross section has various contributions, as we have discussed in § 3.7, recalling eq. (3.83), we can write the effective cross section

$$\sigma_{\text{eff}} \doteq \sum_{i,j \in \{\chi, t, \tilde{t}\}} \sigma_{ij} \frac{n_i^{eq} n_j^{eq}}{n^{eq\,2}}, \tag{5.47}$$

where we have to consider the degrees of freedom: $g_\chi = 2$, $g_{\tilde{t}} = 3$. On the basis of the centre-of-mass energy $\sqrt{s} \approx 2m_\chi$, so depending on m_χ, we have different processes:

- $m_\chi \gtrsim m_t$: the main annihilation process is $\chi\chi \to t\bar{t}$ in fig. 5.7a; in addition we have the coannihilation processes $\chi\tilde{t} \to tg$ in figs. 5.7b and 5.7c and $\tilde{t}\bar{\tilde{t}} \to gg$ in figs. 5.7e–5.7g, the last ones depend solely on g_s (strong coupling constant), so they are an important contribution for low λ_χ;

- $m_\chi < m_t$: the process $\chi\chi \to t\bar{t}$ is no more kinematically allowed, the relic density is characterised by the loop-induced process $\chi\chi \to gg$ (whose diagrams are the same as in fig. 5.8 by substitution of γ with g) and by the $2 \to 3$ processes $\chi\chi \to W^+ b\bar{t}$, $\chi\chi \to W^- \bar{b}t$, shown in fig. 5.9. In this mass range we can have also the loop-induced processes $\chi\chi \to h \to K\bar{K}$, shown in fig. 5.10, with K any massive kinematically allowed Standard Model particle, such as b, W, . . . ; this process is enhanced on the Higgs resonance $m_\chi \approx m_h/2$;

- the choice of the mass splitting as in eq. (5.46) makes $m_{\tilde{t}} > m_t$ and that means the processes in figs. 5.7d and 5.7h are always possible;
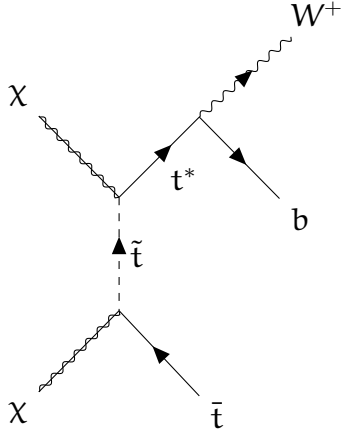
Figure 5.9: The $2 \to 3$ process $\chi\chi \to W^+ b\bar{t}$. The diagram for the other process $\chi\chi \to W^- \bar{b}t$ is similar.
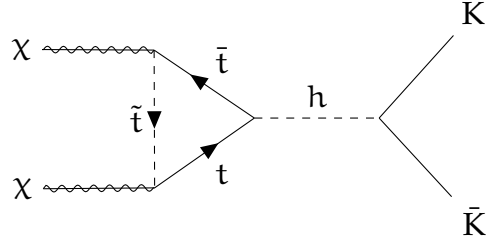
Figure 5.10: Loop-induced annihilation of χ in Standard Model massive particle K, through Higgs exchange. This process is enhanced on the Higgs resonance, $m_\chi \approx m_h/2$.

- for the same reason, also the processes in figs. 5.7b and 5.7c are always possible independently on the value of m_χ.

In [13], the authors considered the value of the correct relic density from the old measurement performed by PLANCK [135] (we will refer to it as PLANCK15):

$$\Omega h^2|_{\text{PLANCK15}} = 0.1199 \pm 0.0027 , \tag{5.48}$$

with a 10% theoretical uncertainty. With respect to the results in [13], we have added the 95% CL γ-ray line limits provided by FERMI-LAT [19] and HESS [20]. Following the same approach as in § 5.2, we have made a rescaling using a formula similar to eq. (5.33), exploiting the following proportionality relation valid for a certain m_χ

$$\langle \sigma v \rangle_{\gamma\gamma} \propto \lambda_\chi^4 , \tag{5.49}$$

and the fact that MADDM can compute $\langle \sigma v \rangle_{\gamma\gamma}$ straightforwardly.
For the direct detection constraints, we have updated the results in [13], considering the most recent results by XENON1T [100]. We have taken the $\sigma_{\text{SI}} = \sigma_{\text{SI}}^*$ computation that was performed by [13] for each value of m_χ, fixing $\lambda_\chi = \lambda_\chi^*$, and we have made a rescaling, finding the upper limit λ_χ^{ul}, on the basis of the 90% CL upper limit $\sigma_{\text{SI}}^{\text{ul}}$ provided by [100]:

$$\lambda_\chi^{\text{ul}} = \sqrt[4]{\frac{\sigma_{\text{SI}}^{\text{ul}}}{\sigma_{\text{SI}}^*}} \lambda_\chi^* . \tag{5.50}$$

For what concerns experimental limits from collider searches we have adopted the results of [13], considering the $\tilde{t}$ searches performed by CMS and ATLAS. A large number of searches for the neutralino-stop sector were performed, the $\tilde{t}$ production is independent on the coupling strength λ_χ because depends only
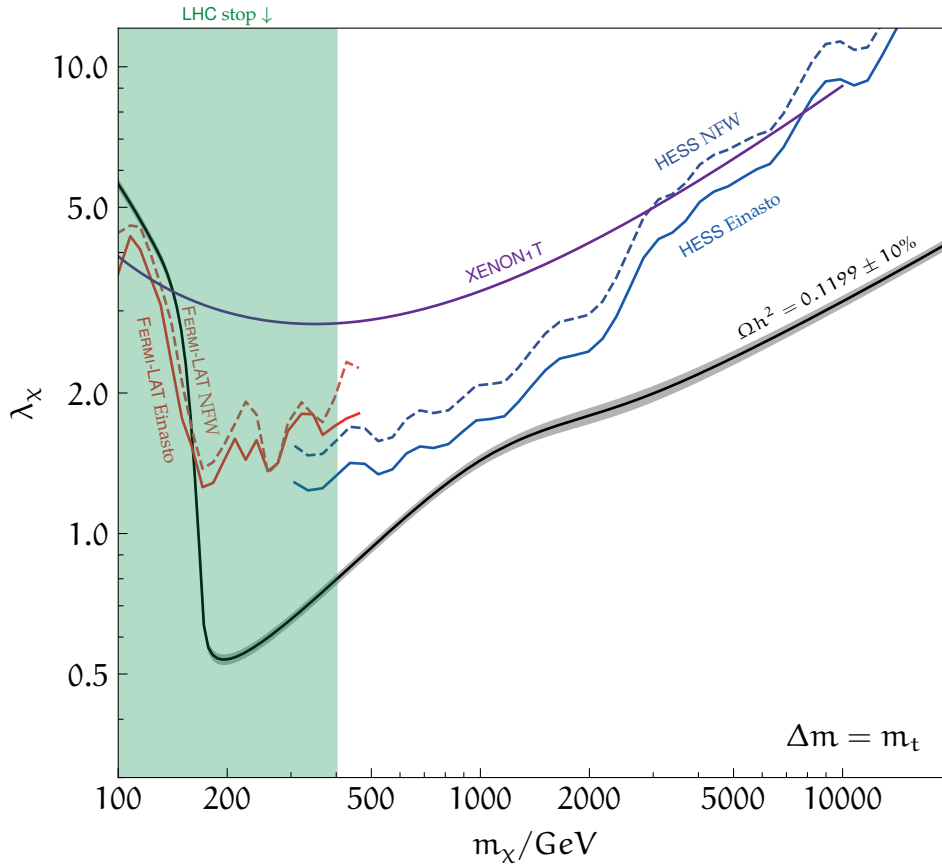
Figure 5.11: Parameter space of the simplified top-philic model. The black line is the coupling that provides the observed relic density (Pʟᴀɴᴄᴋ15 [135]) for each value of mass, with a 10% theoretical uncertainty grey band (result taken from [13]). Moreover we show the 95% CL γ-ray line upper limits from Fᴇʀᴍɪ-LAT [19] and HESS [20] for two different density profiles: Einasto (solid lines) and NFW (dashed lines). We show also the 90% CL upper limits on the spin-independent cross section from XENON1T [100]. Finally, the shaded area represents the 95% CL combined excluded region due to the stop searches at colliders performed by both CMS [136–138] and ATLAS [139–141].

on his gauge interactions, so these searches do not make any reference to the strength of the λ_χ coupling. In order to remain in the framework of the simplified top-philic model, we can consider the results for $\tilde{t}$ decays that do not involve other supersymmetric particles. We have considered the LHC 13 TeV following analysis: CMS fully hadronic [136, 137], CMS single lepton [138], ATLAS fully hadronic [139], ATLAS single lepton [140] and ATLAS two leptons [141]. In [13], the authors have combined them and analysed the resulting 95% CL exclusion region on the parameters $(m_\chi, \Delta m)$. In this case we have taken the bounds for the mass splitting (5.46), that results in the exclusion region $m_\chi \notin [56, 400]$ GeV (from now on labelled 'LHC stop').

Plotting the discussed results we obtain the graph in fig. 5.11. First of all the part of the parameter space below the relic density line is excluded. The relic density

drops when $m_\chi \approx m_t$ where we have that $t\bar{t}$ production is kinematically allowed. Collider searches limits exclude a large region, with masses below $400\,\text{GeV}$, while XENON1T limits exclude the high coupling region. With respect to the analysis carried out by [13], we obtain the strongest limits for $800\,\text{GeV} \lesssim m_\chi \lesssim 8\,\text{TeV}$, given by the γ-ray line limits by HESS. In the region $m_\chi \gtrsim 8\,\text{TeV}$ the XENON1T limits are slightly stronger. For $400\,\text{GeV} \lesssim m_\chi \lesssim 800\,\text{GeV}$ the strongest limits are given by the measurement on cosmic-ray antiproton fluxes performed by AMS-02 [142] and reported in [13]. In [13], the authors considered the limits for γ-ray continuous searches coming from the analysis of dwarf spheroidal galaxies by FERMI-LAT [124]. In the case of this model, in the low mass region, the constraints coming from γ-ray line searches are more promising with respect to those from continuous searches. This happens because for $m_\chi \ll m_t$, we have seen that the annihilation process $\chi\chi \to t\bar{t}$ is inefficient and the loop-induced annihilation $\chi\chi \to gg$, that yields a continuum spectrum of photons, is the dominant channel during freeze-out. That process proceeds via the same loop diagrams as the annihilation in $\gamma\gamma$, shown in fig. 5.8 (upon substitution of γ with g). We can relate their cross sections, obtaining [143]:

$$\frac{\langle\sigma v\rangle_{\gamma\gamma}}{\langle\sigma v\rangle_{gg}} = \frac{Q_t^4 N_C \alpha_e^2}{2\alpha_s^2}\,, \tag{5.51}$$

where $\alpha_s = g_s^2/(4\pi)$. An estimation of the ratio can be obtained by evaluating α_s at a fixed energy scale μ. For $\mu = 300\,\text{GeV}$ we have $\langle\sigma v\rangle_{\gamma\gamma}/\langle\sigma v\rangle_{gg} \approx 0.5\%$. So, in the low mass region, the process yielding the continuum γ-ray spectrum and the annihilation in γ-ray line are not very different in size and are both loop-suppressed. The greater sensitivity of the line searches channel allows for the line limits to be stronger than the continuous ones. In contrast, in the region $m_\chi > m_t$, the annihilation into $t\bar{t}$ (that results in a continuum γ-ray spectrum) is not loop-suppressed. Its cross section will be larger than that from the annihilation in $\gamma\gamma$ and the limits on the continuum signal will be likely stronger.

Chapter 6

Conclusion and outlook

In this thesis we investigated loop-induced annihilation of dark matter. In particular, we focused on the γ-ray line signal, arising from the annihilation into a pair of photons, an important indirect detection signature, because of the low background. The computation of loop-induced processes can in principle be done with numerical tools, however no dark matter tool was able to do it for arbitrary models so far. In this thesis we studied MADDM, and we updated it by adding this feature. We gave an outline on the main numerical techniques that are used to make a loop-induced computation and we described three MATHEMATICA packages: FEYNRULES, FEYNARTS and NLOCT, that allows to implement any dark matter model at NLO in MADDM. We validated the new feature by studying two dark matter models. The first one is the singlet scalar Higgs portal model, it is constituted by a scalar WIMP dark matter particle S, that couples with Standard Model through the Higgs boson. We computed the loop-induced process $SS \rightarrow \gamma\gamma$ with MADDM and we compared the results with the Higgs effective field theory, in which the same process is a tree-level process, that can be handled easily by MADDM. The results were in perfect agreement for different values of the parameters. The second model we studied is a simplified top-philic model, made of a Majorana spinor dark matter particle χ and a scalar coloured mediator $\tilde{t}$ with the same quantum number as the right top quark. We computed the loop-induced process $\chi\chi \rightarrow \gamma\gamma$ with MADDM and we compared the results with analytical formulae, obtaining excellent agreement. These tests show that the loop-induced feature is correctly implemented in MADDM and works extremely well for simple models.

We used the code to analyse the parameter space of the models, inferring important constraints on it, based on the γ-ray line searches by the experiments FERMI-LAT and HESS, that placed upper limits on the value of $\langle \sigma v \rangle_{\gamma\gamma}$. For the singlet scalar Higgs portal model we studied the parameter space by varying the mass of the dark matter m_S and the coupling λ_{hS}, between S and Higgs boson. We computed the value of λ_{hS} that accounts for the measured relic density for each value of m_S. Consequently we implemented the limits coming from direct detection (XENON1T) and Higgs invisible decay width, that allowed us to constrain a large part of the parameter space. Finally we added the limits coming

from γ-ray line searches by FERMI-LAT. We observed that the parameter space compatible with constraints corresponds to a mass interval of $m_S \approx 55$ to $63\,GeV$ around $m_h/2$, that is the resonance region.

For the simplified top-philic model we considered the parameter space made of the dark matter mass m_χ and the coupling λ_χ, between dark matter and the mediator $\tilde{t}$. We fixed $m_{\tilde{t}} = m_\chi + m_t$, where t is the top quark. We took the previous results of [13], where the authors computed the relic density for the same choice of the parameters. We updated it, adding the γ-ray line limits by FERMI-LAT and HESS. Considering all the constraints, the allowed parameter space is above the relic density line, constrained by the AMS-02 limits for $400\,GeV \lesssim m_\chi \lesssim 800\,GeV$ and by the HESS γ-ray line limits for $800\,GeV \lesssim m_\chi \lesssim 8\,TeV$. The region $m_\chi \lesssim 400\,GeV$ is excluded by LHC limits, while the region $m_\chi \gtrsim 8\,TeV$ is constrained by the XENON1T direct detection limits. With respect to previous results, the HESS γ-ray line limits allows to rule out a large part of the parameter space.

In future works, we will validate MADDM on more complicated models, as the Inert Doublet Model (IDM) [144–146], in order to finalise the validation of the loop-induced processes and provide a new release of the code, that will include this feature. Moreover we will use the code to derive interesting constraints on IDM parameters, extending previous analysis [147, 148].

Acknowledgments

First of all I would like to express deep gratitude to Professor Fabio Maltoni, for the support in this last year and for giving me the opportunity to spend six months at the *Centre for Cosmology, Particle Physics and Phenomenology* (CP3) to write this thesis and working with his research group.

I am also deeply grateful to my supervisor Jan Heisig, for proposing me this amazing project, for the support in these six months and for teaching me what it means to be a researcher. Thank you for letting me discover dark matter and for all the help you gave me.

Special thank also to Chiara Arina, for the persistence support, the advices and the patience. I have really appreciated your help.

I am particularly thankful for the assistance given by Olivier Mattelaer (for MadGraph5_aMC@NLO and MadDM) and by Céline Degrande (for FeynRules and NLOCT).

I want to thank the entire staff of CP3 and all the people I have met there for the great hospitality I have received.

Many thanks also to the awesome people of the 'Louvain group', for sharing their time with me. Thank you for all the nights spent in tasting beers, playing pool, bowling and sing at karaoke.

Voglio ringraziare Federico, per aver condiviso con me l'esperienza di essere catapultati all'estero all'improvviso, per le discussioni fino a tarda sera e per la sua deliziosa carbonara.

Un grazie anche ai miei amici, per il costante supporto in questi cinque anni di studio, per tutti i momenti divertenti che abbiamo trascorso e che mi hanno aiutato ad affrontare tutto con più serenità. Grazie soprattutto a Giacomo, per le continue chiacchierate, i consigli e per tutte le volte che abbiamo preso il treno a orari improponibili con la sola consolazione di una colazione da RistòPallotti.

Un enorme grazie alla mia famiglia. Questi anni sono stati intensi, e il vostro aiuto è stato essenziale. Non sarei mai arrivato a questo punto senza il vostro costante supporto, i continui consigli e la piena disponibilità. Un solo grazie non è sufficiente.

Infine un ringraziamento speciale va a Federica, per essere stata una costante presenza da (quasi) cinque anni a questa parte. Insieme abbiamo condiviso viaggi, esperienze, successi e difficoltà. Sei una parte insostituibile della mia vita. Senza di te non sarei mai diventato quello che sono ora.

Bibliography

[1] F. Zwicky. 'Die Rotverschiebung von extragalaktischen Nebeln'. *Helvetica Physica Acta* 6 (Jan. 1933), pp. 110–127.

[2] Vera C. Rubin and Jr. Ford W. Kent. 'Rotation of the Andromeda Nebula from a Spectroscopic Survey of Emission Regions'. *Astrophysical Journal* 159 (Feb. 1970), p. 379. DOI: 10.1086/150317.

[3] N. Aghanim et al. 'Planck 2018 results. VI. Cosmological parameters' (2018). arXiv: 1807.06209 [astro-ph.CO].

[4] Federico Ambrogi et al. 'MadDM v.3.0: a Comprehensive Tool for Dark Matter Studies'. *Phys. Dark Univ.* 24 (2019), p. 100249. DOI: 10.1016/j.dark.2018.11.009. arXiv: 1804.00044 [hep-ph].

[5] Johan Alwall et al. 'MadGraph 5 : Going Beyond'. *JHEP* 06 (2011), p. 128. DOI: 10.1007/JHEP06(2011)128. arXiv: 1106.0522 [hep-ph].

[6] J. Alwall et al. 'The automated computation of tree-level and next-to-leading order differential cross sections, and their matching to parton shower simulations'. *JHEP* 07 (2014), p. 079. DOI: 10.1007/JHEP07(2014)079. arXiv: 1405.0301 [hep-ph].

[7] G. Belanger et al. 'micrOMEGAs_3: A program for calculating dark matter observables'. *Comput. Phys. Commun.* 185 (2014), pp. 960–985. DOI: 10.1016/j.cpc.2013.10.016. arXiv: 1305.0237 [hep-ph].

[8] Torsten Bringmann et al. 'DarkSUSY 6 : An Advanced Tool to Compute Dark Matter Properties Numerically'. *JCAP* 1807.07 (2018), p. 033. DOI: 10.1088/1475-7516/2018/07/033. arXiv: 1802.03399 [hep-ph].

[9] Valentin Hirschi and Olivier Mattelaer. 'Automated event generation for loop-induced processes'. *JHEP* 10 (2015), p. 146. DOI: 10.1007/JHEP10(2015)146. arXiv: 1507.00020 [hep-ph].

[10] Vanda Silveira and A. Zee. 'Scalar Phantoms'. *Physics Letters B* 161.1 (1985), pp. 136–140. ISSN: 0370-2693. DOI: https://doi.org/10.1016/0370-2693(85)90624-0. URL: http://www.sciencedirect.com/science/article/pii/0370269385906240.

[11] C. P. Burgess, Maxim Pospelov, and Tonnis ter Veldhuis. 'The Minimal model of nonbaryonic dark matter: A Singlet scalar'. *Nucl. Phys.* B619 (2001), pp. 709–728. DOI: 10.1016/S0550-3213(01)00513-2. arXiv: hep-ph/0011335 [hep-ph].

[12] Alessandro Cuoco et al. 'A global fit of the γ-ray galactic center excess within the scalar singlet Higgs portal model'. *JCAP* 1606.06 (2016), p. 050. DOI: `10.1088/1475-7516/2016/06/050`. arXiv: `1603.08228 [hep-ph]`.

[13] Mathias Garny et al. 'Top-philic dark matter within and beyond the WIMP paradigm'. *Phys. Rev.* D97.7 (2018), p. 075002. DOI: `10.1103/PhysRevD.97.075002`. arXiv: `1802.00814 [hep-ph]`.

[14] Mikhail A. Shifman et al. 'Low-Energy Theorems for Higgs Boson Couplings to Photons'. *Sov. J. Nucl. Phys.* 30 (1979). [Yad. Fiz.30,1368(1979)], pp. 711–716.

[15] S. Dawson. 'Radiative corrections to Higgs boson production'. *Nucl. Phys.* B359 (1991), pp. 283–300. DOI: `10.1016/0550-3213(91)90061-2`.

[16] M. Spira et al. 'Higgs boson production at the LHC'. *Nucl. Phys.* B453 (1995), pp. 17–82. DOI: `10.1016/0550-3213(95)00379-7`. arXiv: `hep-ph/9504378 [hep-ph]`.

[17] Lars Bergström. 'Radiative processes in dark matter photino annihilation'. *Physics Letters B* 225.4 (1989), pp. 372–380. ISSN: 0370-2693. DOI: `https://doi.org/10.1016/0370-2693(89)90585-6`. URL: `http://www.sciencedirect.com/science/article/pii/0370269389905856`.

[18] Lars Bergström and Piero Ullio. 'Full one loop calculation of neutralino annihilation into two photons'. *Nucl. Phys.* B504 (1997), pp. 27–44. DOI: `10.1016/S0550-3213(97)00530-0`. arXiv: `hep-ph/9706232 [hep-ph]`.

[19] M. Ackermann et al. 'Updated search for spectral lines from Galactic dark matter interactions with pass 8 data from the Fermi Large Area Telescope'. *Phys. Rev.* D91.12 (2015), p. 122002. DOI: `10.1103/PhysRevD.91.122002`. arXiv: `1506.00013 [astro-ph.HE]`.

[20] H. Abdallah et al. 'Search for γ-Ray Line Signals from Dark Matter Annihilations in the Inner Galactic Halo from 10 Years of Observations with H.E.S.S.'. *Phys. Rev. Lett.* 120.20 (2018), p. 201101. DOI: `10.1103/PhysRevLett.120.201101`. arXiv: `1805.05741 [astro-ph.HE]`.

[21] Adam Alloul et al. 'FeynRules 2.0 - A complete toolbox for tree-level phenomenology'. *Comput. Phys. Commun.* 185 (2014), pp. 2250–2300. DOI: `10.1016/j.cpc.2014.04.012`. arXiv: `1310.1921 [hep-ph]`.

[22] Thomas Hahn. 'Generating Feynman diagrams and amplitudes with FeynArts 3'. *Comput. Phys. Commun.* 140 (2001), pp. 418–431. DOI: `10.1016/S0010-4655(01)00290-9`. arXiv: `hep-ph/0012260 [hep-ph]`.

[23] Celine Degrande. 'Automatic evaluation of UV and R2 terms for beyond the Standard Model Lagrangians: a proof-of-principle'. *Comput. Phys. Commun.* 197 (2015), pp. 239–262. DOI: `10.1016/j.cpc.2015.08.015`. arXiv: `1406.3030 [hep-ph]`.

[24] Edward W. Kolb and Michael S. Turner. *"The Early Universe"*. Frontiers in Physics. Addison–Wesley Publishing Company, 1990. ISBN: 9780201116038.

[25] Peter Coles and Francesco Lucchin. *"Cosmology"*. *"The Origin and Evolution of Cosmic Structure"*. 2nd ed. "John Wiley & Sons, Ltd", 2002. ISBN: 9780471489092.

[26] Sohrab Rahvar. 'Cooling in the universe' (2006). arXiv: `physics/0603087 [physics]`.

[27] Jaan Einasto. 'Dark Matter'. *arXiv e-prints*, arXiv:0901.0632 (Jan. 2009), arXiv:0901.0632. arXiv: `0901.0632 [astro-ph.CO]`.

[28] Gianfranco Bertone and Dan Hooper. 'History of dark matter'. *Rev. Mod. Phys.* 90.4 (2018), p. 045002. DOI: `10.1103/RevModPhys.90.045002`. arXiv: `1605.04909 [astro-ph.CO]`.

[29] Sidney van den Bergh. 'The Early history of dark matter'. *Publ. Astron. Soc. Pac.* 111 (1999), p. 657. DOI: `10.1086/316369`. arXiv: `astro-ph/9904251 [astro-ph]`.

[30] Martin Bauer and Tilman Plehn. 'Yet Another Introduction to Dark Matter' (2017). arXiv: `1705.01987 [hep-ph]`.

[31] Marco Cirelli. 'Indirect Searches for Dark Matter: a status review'. *Pramana* 79 (2012), pp. 1021–1043. DOI: `10.1007/s12043-012-0419-x`. arXiv: `1202.1454 [hep-ph]`.

[32] Jennifer M. Gaskins. 'A review of indirect searches for particle dark matter'. *Contemp. Phys.* 57.4 (2016), pp. 496–525. DOI: `10.1080/00107514.2016.1175160`. arXiv: `1604.00014 [astro-ph.HE]`.

[33] Jan Conrad and Olaf Reimer. 'Indirect dark matter searches in gamma and cosmic rays'. *Nature Phys.* 13.3 (2017), pp. 224–231. DOI: `10.1038/nphys4049`. arXiv: `1705.11165 [astro-ph.HE]`.

[34] Tracy R. Slatyer. 'Indirect Detection of Dark Matter'. In: *Proceedings, Theoretical Advanced Study Institute in Elementary Particle Physics : Anticipating the Next Discoveries in Particle Physics (TASI 2016): Boulder, CO, USA, June 6-July 1, 2016*. 2018, pp. 297–353. DOI: `10.1142/9789813233348_0005`. arXiv: `1710.05137 [hep-ph]`.

[35] Michael Klasen, Martin Pohl, and Günter Sigl. 'Indirect and direct search for dark matter'. *Prog. Part. Nucl. Phys.* 85 (2015), pp. 1–32. DOI: `10.1016/j.ppnp.2015.07.001`. arXiv: `1507.03800 [hep-ph]`.

[36] Katherine Freese, Mariangela Lisanti, and Christopher Savage. 'Colloquium: Annual modulation of dark matter'. *Rev. Mod. Phys.* 85 (2013), pp. 1561–1581. DOI: `10.1103/RevModPhys.85.1561`. arXiv: `1209.3339 [astro-ph.CO]`.

[37] Sinclair Smith. 'The Mass of the Virgo Cluster'. *Astrophysical Journal* 83 (Jan. 1936), p. 23. DOI: `10.1086/143697`.

[38] Erik Holmberg. 'A Study of Double and Multiple Galaxies Together with Inquiries into some General Metagalactic Problems'. *Annals of the Observatory of Lund* 6 (Jan. 1937), pp. 1–173.

[39] Thornton Page. 'Radial Velocities and Masses of Double Galaxies.' *Astrophysical Journal* 116 (July 1952), p. 63. DOI: 10.1086/145593.

[40] G. C. Mc Vittie. 'Problems of Extragalactic Research'. In: (Aug. 12–12, 1961). Ed. by G. C. Mc Vittie. Santa Barbara, CA, USA: The Mac Millan Company, 1962.

[41] Horace W. Babcock. 'The rotation of the Andromeda Nebula'. *Lick Observatory Bulletin* 498 (Jan. 1939), pp. 41–51. DOI: 10.5479/ADS/bib/1939LicOB.19.41B.

[42] J. H. Oort. 'Some Problems Concerning the Structure and Dynamics of the Galactic System and the Elliptical Nebulae NGC 3115 and 4494.' *Astrophysical Journal* 91 (Apr. 1940), p. 273. DOI: 10.1086/144167.

[43] H. C. van de Hulst, E. Raimond, and H. van Woerden. 'Rotation and density distribution of the Andromeda nebula derived from observations of the 21-cm line'. *Bulletin Astronomical Institute of the Netherlands* 14 (Nov. 1957), p. 1.

[44] Morton S. Roberts. 'A High-Resolution 21-CM Hydrogen-Line Survey of the Andromeda Nebula'. *Astrophysical Journal* 144 (May 1966), p. 639. DOI: 10.1086/148645.

[45] K. C. Freeman. 'On the Disks of Spiral and S0 Galaxies'. *Astrophysical Journal* 160 (June 1970), p. 811. DOI: 10.1086/150474.

[46] D. H. Rogstad and G. S. Shostak. 'Gross Properties of Five Scd Galaxies as Determined from 21-CENTIMETER Observations'. *Astrophysical Journal* 176 (Sept. 1972), p. 315. DOI: 10.1086/151636.

[47] M. Milgrom. 'A modification of the Newtonian dynamics as a possible alternative to the hidden mass hypothesis.' *Astrophysical Journal* 270 (July 1983), pp. 365–370. DOI: 10.1086/161130.

[48] M. Milgrom. 'A modification of the Newtonian dynamics - Implications for galaxies.' *Astrophysical Journal* 270 (July 1983), pp. 371–389. DOI: 10.1086/161131.

[49] M. Milgrom. 'A modification of the newtonian dynamics : implications for galaxy systems.' *Astrophysical Journal* 270 (July 1983), pp. 384–389. DOI: 10.1086/161132.

[50] Mordehai Milgrom and Robert H. Sanders. 'MOND predictions of halo phenomenology in disc galaxies'. *Mon. Not. Roy. Astron. Soc.* 357 (2005), pp. 45–48. DOI: 10.1111/j.1365-2966.2004.08578.x. arXiv: astro-ph/0406487 [astro-ph].

[51] Mordehai Milgrom and Robert H. Sanders. 'MOND rotation curves of very low mass spiral galaxies'. *Astrophys. J.* 658 (2007), p. L17. DOI: 10.1086/513695. arXiv: astro-ph/0611494 [astro-ph].

[52] Jacob D. Bekenstein. 'Relativistic gravitation theory for the MOND paradigm'. *Phys. Rev.* D70 (2004). [Erratum: Phys. Rev.D71,069901(2005)], p. 083509. DOI: 10.1103/PhysRevD.70.083509,10.1103/PhysRevD.71.069901. arXiv: astro-ph/0403694 [astro-ph].

[53] Douglas Clowe et al. 'A Direct Empirical Proof of the Existence of Dark Matter'. *The Astrophysical Journal* 648.2 (Aug. 2006), pp. L109–L113. DOI: 10.1086/508162. URL: https://doi.org/10.1086%2F508162.

[54] Aurel Schneider, Robert E. Smith, and Darren Reed. 'Halo Mass Function and the Free Streaming Scale'. *Mon. Not. Roy. Astron. Soc.* 433 (2013), p. 1573. DOI: 10.1093/mnras/stt829. arXiv: 1303.0839 [astro-ph.CO].

[55] George R. Blumenthal et al. 'Formation of galaxies and large-scale structure with cold dark matter'. *Nature* 311.5986 (1984), pp. 517–525. ISSN: 1476-4687. DOI: 10.1038/311517a0. URL: https://doi.org/10.1038/311517a0.

[56] Simon D. M. White et al. 'Clusters, Filaments, and Voids in a Universe Dominated by Cold Dark Matter'. *Astrophysical Journal* 313 (Feb. 1987), p. 505. DOI: 10.1086/164990.

[57] A. L. Melott et al. 'Cluster Analysis of the Nonlinear Evolution of Large-Scale Structure in an Axion/Gravitino/Photino-Dominated Universe'. *Physical Review Letters* 51.10 (Sept. 1983), pp. 935–938. DOI: 10.1103/PhysRevLett.51.935.

[58] J. R. Bond, A. S. Szalay, and M. S. Turner. 'Formation of Galaxies in a Gravitino-Dominated Universe'. *Phys. Rev. Lett.* 48 (23 June 1982), pp. 1636–1639. DOI: 10.1103/PhysRevLett.48.1636. URL: https://link.aps.org/doi/10.1103/PhysRevLett.48.1636.

[59] P. J. E. Peebles. 'Primeval adiabatic perturbations - Effect of massive neutrinos'. *Astrophysical Journal* 258 (July 1982), pp. 415–424. DOI: 10.1086/160094.

[60] J. R. Bond and A. S. Szalay. 'The collisionless damping of density fluctuations in an expanding universe'. *Astrophysical Journal* 274 (Nov. 1983), pp. 443–468. DOI: 10.1086/161460.

[61] S. D. M. White, C. S. Frenk, and M. Davis. 'Clustering in a neutrino-dominated universe'. *Astrophysical Journal, Letters* 274 (Nov. 1983), pp. L1–L5. DOI: 10.1086/184139.

[62] A. S. Szalay and G. Marx. 'Neutrino rest mass from cosmology'. *Astron. Astrophys.* 49 (1976), pp. 437–441.

[63] Y. Akrami et al. 'Planck 2018 results. I. Overview and the cosmological legacy of Planck' (2018). arXiv: 1807.06205 [astro-ph.CO].

[64] R. D. Peccei and Helen R. Quinn. 'CP Conservation in the Presence of Instantons'. *Phys. Rev. Lett.* 38 (1977). [,328(1977)], pp. 1440–1443. DOI: `10.1103/PhysRevLett.38.1440`.

[65] Scott Dodelson and Lawrence M. Widrow. 'Sterile-neutrinos as dark matter'. *Phys. Rev. Lett.* 72 (1994), pp. 17–20. DOI: `10.1103/PhysRevLett.72.17`. arXiv: `hep-ph/9303287 [hep-ph]`.

[66] A. Boyarsky et al. 'Sterile Neutrino Dark Matter'. *Prog. Part. Nucl. Phys.* 104 (2019), pp. 1–45. DOI: `10.1016/j.ppnp.2018.07.004`. arXiv: `1807.07938 [hep-ph]`.

[67] Palash B. Pal and Lincoln Wolfenstein. 'Radiative Decays of Massive Neutrinos'. *Phys. Rev.* D25 (1982), p. 766. DOI: `10.1103/PhysRevD.25.766`.

[68] Jean-Loup Gervais and B. Sakita. 'Field Theory Interpretation of Supergauges in Dual Models'. *Nucl. Phys.* B34 (1971). [,154(1971)], pp. 632–639. DOI: `10.1016/0550-3213(71)90351-8`.

[69] Yu. A. Golfand and E. P. Likhtman. 'Extension of the Algebra of Poincare Group Generators and Violation of p Invariance'. *JETP Lett.* 13 (1971). [Pisma Zh. Eksp. Teor. Fiz.13,452(1971)], pp. 323–326.

[70] D. V. Volkov and V. P. Akulov. 'Possible universal neutrino interaction'. *JETP Lett.* 16 (1972). [Pisma Zh. Eksp. Teor. Fiz.16,621(1972)], pp. 438–440.

[71] J. Wess and B. Zumino. 'Supergauge Transformations in Four-Dimensions'. *Nucl. Phys.* B70 (1974). [,24(1974)], pp. 39–50. DOI: `10.1016/0550-3213(74)90355-1`.

[72] Paolo Gondolo and Graciela Gelmini. 'Cosmic abundances of stable particles: Improved analysis'. *Nucl. Phys.* B360 (1991), pp. 145–179. DOI: `10.1016/0550-3213(91)90438-4`.

[73] Kim Griest and David Seckel. 'Three exceptions in the calculation of relic abundances'. *Phys. Rev.* D 43 (10 May 1991), pp. 3191–3203. DOI: `10.1103/PhysRevD.43.3191`. URL: `https://link.aps.org/doi/10.1103/PhysRevD.43.3191`.

[74] Julio F. Navarro, Carlos S. Frenk, and Simon D. M. White. 'The Structure of cold dark matter halos'. *Astrophys. J.* 462 (1996), pp. 563–575. DOI: `10.1086/177173`. arXiv: `astro-ph/9508025 [astro-ph]`.

[75] J. Einasto. 'On the Construction of a Composite Model for the Galaxy and on the Determination of the System of Galactic Parameters'. *Trudy Astrofizicheskogo Instituta Alma-Ata* 5 (1965), pp. 87–100.

[76] A. Burkert. 'The Structure of dark matter halos in dwarf galaxies'. *IAU Symp.* 171 (1996). [Astrophys. J.447,L25(1995)], p. 175. DOI: `10.1086/309560`. arXiv: `astro-ph/9504041 [astro-ph]`.

[77] Mattia Fornasa and Anne M. Green. 'Self-consistent phase-space distribution function for the anisotropic dark matter halo of the Milky Way'. *Phys.*

Rev. D89.6 (2014), p. 063531. DOI: `10.1103/PhysRevD.89.063531`. arXiv: `1311.5477 [astro-ph.CO]`.

[78] Lisa Goodenough and Dan Hooper. 'Possible Evidence For Dark Matter Annihilation In The Inner Milky Way From The Fermi Gamma Ray Space Telescope' (2009). arXiv: `0910.2998 [hep-ph]`.

[79] Dan Hooper and Lisa Goodenough. 'Dark Matter Annihilation in The Galactic Center As Seen by the Fermi Gamma Ray Space Telescope'. *Phys. Lett.* B697 (2011), pp. 412–428. DOI: `10.1016/j.physletb.2011.02.029`. arXiv: `1010.2752 [hep-ph]`.

[80] Dan Hooper and Tracy R. Slatyer. 'Two Emission Mechanisms in the Fermi Bubbles: A Possible Signal of Annihilating Dark Matter'. *Phys. Dark Univ.* 2 (2013), pp. 118–138. DOI: `10.1016/j.dark.2013.06.003`. arXiv: `1302.6589 [astro-ph.HE]`.

[81] M. Ajello et al. 'Fermi-LAT Observations of High-Energy γ-Ray Emission Toward the Galactic Center'. *Astrophys. J.* 819.1 (2016), p. 44. DOI: `10.3847/0004-637X/819/1/44`. arXiv: `1511.02938 [astro-ph.HE]`.

[82] Rebecca K. Leane and Tracy R. Slatyer. 'Dark Matter Strikes Back at the Galactic Center' (2019). arXiv: `1904.08430 [astro-ph.HE]`.

[83] S. Courteau et al. 'Galaxy Masses'. *Rev. Mod. Phys.* 86 (2014), pp. 47–119. DOI: `10.1103/RevModPhys.86.47`. arXiv: `1309.3276 [astro-ph.CO]`.

[84] M. Ackermann et al. 'Searching for Dark Matter Annihilation from Milky Way Dwarf Spheroidal Galaxies with Six Years of Fermi Large Area Telescope Data'. *Phys. Rev. Lett.* 115.23 (2015), p. 231301. DOI: `10.1103/PhysRevLett.115.231301`. arXiv: `1503.02641 [astro-ph.HE]`.

[85] H. Abdalla et al. 'Searches for gamma-ray lines and 'pure WIMP' spectra from Dark Matter annihilations in dwarf galaxies with H.E.S.S'. *JCAP* 1811.11 (2018), p. 037. DOI: `10.1088/1475-7516/2018/11/037`. arXiv: `1810.00995 [astro-ph.HE]`.

[86] Oscar Adriani et al. 'An anomalous positron abundance in cosmic rays with energies 1.5-100 GeV'. *Nature* 458 (2009), pp. 607–609. DOI: `10.1038/nature07942`. arXiv: `0810.4995 [astro-ph]`.

[87] M. Ackermann et al. 'Measurement of Separate Cosmic-Ray Electron and Positron Spectra with the Fermi Large Area Telescope'. *Phys. Rev. Lett.* 108.1, 011103 (Jan. 2012), p. 011103. DOI: `10.1103/PhysRevLett.108.011103`. arXiv: `1109.0521 [astro-ph.HE]`.

[88] M. Aguilar et al. 'First Result from the Alpha Magnetic Spectrometer on the International Space Station: Precision Measurement of the Positron Fraction in Primary Cosmic Rays of 0.5–350 GeV'. *Phys. Rev. Lett.* 110 (14 Apr. 2013), p. 141102. DOI: `10.1103/PhysRevLett.110.141102`. URL: `https://link.aps.org/doi/10.1103/PhysRevLett.110.141102`.

[89] Dan Hooper et al. 'HAWC Observations Strongly Favor Pulsar Interpretations of the Cosmic-Ray Positron Excess'. *Phys. Rev.* D96.10 (2017), p. 103013. DOI: 10.1103/PhysRevD.96.103013. arXiv: 1702.08436 [astro-ph.HE].

[90] Riccardo Catena and Piero Ullio. 'A novel determination of the local dark matter density'. *JCAP* 1008 (2010), p. 004. DOI: 10.1088/1475-7516/2010/08/004. arXiv: 0907.0018 [astro-ph.CO].

[91] Martin C. Smith et al. 'The RAVE survey: constraining the local Galactic escape speed'. *Monthly Notices of the Royal Astronomical Society* 379.2 (July 2007), pp. 755–772. ISSN: 0035-8711. DOI: 10.1111/j.1365-2966.2007.11964.x. eprint: http://oup.prod.sis.lan/mnras/article-pdf/379/2/755/3399611/mnras0379-0755.pdf. URL: https://doi.org/10.1111/j.1365-2966.2007.11964.x.

[92] Katherine Freese, Joshua Frieman, and Andrew Gould. 'Signal modulation in cold-dark-matter detection'. *Phys. Rev. D* 37 (12 June 1988), pp. 3388–3405. DOI: 10.1103/PhysRevD.37.3388. URL: https://link.aps.org/doi/10.1103/PhysRevD.37.3388.

[93] Jo Bovy, David W. Hogg, and Hans-Walter Rix. 'GALACTIC MASERS AND THE MILKY WAY CIRCULAR VELOCITY'. *The Astrophysical Journal* 704.2 (Oct. 2009), pp. 1704–1709. ISSN: 1538-4357. DOI: 10.1088/0004-637x/704/2/1704. URL: http://dx.doi.org/10.1088/0004-637X/704/2/1704.

[94] Ralph Schönrich, James Binney, and Walter Dehnen. 'Local kinematics and the local standard of rest'. *Monthly Notices of the Royal Astronomical Society* 403.4 (Apr. 2010), pp. 1829–1833. ISSN: 1365-2966. DOI: 10.1111/j.1365-2966.2010.16253.x. URL: http://dx.doi.org/10.1111/j.1365-2966.2010.16253.x.

[95] E. Aprile et al. 'The XENON1T dark matter experiment'. *The European Physical Journal C* 77.12 (Dec. 2017), p. 881. ISSN: 1434-6052. DOI: 10.1140/epjc/s10052-017-5326-3. URL: https://doi.org/10.1140/epjc/s10052-017-5326-3.

[96] D. S. Akerib et al. 'Technical Results from the Surface Run of the LUX Dark Matter Experiment'. *Astropart. Phys.* 45 (2013), pp. 34–43. DOI: 10.1016/j.astropartphys.2013.02.001. arXiv: 1210.4569 [astro-ph.IM].

[97] P. Agnes et al. 'First results from the DarkSide-50 dark matter experiment at Laboratori Nazionali del Gran Sasso'. *Physics Letters B* 743 (2015), pp. 456–466. ISSN: 0370-2693. DOI: https://doi.org/10.1016/j.physletb.2015.03.012. URL: http://www.sciencedirect.com/science/article/pii/S0370269315001756.

[98] Andi Tan et al. 'Dark Matter Search Results from the Commissioning Run of PandaX-II'. *Phys. Rev.* D93.12 (2016), p. 122009. DOI: 10.1103/PhysRevD.93.122009. arXiv: 1602.06563 [hep-ex].

[99] R. Agnese et al. 'Demonstration of surface electron rejection with interleaved germanium detectors for dark matter searches'. *Applied Physics Letters* 103.16 (2013), p. 164105. DOI: 10.1063/1.4826093. eprint: https://doi.org/10.1063/1.4826093. URL: https://doi.org/10.1063/1.4826093.

[100] E. Aprile et al. 'Dark Matter Search Results from a One Ton-Year Exposure of XENON1T'. *Phys. Rev. Lett.* 121.11 (2018), p. 111302. DOI: 10.1103/PhysRevLett.121.111302. arXiv: 1805.12562 [astro-ph.CO].

[101] D. S. Akerib et al. 'Improved Limits on Scattering of Weakly Interacting Massive Particles from Reanalysis of 2013 LUX Data'. *Phys. Rev. Lett.* 116.16 (2016), p. 161301. DOI: 10.1103/PhysRevLett.116.161301. arXiv: 1512.03506 [astro-ph.CO].

[102] D. S. Akerib et al. 'Results from a search for dark matter in the complete LUX exposure'. *Phys. Rev. Lett.* 118.2 (2017), p. 021303. DOI: 10.1103/PhysRevLett.118.021303. arXiv: 1608.07648 [astro-ph.CO].

[103] Xiangyi Cui et al. 'Dark Matter Results From 54-Ton-Day Exposure of PandaX-II Experiment'. *Phys. Rev. Lett.* 119.18 (2017), p. 181302. DOI: 10.1103/PhysRevLett.119.181302. arXiv: 1708.06917 [astro-ph.CO].

[104] P. Agnes et al. 'DarkSide-50 532-day Dark Matter Search with Low-Radioactivity Argon'. *Phys. Rev.* D98.10 (2018), p. 102006. DOI: 10.1103/PhysRevD.98.102006. arXiv: 1802.07198 [astro-ph.CO].

[105] R. Agnese et al. 'Search for Low-Mass Dark Matter with CDMSlite Using a Profile Likelihood Fit'. *Phys. Rev.* D99.6 (2019), p. 062001. DOI: 10.1103/PhysRevD.99.062001. arXiv: 1808.09098 [astro-ph.CO].

[106] R. Agnese et al. 'Results from the Super Cryogenic Dark Matter Search Experiment at Soudan'. *Phys. Rev. Lett.* 120.6 (2018), p. 061802. DOI: 10.1103/PhysRevLett.120.061802. arXiv: 1708.08869 [hep-ex].

[107] J. Billard, L. Strigari, and E. Figueroa-Feliciano. 'Implication of neutrino backgrounds on the reach of next generation dark matter direct detection experiments'. *Phys. Rev.* D89.2 (2014), p. 023524. DOI: 10.1103/PhysRevD.89.023524. arXiv: 1307.5458 [hep-ph].

[108] Lyndon Evans and Philip Bryant. 'LHC Machine'. *Journal of Instrumentation* 3.08 (Aug. 2008), S08001–S08001. DOI: 10.1088/1748-0221/3/08/s08001. URL: https://doi.org/10.1088%2F1748-0221%2F3%2F08%2Fs08001.

[109] Ringaile Placakyte. 'Parton Distribution Functions'. In: *Proceedings, 31st International Conference on Physics in collisions (PIC 2011): Vancouver, Canada, August 28-September 1, 2011*. 2011. arXiv: 1111.5452 [hep-ph].

[110] Albert M Sirunyan et al. 'Search for invisible decays of a Higgs boson produced through vector boson fusion in proton-proton collisions at $\sqrt{s} = 13\,\text{TeV}$'. *Phys. Lett.* B793 (2019), pp. 520–551. DOI: 10.1016/j.physletb.2019.04.025. arXiv: 1809.05937 [hep-ex].

[111] Valentin Hirschi et al. 'Automation of one-loop QCD corrections'. *JHEP* 05 (2011), p. 044. DOI: 10.1007/JHEP05(2011)044. arXiv: 1103.0621 [hep-ph].

[112] Giovanni Ossola, Costas G. Papadopoulos, and Roberto Pittau. 'NLO corrections with the OPP method'. *Nuclear Physics B - Proceedings Supplements* 183 (2008). Proceedings of the 9th DESY Workshop on Elementary Particle Theory, 42–47. ISSN: 0920-5632. DOI: https://doi.org/10.1016/j.nuclphysbps.2008.09.080. URL: http://www.sciencedirect.com/science/article/pii/S0920563208001989.

[113] G. Passarino and M. Veltman. 'One-loop corrections for e^+e^- annihilation into $\mu^+\mu^-$ in the Weinberg model'. *Nuclear Physics B* 160.1 (1979), pp. 151–207. ISSN: 0550-3213. DOI: https://doi.org/10.1016/0550-3213(79)90234-7. URL: http://www.sciencedirect.com/science/article/pii/0550321379902347.

[114] Andrei I. Davydychev. 'A Simple formula for reducing Feynman diagrams to scalar integrals'. *Phys. Lett.* B263 (1991), pp. 107–111. DOI: 10.1016/0370-2693(91)91715-8.

[115] Gerard 't Hooft and M. J. G. Veltman. 'Scalar One Loop Integrals'. *Nucl. Phys.* B153 (1979), pp. 365–401. DOI: 10.1016/0550-3213(79)90605-9.

[116] Giovanni Ossola, Costas G. Papadopoulos, and Roberto Pittau. 'On the Rational Terms of the one-loop amplitudes'. *JHEP* 05 (2008), p. 004. DOI: 10.1088/1126-6708/2008/05/004. arXiv: 0802.1876 [hep-ph].

[117] Celine Degrande et al. 'UFO - The Universal FeynRules Output'. *Comput. Phys. Commun.* 183 (2012), pp. 1201–1214. DOI: 10.1016/j.cpc.2012.01.022. arXiv: 1108.2040 [hep-ph].

[118] Mihailo Backovič, Kyoungchul Kong, and Mathew McCaskey. 'MadDM v.1.0: Computation of Dark Matter Relic Abundance Using MadGraph5'. *Physics of the Dark Universe* 5-6 (2014), pp. 18–28. DOI: 10.1016/j.dark.2014.04.001. arXiv: 1308.4955 [hep-ph].

[119] Mihailo Backovič et al. 'Direct Detection of Dark Matter with MadDM v.2.0'. *Phys. Dark Univ.* 9-10 (2015), pp. 37–50. DOI: 10.1016/j.dark.2015.09.001. arXiv: 1505.04190 [hep-ph].

[120] Carlos Faham. 'First Dark Matter Search Results from the Large Underground Xenon (LUX) Experiment'. In: *Proceedings, 49th Rencontres de Moriond on Cosmology: La Thuile, Italy, March 15-22, 2014*. 2014, pp. 167–170. arXiv: 1405.5906 [hep-ex].

[121] E. Aprile et al. 'First Dark Matter Search Results from the XENON1T Experiment'. *Phys. Rev. Lett.* 119.18 (2017), p. 181301. DOI: 10.1103/PhysRevLett.119.181301. arXiv: 1705.06655 [astro-ph.CO].

[122] D. S. Akerib et al. 'Limits on spin-dependent WIMP-nucleon cross section obtained from the complete LUX exposure'. *Phys. Rev. Lett.* 118.25 (2017),

p. 251302. DOI: 10.1103/PhysRevLett.118.251302. arXiv: 1705.03380 [astro-ph.CO].

[123] C. Amole et al. 'Dark Matter Search Results from the PICO-60 C_3F_8 Bubble Chamber'. *Phys. Rev. Lett.* 118.25 (2017), p. 251301. DOI: 10.1103/PhysRevLett.118.251301. arXiv: 1702.07666 [astro-ph.CO].

[124] A. Albert et al. 'Searching for Dark Matter Annihilation in Recently Discovered Milky Way Satellites with Fermi-LAT'. *Astrophys. J.* 834.2 (2017), p. 110. DOI: 10.3847/1538-4357/834/2/110. arXiv: 1611.03184 [astro-ph.HE].

[125] A. Albert et al. *Figures and data files associated with the Fermi LAT paper "Searching for Dark Matter Annihilation in Recently Discovered Milky Way Satellites with Fermi-LAT"*. 2016. URL: https://www-glast.stanford.edu/pub_data/1203/.

[126] Matthew Gonderinger et al. 'Vacuum Stability, Perturbativity, and Scalar Singlet Dark Matter'. *JHEP* 01 (2010), p. 053. DOI: 10.1007/JHEP01(2010)053. arXiv: 0910.3167 [hep-ph].

[127] M. Tanabashi et al. 'Review of Particle Physics'. *Phys. Rev.* D 98 (3 Aug. 2018), p. 030001. DOI: 10.1103/PhysRevD.98.030001. URL: https://link.aps.org/doi/10.1103/PhysRevD.98.030001.

[128] William J. Marciano, Cen Zhang, and Scott Willenbrock. 'Higgs Decay to Two Photons'. *Phys. Rev.* D85 (2012), p. 013002. DOI: 10.1103/PhysRevD.85.013002. arXiv: 1109.5304 [hep-ph].

[129] Claude Duhr. 'Higgs effective theory' (2011). URL: http://feynrules.irmp.ucl.ac.be/wiki/HiggsEffectiveTheory#no1.

[130] Geneviève Bélanger et al. 'micrOMEGAs5.0 : Freeze-in'. *Comput. Phys. Commun.* 231 (2018), pp. 173–186. DOI: 10.1016/j.cpc.2018.04.027. arXiv: 1801.03509 [hep-ph].

[131] James M. Cline et al. 'Update on scalar singlet dark matter'. *Phys. Rev.* D88 (2013). [Erratum: Phys. Rev.D92,no.3,039906(2015)], p. 055025. DOI: 10.1103/PhysRevD.92.039906,10.1103/PhysRevD.88.055025. arXiv: 1306.4710 [hep-ph].

[132] Shinya Kanemura et al. 'Can WIMP Dark Matter overcome the Nightmare Scenario?' *Phys. Rev.* D82 (2010), p. 055026. DOI: 10.1103/PhysRevD.82.055026. arXiv: 1005.5651 [hep-ph].

[133] Mathias Garny et al. 'Majorana Dark Matter with a Coloured Mediator: Collider vs Direct and Indirect Searches'. *JHEP* 06 (2014), p. 169. DOI: 10.1007/JHEP06(2014)169. arXiv: 1403.4634 [hep-ph].

[134] Mathias Garny et al. 'Coannihilation without chemical equilibrium'. *Phys. Rev.* D96.10 (2017), p. 103521. DOI: 10.1103/PhysRevD.96.103521. arXiv: 1705.09292 [hep-ph].

[135] P. A. R. Ade et al. 'Planck 2015 results. XIII. Cosmological parameters'. *Astron. Astrophys.* 594 (2016), A13. DOI: 10.1051/0004-6361/201525830. arXiv: 1502.01589 [astro-ph.CO].

[136] Albert M Sirunyan et al. 'Search for direct production of supersymmetric partners of the top quark in the all-jets final state in proton-proton collisions at $\sqrt{s} = 13$ TeV'. *JHEP* 10 (2017), p. 005. DOI: 10.1007/JHEP10(2017)005. arXiv: 1707.03316 [hep-ex].

[137] Albert M Sirunyan et al. 'Search for new phenomena with the M_{T2} variable in the all-hadronic final state produced in proton-proton collisions at $\sqrt{s} = 13$ TeV'. *Eur. Phys. J.* C77.10 (2017), p. 710. DOI: 10.1140/epjc/s10052-017-5267-x. arXiv: 1705.04650 [hep-ex].

[138] Albert M Sirunyan et al. 'Search for top squark pair production in pp collisions at $\sqrt{s} = 13$ TeV using single lepton events'. *JHEP* 10 (2017), p. 019. DOI: 10.1007/JHEP10(2017)019. arXiv: 1706.04402 [hep-ex].

[139] Morad Aaboud et al. 'Search for a scalar partner of the top quark in the jets plus missing transverse momentum final state at $\sqrt{s}$=13 TeV with the ATLAS detector'. *JHEP* 12 (2017), p. 085. DOI: 10.1007/JHEP12(2017)085. arXiv: 1709.04183 [hep-ex].

[140] Morad Aaboud et al. 'Search for top-squark pair production in final states with one lepton, jets, and missing transverse momentum using 36 fb^{-1} of $\sqrt{s} = 13$ TeV pp collision data with the ATLAS detector'. *JHEP* 06 (2018), p. 108. DOI: 10.1007/JHEP06(2018)108. arXiv: 1711.11520 [hep-ex].

[141] M. Aaboud et al. 'Search for direct top squark pair production in final states with two leptons in $\sqrt{s} = 13$ TeV pp collisions with the ATLAS detector'. *Eur. Phys. J.* C77.12 (2017), p. 898. DOI: 10.1140/epjc/s10052-017-5445-x. arXiv: 1708.03247 [hep-ex].

[142] M. Aguilar et al. 'Antiproton Flux, Antiproton-to-Proton Flux Ratio, and Properties of Elementary Particle Fluxes in Primary Cosmic Rays Measured with the Alpha Magnetic Spectrometer on the International Space Station'. *Phys. Rev. Lett.* 117.9 (2016), p. 091103. DOI: 10.1103/PhysRevLett.117.091103.

[143] Mathias Garny et al. 'Internal bremsstrahlung signatures in light of direct dark matter searches'. *JCAP* 1312 (2013), p. 046. DOI: 10.1088/1475-7516/2013/12/046. arXiv: 1306.6342 [hep-ph].

[144] Agnieszka Ilnicka, Maria Krawczyk, and Tania Robens. 'Inert Doublet Model in light of LHC Run I and astrophysical data'. *Phys. Rev.* D93.5 (2016), p. 055026. DOI: 10.1103/PhysRevD.93.055026. arXiv: 1508.01671 [hep-ph].

[145] Alexander Belyaev et al. 'Anatomy of the Inert Two Higgs Doublet Model in the light of the LHC and non-LHC Dark Matter Searches'. *Phys. Rev.* D97.3 (2018), p. 035011. DOI: 10.1103/PhysRevD.97.035011. arXiv: 1612.00511 [hep-ph].

[146] Benedikt Eiteneuer, Andreas Goudelis, and Jan Heisig. 'The inert doublet model in the light of Fermi-LAT gamma-ray data: a global fit analysis'. *Eur. Phys. J.* C77.9 (2017), p. 624. DOI: 10.1140/epjc/s10052-017-5166-1. arXiv: 1705.01458 [hep-ph].

[147] Michael Gustafsson et al. 'Significant Gamma Lines from Inert Higgs Dark Matter'. *Phys. Rev. Lett.* 99 (2007), p. 041301. DOI: 10.1103/PhysRevLett.99.041301. arXiv: astro-ph/0703512 [ASTRO-PH].

[148] Camilo Garcia-Cely, Michael Gustafsson, and Alejandro Ibarra. 'Probing the Inert Doublet Dark Matter Model with Cherenkov Telescopes'. *JCAP* 1602.02 (2016), p. 043. DOI: 10.1088/1475-7516/2016/02/043. arXiv: 1512.02801 [hep-ph].